Title
From Polyoxometalates to Metal-Organic Frameworks: Inorganic Compounds in the Study and Treatment of Disease

Author
Levine, Dana Jaya

Publication Date
2016

Peer reviewed|Thesis/dissertation

From Polyoxometalates to Metal-Organic Frameworks:

Inorganic Compounds in the Study and Treatment of Disease

By

Dana Jaya Levine

A dissertation submitted in partial satisfaction of the

requirements for the degree of

Doctor of Philosophy

in

Chemistry

and the Designated Emphasis

in

Nanoscale Science and Engineering

in the

Graduate Division

of the

University of California, Berkeley

Committee in charge:

Professor Jeffrey R. Long, Chair
Professor Kenneth N. Raymond
Professor Phillip B. Messersmith

Spring 2016

Abstract

From Polyoxometalates to Metal-Organic Frameworks:

Inorganic Compounds in the Study and Treatment of Disease

By

Dana Jaya Levine

Doctor of Philosophy in Chemistry

and the Designated Emphasis

in

Nanoscale Science and Engineering

University of California, Berkeley

Professor Jeffrey R. Long, Chair

The diverse structures and properties of inorganic compounds are powerful tools that can be used to address various challenges in the field of medicine. In this dissertation, one goal was to elucidate the underlying mechanism of a common method for precipitation of infectious prions that is mediated by polyoxometalates. Another aspect of this work focused on developing metal-organic materials for drug delivery applications. In particular, calcium-based coordination solids were prepared for pH-triggered delivery of olsalazine, a drug used in the treatment of ulcerative colitis. Further, olsalazine was used as a ligand to synthesize a new family of porous metal-organic frameworks with open metal sites that can serve as platforms for gas storage and drug delivery.

The Keggin-type phosphotungstate anion (PTA) is a polyoxometalate that has been widely used to facilitate the precipitation of the disease-causing prion protein (PrP^{Sc}) from infected tissue for detection and biophysical study. In order to probe the mechanism of this method, the PTA precipitation was evaluated by several techniques including nuclear magnetic resonance spectroscopy and mass spectrometry at varying pH, revealing decomposition of the parent $[PW_{12}O_{40}]^{3-}$ ion into a $[PW_{11}O_{39}]^{7-}$ (PW_{11}) complex and a single orthotungstate anion $[WO_4]^{2-}$. The efficacy of each component was then evaluated by immunoblotting, ELISA, and electron microscopy. These studies revealed that both the PW_{11} and orthotungstate species contribute to PrP^{Sc} precipitation. However, the purity and ease of detecting PrP^{Sc} by ELISA increases when co-precipitation of lipids is suppressed by PW_{11}. To further elucidate the mechanism of PrP^{Sc} precipitation, each buffer component was evaluated to determine its influence on the morphology of PrP aggregates in crude brain homogenate. A synergistic effect is observed with PTA and

detergent on the formation of larger, fibrillar aggregates, which leads to effective separation of lipids from PrP^{Sc} and higher precipitation yields. From these results, we can conclude that the separation of buoyant lipids from PrP^{Sc} is a major factor governing the facile precipitation of prions from tissue. This understanding may lead to improved methods to determine the structure of the infectious prion isoform and aid in the development of robust diagnostic tools for prion detection.

The therapeutic value of biologically active small molecules can be increased through coordination to biocompatible metals. In addition to altering the pharmacokinetic properties of a drug, the metal interaction can also be tuned to release the active drug in response to changes in the environment such as pH variations. To this end, the ulcerative colitis drug olsalazine (H_4olz) was used as a ligand to form extended coordination solids, including one-dimensional chains ($Ca(H_2olz)\cdot 4H_2O$), two-dimensional sheets ($Ca(H_2olz)\cdot 2H_2O$), and a flexible three-dimensional metal-organic framework ($Ca(H_2olz)\cdot 2DMF$). Further, the $Ca(H_2olz)\cdot 2DMF$ framework can be desolvated to produce a dense $Ca(H_2olz)$ phase upon treatment with aqueous acid. These materials are all highly crystalline and have been characterized by TGA, pXRD, and single crystal X-ray diffraction. Each material was pressed into pellets and exposed to simulated gastrointestinal fluids to mimic the passage of a pill from the acidic stomach environment to the neutral pH of the intestines and colon. All three calcium materials released olsalazine more gradually when compared to the sodium salt control, which underwent rapid release under simulated intestinal conditions. These results suggest that the calcium coordination solids of olsalazine may provide advantages over the existing sodium formulations by minimizing side effects that arise from early release outside of the colon.

Olsalazine was also used as a ligand to create a new series of porous metal-organic frameworks that are expanded analogues of the well known MOF-74 M_2(dobdc) materials ($dobdc^{4-}$ = 2,5-dioxido-1,4-benzenedicarboxylate). The M_2(olz) frameworks have been synthesized with M = Mg, Fe, Co, Ni, and Zn, and they exhibit high surface areas with large hexagonal pore apertures, approximately 27 Å in diameter. Gas sorption studies have been performed at varying temperatures with hydrogen and carbon dioxide, revealing strong uptake for each of these gases. The nature of the hydrogen interaction was further studied by infrared spectroscopy, which revealed multiple binding sites and high enthalpies of adsorption. The open metal sites of Mg_2(olz) were also used to coordinate phenethylamine (PEA), a model drug for a broad class of bioactive compounds. The $Mg_2(olz)(PEA)_2$ material was subjected to simulated biological conditions, and we observed controlled release of phenethylamine from the pores, along with slower, concurrent dissolution of the framework. The low toxicity, high surface areas, and coordinatively unsaturated open metal sites make these M_2(olz) materials promising candidates for applications in gas storage, separations, and drug delivery.

Para mis padres, Hela Levine Jungster y Samuel Levine,
por su inspiración y apoyo en la realización de este sueño.

Table of Contents

Table of Figures

Acknowledgements

I would first like to thank my advisor, Prof. Jeffrey Long, for giving me the freedom to pursue my interests at the intersection of inorganic chemistry and medicine, for encouraging me to think deeply about my research, and for refining my palate for sour beers and barrel-aged spirits. Jeff is a remarkable scientist whose dedication to applied research while addressing fundamental questions in chemistry has shaped my own approach to science.

I would also like to thank my thesis committee members, Prof. Kenneth Raymond and Prof. Phillip Messersmith. Ken's prolific contributions to bioinorganic chemistry have inspired me to pursue this field, and it has been a pleasure to learn from him over the years. Phil's creative approach to biomaterials influenced my graduate research on metal-coordinated drug delivery platforms long before I had the opportunity to meet him in person. I am happy to have overlapped with him at Berkeley in the last year of my Ph.D. and benefited greatly from scientific conversations with him and his group.

My undergraduate research experience at Caltech and the NASA Jet Propulsion Laboratory helped ignite my passion for interdisciplinary research. For this, I thank Prof. Harry Gray, Prof. Adrian Ponce, Dr. Morgan Cable, and Prof. Hannah Shafaat for introducing me to the myriad applications of inorganic chemistry and for their continued mentorship throughout my academic career.

For the first few years of my graduate work, I spent much of my time doing research at the UCSF Institute for Neurodegenerative Diseases. It was a privilege to work with many preeminent scientists in the field of prion research, especially Dr. Stan Prusiner, who first put forth the prion hypothesis and continues to lead as a pioneer in the field. Prof. Holger Wille gave me a comprehensive introduction to the world of prions, and his years of experience in this area were invaluable. I thank Lillian Falese for teaching me to do everything from making brain homogenate to running Western blots. Prof. Jan Stöhr was a great colleague and mentor whose motivation and perspective were instrumental in helping me bring my prion research to fruition. I was also happy to have another inorganic chemist in the mix with the arrival of Zack Mensinger, who also worked between the Prusiner and Long groups and whose similar training led to many interesting scientific discussions. Aleksandra Kijac was also a joint Berkeley–IND postdoc, and I enjoyed our conversations about NMR and BART strategies. I appreciate that Joel Watts let me borrow his 2-μL pipetteman and shared my passion for blasting Dream Theater in the lab. Hang Nguyen played a key role in bringing my manuscript into the world with her editing skills, and Panos Philandrinos was always helpful and attentive in keeping everything running smoothly. I also enjoyed many fascinating conversations with Dr. Michael Geschwind about potential drug delivery systems, and I am grateful for my experiences with everyone at the IND.

A key turning point in my graduate research was the opportunity to spend a semester in the Yale Biomedical Engineering Department, and I thank Prof. Mark Saltzman for strengthening my foundation in this field. Jennifer Saucier-Sawyer was an excellent

mentor who trained me in nanoparticle synthesis and characterization techniques, while also introducing me to the skills and nuances involved in doing animal studies. I also must thank Prof. Richard Carson and the PET Center team for teaching me about the intricacies of nuclear imaging studies. Everyone in the Saltzman lab was very welcoming, and it was great to learn from everyone about their science during this time.

I would like to enthusiastically thank all of the members of the Long group, past and present, who have profoundly shaped my experience in graduate school. Even though my research was radically different from the rest of the group, everyone showed enthusiasm for my work while offering support, insight, and motivation throughout the process. I especially thank the gas sorption subgroup for inducting me into their sacred cult with monthly meetings on the Sabbath and for teaching me how to do MOF chemistry.

With six years in the group, I would have to write a separate chapter to fully capture all of the ways that everyone has influenced me in grad school, so I will try to keep this relatively short…I was excited to join the Long group with some great grad students including Katie Meihaus, Eric Bloch, Xiaowen Feng, Zoey Herm, Brian Weirs, Thomas MacDonald, Kenji Sumida, Joe Zadrozny, Dave Harris, and Jeff Rinehart. I thank Joe for introducing me to the department as someone who kept mysterious things hidden behind a wall of old mattresses in my garage (spoiler: it was a drum set). Katie, thank you for your constant support from the beginning and for letting me crash on your couch while I knocked out my last few experiments.

In the following years, the Long group family continued to grow with many more awesome students including Jordan Axelson, Jarad Mason, David Zee, Miguel Gonzalez, Mike Aubrey, Dianne Xiao, Lucy Darago, Matt Kapelewski, Doug Reed, Phil Bunting, Julia Oktawiec, Mercedes Taylor, Rodi Torres-Gavosto, Jon Bachmann, Kristen Colwell, Rebecca Siegelman, Colin Gould, Ari Turkiewicz, Mike Ziebel, and Henry Jiang (who is an epic karaoke partner for everything from Phantom to Dio). Jordan has been a close friend who has also worked hard to forge new scientific paths in the Long group, and her dedication to teaching and outreach is inspiring. Furthermore, I owe her many more mazapanes for all of her help in tracking down signatures and handing in my paperwork.

Many wonderful postdocs in the lab have also played an important role in shaping my graduate experience, including Elizabeth Montalvo, Paulina Gómora-Figueroa, Rob Ameloot, Michael Nippe, Hemamala Karunadasa, Dave Rogow, Jeff Van Humbeck, Keith Keitz, Zack Mensinger, Wendy Queen, Gokhan Barin, Aravind Kumar, Farshid Ramezanipour, Zach Smith, Phil Milner, Jeff Martell, Jiwoong Lee, Alexander Tskhovrebov, Hye Jeong Park, and Tomce Runcevski. I am grateful for their advice and perspective in navigating the transition from graduate student to postdoc and beyond.

It was also a pleasure to work alongside many exceptional visiting students and Berkeley undergrads over the years, including Christina Legendre (synthetic wiz and sailing extraordinaire), Greg Paille, Celia Guevar, Anna Aulisio, Chiara Ortelli, Kohei Takahashi, Adam Dzierbinski, Emily Mensforth, Valentina Colombo, Mary Anne Manumpil, Kaitlyn Weeber, David Gygi, Raymond Yu, and Jo Melville.

I reserve a special acknowledgement for the high-traffic corner of 210 Lewis where I had the pleasure of sharing a space with Miguel Gonzalez and Selly Demir in my last years of grad school. I greatly valued the scientific conversations with Miguel Gonzalez, who encouraged me to think critically about my work and develop my ideas; he is also an excellent crystallographer, a dangerous bartender, and a true friend. Selly is an exceptional colleague whose friendship, perspective, and encouragement played a crucial role in motivating me throughout my Ph.D., especially after many late nights in lab.

My labmates have also been exceptional friends throughout my time in Berkeley, and I've enjoyed everything from Longballs softball and group room parties to barbecues and Kip's karaoke. I am also very grateful to all of my good friends who helped me balance my time outside of the lab by trying delicious food and beer, werkin' it in Oakland, and simply exploring the beautiful San Francisco Bay Area (as opposed to the numerous other bays that exist in this vast country).

I would also like to thank the National Science Foundation Graduate Fellowship, the National Defense Science and Engineering Graduate Fellowship, the Neuroscience Scholars Program, and the Soroptimist Founder Region Dissertation Fellowship for their funding and support throughout my graduate career. I also appreciate the guidance I received from Lynn Keithlin, Cassandra Hill, Shela Deguzman, and Kathy Bean in navigating the hilly administrative landscape of Berkeley.

Lastly, I would like to thank my family, without whom this would not have been possible. The support and encouragement from my parents, Hela and Samuel Levine, has been indispensable. Their passion for life and science has profoundly shaped my outlook, and I am honored to share this work with them. My grandmother, Rosa Presburger, has always had an independent and tenacious spirit, and she has continually inspired me to pursue my dreams. It has also been a true joy to have a lifetime of experiences with my brother Jay, and I love sharing everything from the heaviest of metal shows to the hoppiest of beers with him. Thanks to everyone in my big family (Ifat, Yoav, Livy, Beto, Ellen, Nicole, Carolina, Fernanda, Shaye, Sonia, Max, Reina, Nir, Yael, Gadi, Daniel, Ari y todos los demás) for their warmth and support from San Diego to Mexico and beyond. Finally, I am grateful for the deep friendship and chemistry I share with David Romney, who has been my closest colleague and best friend throughout this journey.

Chapter 1: Diagnostic and Therapeutic Applications of Inorganic Compounds

1.1 Introduction

Metal-based compounds comprise a rich subset of chemistry. Through different combinations of metal and ligand, chemists can create inorganic materials with a wide range of properties. As such, metal-based compounds represent a highly diversifiable platform for the creation of tools that can address problems in many different areas of science. Recently, inorganic materials have emerged as a means to address various challenges in biology and medicine as well. On one hand, inorganic compounds can serve as probes for biological systems to help elucidate the nature of diseases. On another hand, such materials can also be used for the treatment of diseases, either by controlling the delivery of a therapeutic agent, or by serving as a therapeutic agent directly.

1.2 Metals in Neurodegeneration

1.2.1 Prions and Protein Misfolding Disorders

Prion diseases are characterized by the misfolding of the prion protein (PrP), which leads to progressive neurodegeneration in many mammals. Such diseases include Creutzfeldt-Jakob disease (CJD) in humans, scrapie in sheep, bovine spongiform encephalopathy (BSE) in cattle, and chronic wasting disease in deer and elk. In these prion diseases, endogenous PrP^{C} adopts a self-propagating conformation, designated PrP^{Sc}, which can autocatalytically convert PrP^{C} molecules into infectious PrP^{Sc} (Figure 1.1). PrP misfolding can be caused by genetic mutations, exposure to PrP^{Sc}, or occur spontaneously, resulting in inherited, acquired, or sporadic disease manifestations, respectively. Over time, PrP^{Sc} accumulates and spreads throughout the brain, leading to severe neuronal deterioration, loss of cognitive function, and ultimately death. While diseases caused by PrP^{Sc} are rare in humans, biochemical investigation of PrP^{Sc} diseases may provide valuable applications to other, more common neurodegenerative disorders. In recent studies, a self-perpetuating prion mechanism has been described for amyloid beta in Alzheimer's disease, alpha-synuclein in Parkinson's disease, huntingtin in Huntington's disease, and tau in the tauopathies.[1-6]

To better diagnose and ultimately treat these devastating diseases, it is important to elucidate the structures and the aggregation behaviors of the proteins involved. Several methods have been employed to study the prion aggregates including X-ray fiber diffraction,[7] electron microscopy,[8] and hydrogen–deuterium exchange.[9] However, the structure of PrP^{Sc} remains unknown. Structural models of PrP^{Sc} have been proposed from X-ray fiber diffraction and electron microscopy of prions isolated from brain tissue,[7,10] but the large amounts of crystalline lipids present in the samples can obscure structural features of the protein aggregates.

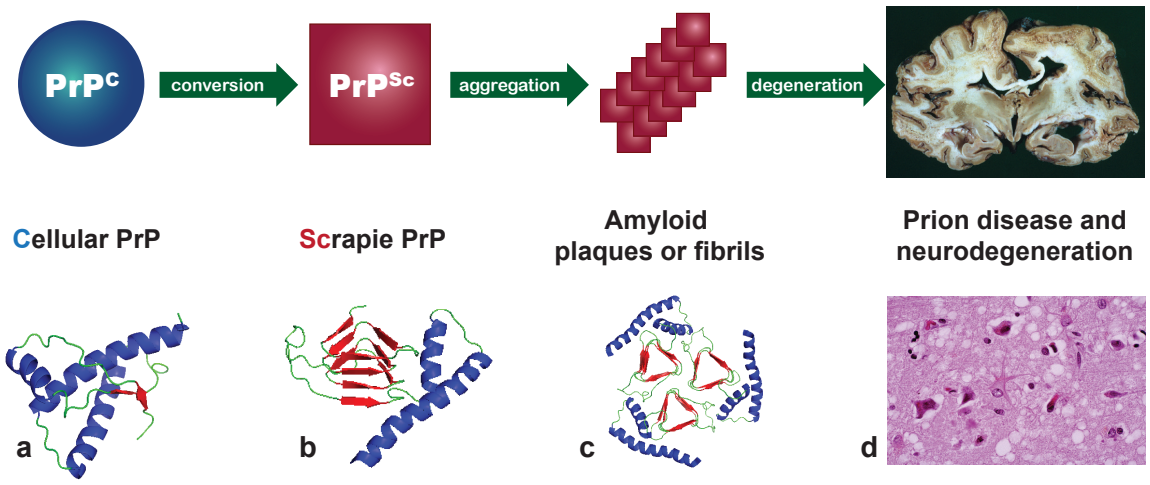

Figure 1.1. The native cellular prion protein (PrP^{C}) can misfold and adopt an infectious conformation (PrP^{Sc}) that can induce the conversion of additional PrP molecules. Aggregates of PrP^{Sc} can induce progressive neurodegeneration and encephalopathy. A solution NMR structure of PrP^{C} (a)[11] shows its rich α-helical content whereas structural models of PrP^{Sc} from X-ray fiber diffraction (b,c)[8] illustrate the dramatic increase in β-sheet content upon misfolding. These aggregates cause vacuolation and atrophy of the brain as observed in the brain pathology of a patient with advanced Creutzfeldt-Jakob disease (d).[12]

Without a true structural understanding of the infectious prion isoform or an antemortem test for its detection, our ability to develop diagnostic and therapeutic tools for these fatal diseases is severely hindered. As such, there is a continuing demand for methods to improve the isolation and detection of PrP^{Sc}.

1.2.2 Polyoxometalates as Precipitation Agents

Polyoxometalates are a class of metal oxide clusters that are comprised of rigid polyhedral units with bridging oxygen atoms. There is a wide variety of POM structures, which vary in their size, shape, composition, and charge. They can be formed by different transition metals such as vanadium, molybdenum, tungsten, and niobium and may incorporate other heteroatoms such as hydrogen, boron, silicon, phosphorus, and lanthanides.[13] The Keggin-type phosphotungstate anion (PTA, $[PW_{12}O_{40}]^{3-}$),[14] which is commonly used as a stain for electron microscopy, was found to facilitate the selective precipitation of infectious PrP^{Sc} over its cellular precursor PrP^{C}.[15] In this manner, PTA can facilitate the concentration of prions for both structural analysis and for quantification from small blood or tissue samples.[16-21] PTA has also been used to improve detection of small amounts of PrP^{Sc} in peripheral tissues of patients with Creutzfeldt–Jakob disease,[22] which could have implications for the development of an antemortem test that does not require brain samples. Furthermore, this method is markedly simpler than previous

methods, which typically required a series of labor-intensive gradient or differential centrifugation steps, which gave high purity samples but with low yield.[23-25]

Despite the widespread use of this POM to isolate prions, there was little knowledge of the underlying mechanism responsible for this effective purification method. To address this, a collaboration was formed between the Prusiner and Long groups, which first resulted in an investigation that quantified the yields of prion protein obtained from precipitations using various kinds of polyoxometalates.[26] This study concluded that Keggin-type polyoxometalate complexes, even with different substitutions at the central atom, performed better than polyoxometalates with other, less symmetric structure types. A later study involved variations of the charge of the central Keggin atom, which was able to influence the morphology of the prion aggregates observed. Some cases favored formation of fibrils while others produced two-dimensional crystals that still retained infectivity.[10] Some of these trends could be attributed to the overall charge of the complex. Understanding these differences could have implications in preparing high purity samples for structural elucidation of the prion protein.

While efforts have also been made to improve diagnostic tools for detection of PrP^{Sc} in the blood of humans and cattle,[27,28] it has been challenging to develop a rapid and reliable method for PrP^{Sc} detection due to difficulties in discriminating infectious PrP^{Sc} from endogenous PrP^{C}, low titers of PrP^{Sc} in blood, and the presence of lipid and protein contaminants that can complicate the accuracy of determinations.[29] In our most recent work, PTA was found to facilitate the precipitation of the prion protein by direct association of the protein with dense PTA derivatives and by indirect disruption of interactions between protein aggregates and buoyant anionic lipid contaminants.[30] With this mechanistic understanding, we hope to further improve our methods for the purification and detection of prions and other neurodegenerative conditions involving protein aggregation such as Alzheimer's, Huntington's, and Parkinson's diseases.

1.2.3 Role of Metals in Neurodegeneration – Opportunities for Treatment

The misfolding of proteins is considered the hallmark of prion diseases; however, some hypothesize that metal ions may also play a significant role in the pathogenesis of neurodegeneration. The functions of the brain are tightly orchestrated by regulation of metal ions, and imbalances in metal homeostasis have been observed in patients with neurodegenerative disesases.[31-33] Disruption to metal homeostasis could lead to changes in protein expression levels and induce conformational changes of metal-binding proteins, both of which can increase the likelihood of developing a disease state. For instance, the amyloid precursor protein (APP) has putative binding sites for copper and zinc, while only amyloid beta, the cleavage product linked to Alzheimer's disease, has been found to bind to iron.[34] Metal ions have also been shown to promote oligomerization of amyloidogenic proteins. Additionally, there are several metal binding motifs in the cellular prion protein (PrP^{C}) known as the octapeptide repeat regions that are widely conserved across different mammalian species and have been shown to selectively bind Cu^{2+}.[35] Misfolding of such metal binding proteins could lead to the disruptions to metal homeostasis in the brain, which may in turn increase the formation of reactive oxygen species and contribute further to misfolding and aggregation events.

With mismanagement of metals being implicated in the etiology of these diseases, metal chelation has been considered a viable target to slow down, or possibly reverse, the progression of neurodegeneration. Indeed, chelation of copper has been found to delay the onset of prion disease in an animal model.[36] Several metal chelators are currently being tested clinically for such diseases as Alzheimer's and Huntington's diseases, as this class of clioquinol compounds are orally available and can cross the blood-brain barrier (Figure 1.2). Clioquionol has been found to inhibit binding of zinc and copper ions to amyloid beta,[37] and a pilot phase II clinical trial showed that patients experienced improved cognitive function and lower plasma levels of $A\beta_{42}$ with chelation therapy.[38] Anther 8-hydroxyquinoline derivative PBT2 can act as an ionophore to increase membrane permeability to improve neuronal functions. It has completed phase IIa clinical trials for treatment of Alzheimer's disease[39] and has recently received Orphan designation for the treatment of Huntington's disease in the US and Europe. Another clioquinol derivative, PBT434 (whose structure has yet to be publically disclosed), is also involved in clinical trials and shows promise for treatment of Parkinson's disease.[40]

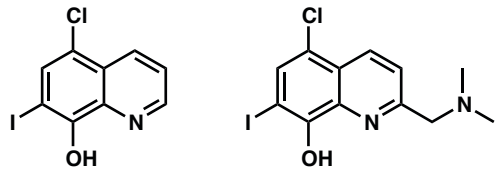

Figure 1.2. Examples of metal chelators in clinical trials for treatment of neurodegenerative diseases.

1.3 Metal-Based Compounds in Medicine

Metal-based compounds are promising as both diagnostic and therapeutic tools since the metal can impart diverse functionalities for various applications (Figure 1.3). The coordination of a metal to an organic drug can influence the properties of the active organic component, as in the case of ferroquine. By incorporating a ferrocene group in the antimalarial chloroquin, the new organometallic compound was able to overcome the resistance that *Plasmodium falciparum* (mosquitos) carrying the malaria pathogen had developed to chloroquin alone.[41,42]

In some cases, the metal itself can serve as the active species, and its preparation as a complex can aid in the delivery of the metal to the intended location. For instance, gold(I) compounds have been useful agents in the treatment of rheumatory arthritis, but the mechanism is not fully understood. While most approved gold formulations are polymeric preparations for intramuscular injection, the ligand set of auranofin enables it to exist as a monomeric complex that is orally available.[43] This is also the case for the magnetic resonance imaging (MRI) contrast agent gadolinium-DOTA (DOTA=1,4,7,10-tetraazacyclododecane-1,4,7,10-tetraacetic acid). The half-filled 4f orbitals of Gd^{3+} give

rise to relatively long electronic relaxation times, making it an effective agent for proton relaxation for MRI studies.[5] However, free Gd^{3+} is highly toxic due to its ability to compete with Ca^{2+} in the body, thus requiring a multi-dentate ligand like DOTA to chelate the Gd^{3+} and minimize dissociation of the complex.

Often, the metal and ligand components together can play a synergistic role to achieve the desired therapeutic effect. Such is the case of bismuth subsalicylate, commonly known as Pepto-Bismol, where the combined bactericidal activity of bismuth and the anti-inflammatory action of salicylic acid can ameliorate gastrointestinal discomfort. Furthermore, a particular complex may be essential to the function of the drug.

In many instances, these compounds are prodrugs, where the compound is metabolized by the body through such transformations as redox reactions and ligand substitutions, which generate the active species *in vivo*. For example, cisplatin, which is the first metallodrug approved for cancer therapy and is particularly effective for testicular cancer, undergoes ligand exchange in which chloride ligands are slowly displaced by water molecules in the blood. Upon reaching cancer cells, the water ligands are displaced by DNA; this alkylation event crosslinks the DNA and prevents further replication of the cancer cell.

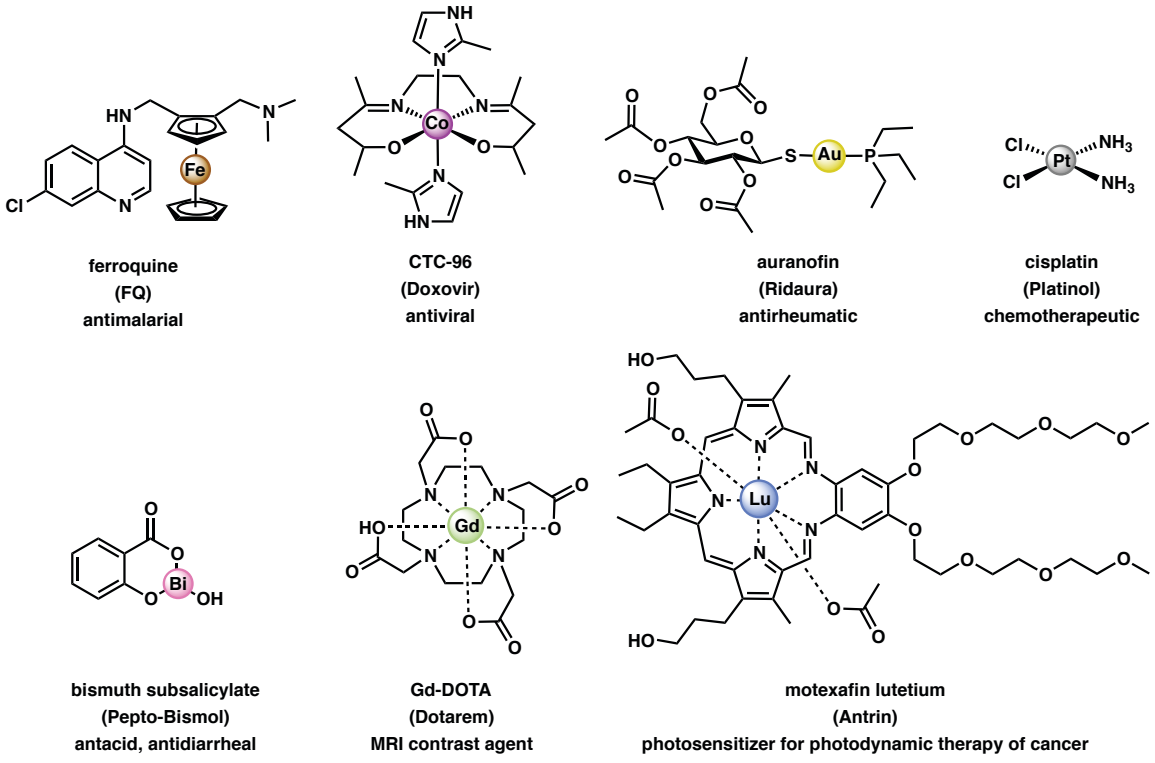

Figure 1.3. A selection of metallopharmaceutical complexes that employ metals from across the periodic table and serve various functions. These compounds are either in clinical trials or approved.

By studying the design elements and performance of these metal-based complexes, these concepts can be expanded to the development of metal-organic materials where solid-state formulations could be advantageous in offering new ways to control the pharmacokinetic profile of a drug. For instance, solid formulations can be designed to dissolve selectively under specified conditions to deliver the drug selectively at the desired pH or redox environment. As such, there are several design strategies that have been explored for this purpose (Figure 1.4).

One strategy involves drug delivery by bioactivation of the material, where the dissolution of the material and resulting release of the ligand is therapeutic. The drug can also be encapsulated within a porous material that releases the cargo under specific conditions. Finally, the metal within the material can have therapeutic value or act as an imaging agent. Furthermore, these particles can be coated or functionalized with targeting groups to improve retention of cargo until the target site is reached.

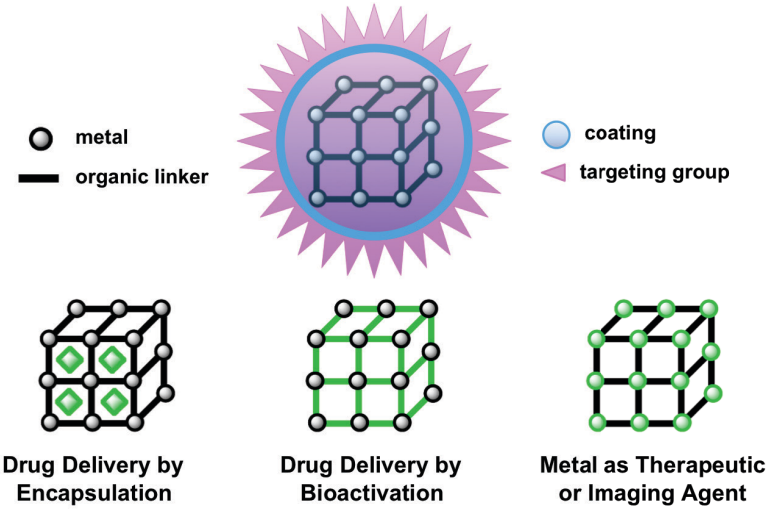

Figure 1.4. Drug delivery strategies with metal-organic materials.

Control of particle size is another important design consideration in developing drug delivery materials, as this can influence biodistribution. For instance, intravenous, intranasal, subcutaneous, and intraocular routes of administration may require use of nano- or microparticles in order to avoid tissue damage. Consistent particle size is also required for production of stable and reproducible formulations as patches, pellets, tablets, injectables, and more. For metal-organic materials, there are several synthetic techniques one can use to control particle size, which include water-in-oil microemulsions, microwave-assisted syntheses, and both solvothermal and hydrothermal conditions.[44] Mechanical techniques such as solvent-assisted ball-milling can also be used to reduce particle size.[45]

Many metal-organic materials can also be prepared as nanoparticles. This size regime is important for biomedical applications, as one can take advantage of the enhanced permeation and retention effect.[46] While small drugs can diffuse similarly through normal

and tumor tissue, nanoparticles in the 10-100 nm regime can selectively diffuse through the leaky vasculature of tumors to accumulate in cancerous tissues. In this way, the therapeutic cargo in the nanoparticles can be delivered selectively to the target site, thereby reducing the necessary dose and off-target side effects. A number of archetypal metal-organic frameworks were prepared as nanoparticles and tested for toxicity levels in zebrafish embryos, and they were found to be well tolerated in the organism.[47]

1.3.1 Drug Delivery by Bioactivation

The administration of biologically active compounds as prodrugs can greatly enhance their performance by increasing circulation time, absorption, and potency while protecting the active forms of the molecules from degradation. Metal-organic compounds provide an attractive approach to prodrug design due to their inherent modularity and diversity. A wide array of compounds can be made by coordinating Lewis basic functional groups of drugs to biocompatible elements, where the properties of the new hybrid material can be used to improve the performance of the drug by masking reactive functional groups, minimizing off-target interactions, and tuning the rate of drug release. While simple salts are commonly used in drug formulation, drugs with two or more coordinating groups can also be used to form extended metal-organic networks. Depending on the distance and orientation of the coordinating groups, as well as the metal and synthetic conditions used, these materials can be prepared as one-dimensional chains, two-dimensional sheets, or three-dimensional structures. These materials can be amorphous or crystalline, making coordination polymers or coordination solids, respectively. Furthermore, these three-dimensional materials can either be densely packed or made porous upon removal of guest solvents to yield an important class of materials known as metal-organic frameworks.

Currently, there are only a few known examples of metal-organic frameworks (MOFs) that utilize a bioactive molecule as the linker for the material. The first reported example is from the Serre group, where they prepared a MOF using Fe(III) and nicotinic acid, which has pellagra-curative, vasodilating, and antilipemic properties.[48] Since then, a few other MOFs with bioactive linkers have been published including ones made of zinc and the iron chelator deferiprone,[49] magnesium and the antioxidant gallate,[50] and zinc and curcumin.[51] Coordination solids have also been prepared similarly with thiopurine antimetabolites[52-54] and the chemotherapeutic letrozole.[55-57]

Zeolitic imidazolate frameworks (ZIFs)[58,59] are a subclass of metal-organic frameworks that assemble to form the same structure types found in zeolites, which are porous aluminosilicate materials. These same topologies are observed between ZIFs and zeolites because the metal-imidazole-metal bond angle in ZIFs is similar to the silicon-oxygen-silicon bond angle of 145° seen in zeolites. A large family of ZIFs has been synthesized from diverse ligands containing an imidazole moiety, including some based on benzimidazole[60] and purine[61] (Figure 1.5). These examples of ZIFs are intriguing because purine derivatives are an important class of biological molecules, some of which have therapeutic effects.

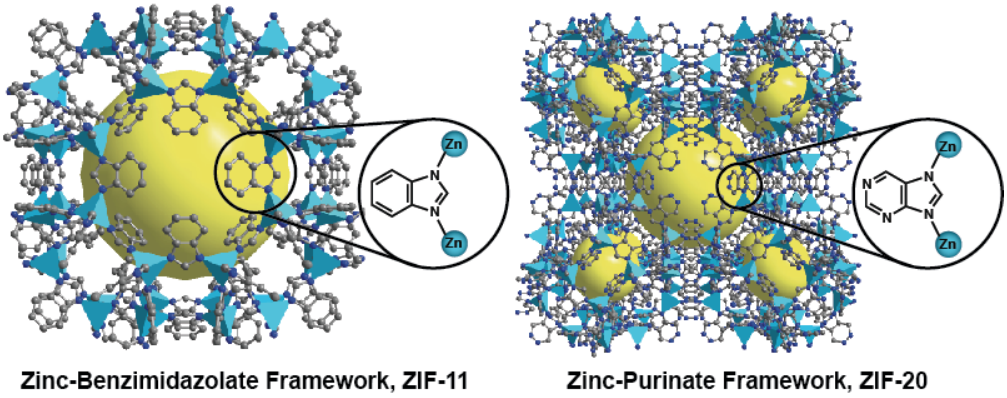

Figure 1.5. Structures of known Zn-based zeolitic imidazolate frameworks, ZIF-11 and ZIF-20, with inset showing metal binding motif.

Thiopurines are antimetabolites that have been widely used in the treatment of leukemia, autoimmune disorders, and organ transplants due to their immunosuppresant and antineoplastic effects. The structures of the thiopurines 6-mercaptopurine and 6-thioguanine are shown in Figure 1.6, along with other imidazole derivatives. Despite their widespread use, thiopurines have several limitations including low bioavailability, short half-life, and off-target effects. These issues could potentially be mitigated by metal-based delivery systems that could mask the sulfur group, for example, and avoid inactivation pathways in the body that involve methylation[62] or oxidation[63] of the thiol.

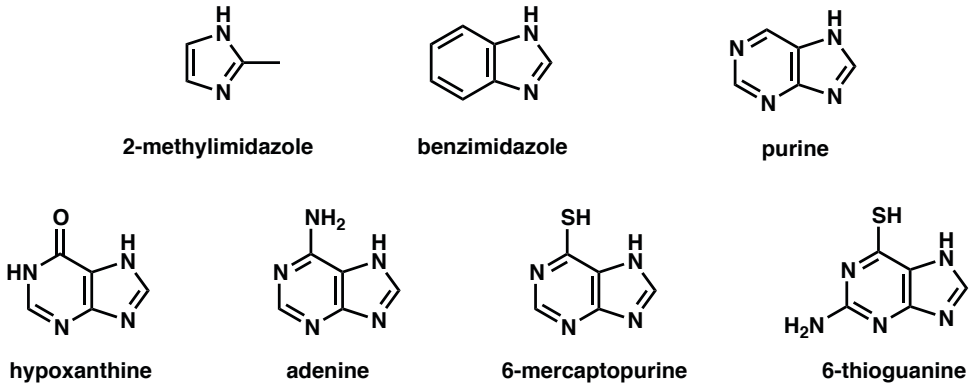

Figure 1.6. Imidazole-based ligands as candidates for coordination solids. Top: ligands known to make zeolitic imidazolate frameworks (ZIFs); the most common Zn-ZIFs for these ligands are ZIF-8, ZIF-11, and ZIF-20, respectively. Bottom: purine derivatives as potential ligands for ZIFs or other extended structures.

Several cobalt-thioguanine chains have been reported (Figure 1.7).[52] While the chains were studied for their magnetic properties, they were not evaluated as a platform for drug release, which could be a promising avenue to explore. Furthermore, an example of a hypoxanthine framework[64,65] with coordination through multiple donor groups suggests that chains of substituted purines could be extended to form higher order structures.

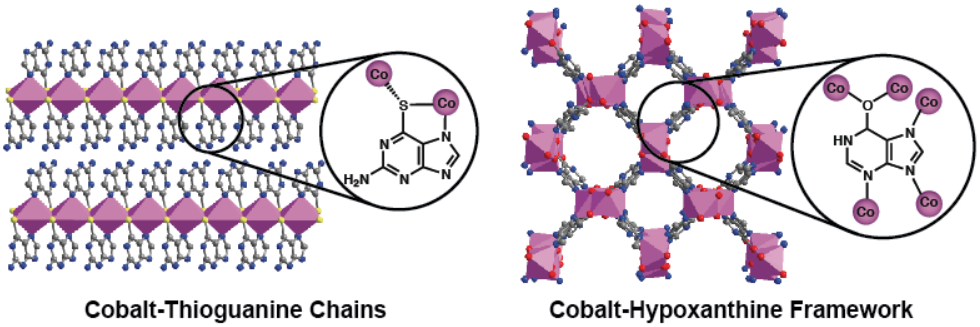

Figure 1.7. Structures of known coordination solids featuring purine derivatives as ligands. The insets show metal binding motifs to the ligand.

1.3.2 Drug Delivery by Encapsulation

Porous metal-organic frameworks (MOFs) are tunable platforms that can be used to encapsulate and deliver a wider range of drugs. They are often biodegradable micro- or meso-porous hybrid solids that possess a vast structural and chemical diversity. A wide array of MOFs can be made from biocompatible elements across the periodic table such as iron, zinc, and magnesium. A number of archetypal metal-organic frameworks have been tested for toxicity in zebrafish embryos, and they were found to be well tolerated by the organism.[47] The combination of such metals with multidentate organic ligands provides an amphiphilic environment that is suitable for the loading and controlled release of a wide range of drug molecules. As such, MOFs can be tuned and optimized for delivery of the desired agent.

There are several approaches that have been employed to load drugs into MOFs including non-covalent drug encapsulation,[66-70] post-synthetic functionalization of the MOF linker,[71] framework amorphization after loading,[72] "ship in a bottle",[73] and "bottle around ship"[74] strategies. There are also a few examples where the drug is used as a ligand to bind to open metal sites within a MOF.[67,75,76] A few of these strategies will be discussed in greater detail below.

The Yaghi lab cleverly made an edible MOF dubbed CD-MOF-1, which is composed of the sugar γ-cyclodextrin linked by potassium ions.[77] This material can be made using food grade reagents such as KCl salt substitute as the metal source and bottled water and Everclear grain spirit as the solvents. The high symmetry of the cyclodextrin facilitated the formation of a highly porous material with a Langmuir surface area of 1320 m^2 g^{-1}. While it is likely to be readily soluble under physiological conditions due to the weaker coordination strength of monocationic potassium, this study sets an important precedent for synthesis and design of biocompatible MOFs with low-toxicity reagents.

A benchmark study in the MOF drug delivery field came from the Serre group, where a series of iron frameworks were used to encapsulate a variety of therapeutic molecules which ranged from polar to nonpolar compounds, including antitumoural and retroviral drugs.[67] These biocompatible porous frameworks were prepared as nanoparticles and surfaces were also functionalized with silica to minimize aggregation. In addition to their

high loadings, these platforms may be useful as both therapeutics and diagnostic tools, since the iron compounds could also be followed by MRI.

A prototypical metal-organic framework known as ZIF-8 (Figure 1.8) was also found to have a high capacity for loading the small anticancer drug 5-fluorouracil.[78] This study establishes that ZIF-8 exhibits remarkable stability at neutral and slightly basic conditions but degrades under acidic conditions. The ability to use pH to trigger degradation of the framework sets an important precedent for using these materials for drug delivery in cancer applications, as the pH differences in tumor tissue and healthy tissue could be exploited for targeted release. Additionally, differences in endosomal pH could also be explored. ZIF-8 has also been used for the delivery of other compounds including caffeine,[74] fluorescein, camptothecin, and iron oxide nanoparticles.[70]

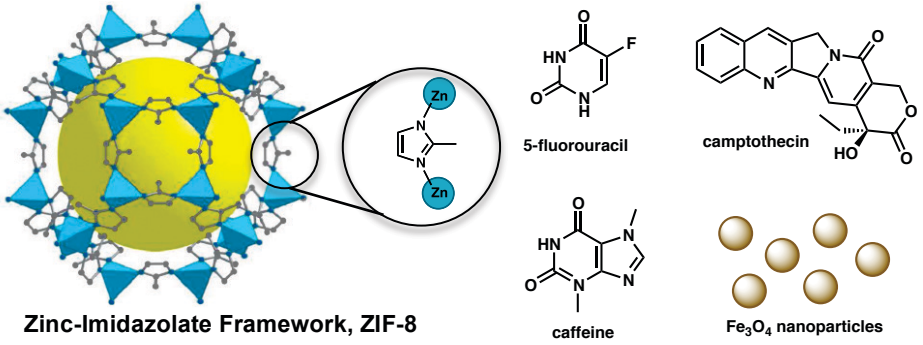

Figure 1.8. Left: Structure of ZIF-8 with inset showing metal binding motif of the ligand. Right: Drugs and other agents encapsulated by ZIF-8.

The MOF-74 structure type forms the basis for an interesting family of metal-organic frameworks that are made from dicationic metals and the ligand 2,5-dioxido-1,4-benzenedicarboxylate ($dobdc^{4-}$).[79-83] Yaghi and coworkers have created a vast library of isoreticular MOF-74 analogs that have variable pore widths ranging from 14 Å to 98 Å.[84] This was achieved elongating the ligand along one axis, adding progressively more phenylene rings up to a total of eleven rings while keeping the same salicylic acid functional groups on the ends to coordinate to the metals in the same way as the original and form the expanded frameworks. With such large pore sizes, they have been able to encapsulate large biomolecules including myoglobin and green fluorescent protein, which are both about 35 x 45 Å along their longest axes.

These frameworks all have hexagonal channels and the metal centers at the vertices are octahedral, with phenoxides and carboxylates from $dobdc^{4-}$ occupying five sites and a solvent molecule is bound at the sixth axial site. By heating under vacuum, the solvent molecule can be removed, generating coordinatively unsaturated open metal-sites after "activating" the material. Due to the square-pyramidal geometry imposed on the metal due to the constraints of the framework ligands, the axial position of the metal is poised to interact with any incoming ligand. This property was employed by the Long group to bind the gas molecule nitric oxide (NO), which has therapeutic effects in small doses, in

the Fe_2(dobdc) framework for slow release of NO.[76] Another group oxidized the Fe_2(dobdc) framework to produce a cationic version of the framework in order strongly bind anionic drugs such as ibuprofen.[75]

Taken together, the expanded MOF-74 series represents a promising set of materials for drug delivery, as the pore size can be tuned to accommodate drugs and biomolecules of varying size. Furthermore, the open metal site could be utilized to influence the rate of release by modulating the strength of the interaction between drug and framework.

1.4 Outlook

In the current study, metal-based compounds were used in various capacities to improve on existing diagnostic and therapeutic tools (Figure 1.9). Chapter 2 will focus on the underlying mechanism involved in the selective precipitation of infectious scrapie prions by phosphotungstate anions. Chapter 3 will describe the synthesis, structures, and release properties of calcium-olsalazine coordination solids for pH-triggered drug delivery in the colon. Finally, Chapter 4 will introduce a new family of porous olsalazine frameworks with the MOF-74 structure type that exhibit high surface areas, strong hydrogen binding, and can serve as platforms for delivery of phenethylamine and other drugs.

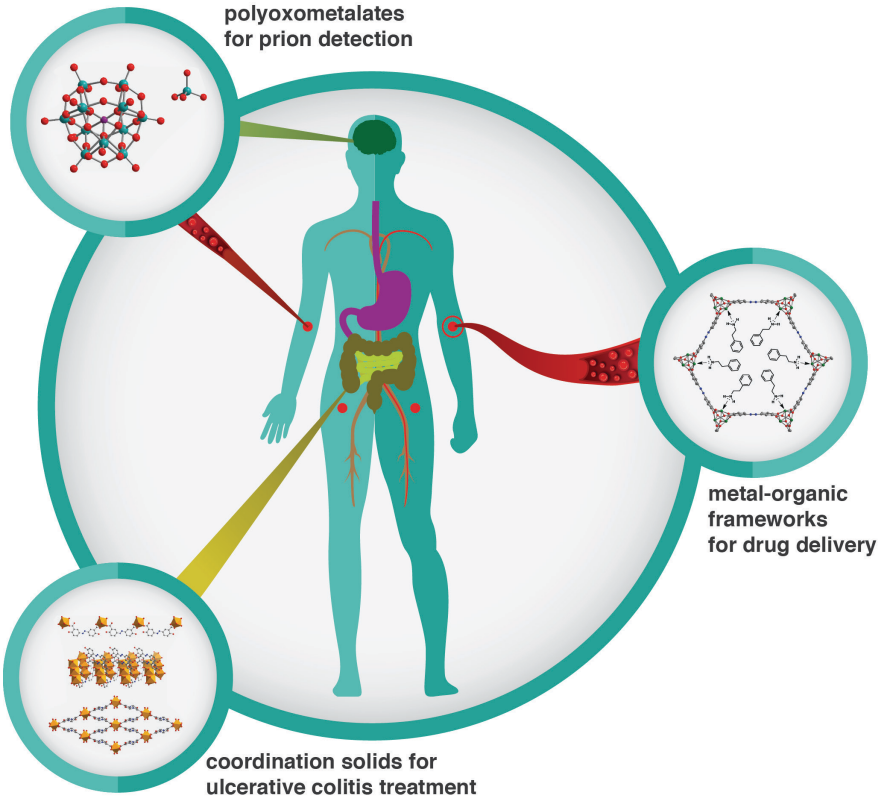

Figure 1.9. Overview depicting the three main contributions of this work to the field of medicinal inorganic chemistry.

1.5 References

(1) Meyer-Luehmann, M., Coomaraswamy, J., Bolmont, T., Kaeser, S., Schaefer, C., Kilger, E., Neuenschwander, A., Abramowski, D., Frey, P., Jaton, A. L., Vigouret, J.-M., Paganetti, P., Walsh, D. M., Mathews, P. M., Ghiso, J., Staufenbiel, M., Walker, L. C., and Jucker, M. (2006) Exogenous induction of cerebral beta-amyloidogenesis is governed by agent and host. *Science 313*, 1781–1784.
(2) Stöhr, J., Watts, J. C., Mensinger, Z. L., Oehler, A., Grillo, S. K., DeArmond, S. J., Prusiner, S. B., and Giles, K. (2012) Purified and synthetic Alzheimer's amyloid beta (Aβ) prions. *Proc. Natl. Acad. Sci. U.S.A. 109*, 11025–11030.
(3) Luk, K. C., Kehm, V. M., Zhang, B., O'Brien, P., Trojanowski, J. Q., and Lee, V. M. Y. (2012) Intracerebral inoculation of pathological α-synuclein initiates a rapidly progressive neurodegenerative α-synucleinopathy in mice. *J. Exp. Med. 209*, 975–986.
(4) Watts, J. C., Giles, K., Oehler, A., Middleton, L., Dexter, D. T., Gentleman, S. M., DeArmond, S. J., and Prusiner, S. B. (2013) Transmission of multiple system atrophy prions to transgenic mice. *Proc. Natl. Acad. Sci. U.S.A. 110*, 19555–19560.
(5) Clavaguera, F., Akatsu, H., Fraser, G., Crowther, R. A., Frank, S., Hench, J., Probst, A., Winkler, D. T., Reichwald, J., Staufenbiel, M., Ghetti, B., Goedert, M., and Tolnay, M. (2013) Brain homogenates from human tauopathies induce tau inclusions in mouse brain. *Proc. Natl. Acad. Sci. U.S.A. 110*, 9535–9540.
(6) Sanders, D. W., Kaufman, S. K., DeVos, S. L., Sharma, A. M., Mirbaha, H., Li, A., Barker, S. J., Foley, A. C., Thorpe, J. R., Serpell, L. C., Miller, T. M., Grinberg, L. T., Seeley, W. W., and Diamond, M. I. (2014) Distinct tau prion strains propagate in cells and mice and define different tauopathies. *Neuron 82*, 1271–1288.
(7) Wille, H., Bian, W., McDonald, M., Kendall, A., Colby, D. W., Bloch, L., Ollesch, J., Borovinskiy, A. L., Cohen, F. E., Prusiner, S. B., and Stubbs, G. (2009) Natural and synthetic prion structure from X-ray fiber diffraction. *Proc. Natl. Acad. Sci. U.S.A. 106*, 16990–16995.
(8) Govaerts, C., Wille, H., Prusiner, S. B., and Cohen, F. E. (2004) Evidence for assembly of prions with left-handed beta-helices into trimers. *Proc. Natl. Acad. Sci. 101*, 8342–8347.
(9) Smirnovas, V., Baron, G. S., Offerdahl, D. K., Raymond, G. J., Caughey, B., and Surewicz, W. K. (2011) Structural organization of brain-derived mammalian prions examined by hydrogen-deuterium exchange. *Nat. Struct. Mol. Biol. 18*, 504–506.
(10) Wille, H., Shanmugam, M., Murugesu, M., Ollesch, J., Stubbs, G., Long, J. R., Safar, J. G., and Prusiner, S. B. (2009) Surface charge of polyoxometalates modulates polymerization of the scrapie prion protein. *Proc. Natl. Acad. Sci. U.S.A. 106*, 3740–3745.
(11) Liu, H., Farr-Jones, S., Ulyanov, N. B., Llinas, M., Marqusee, S., Groth, D., Cohen, F. E., Prusiner, S. B., and James, T. L. (1999) Solution structure of syrian hamster prion protein rPrP(90−231). *Biochemistry 38*, 5362–5377.
(12) B, D. G., Kumar, A., Modi, M. C., Awale, M. M., Patel, H. B., and Mody, S. K. (2013) Transmissible spongiform encephalopathies affecting humans. *ISRN Infect. Dis. 2013*, 1–11.
(13) Rhule, J. T., Hill, C. L., Judd, D. A., and Schinazi, R. F. (1998) Polyoxometalates in medicine. *Chem. Rev. 98*, 327–358.

(14) Keggin, J. F. (1933) Structure of the molecule of 12-phosphotungstic acid. *Nature 131*, 908–909.
(15) Safar, J., Wille, H., Itri, V., Groth, D., Serban, H., Torchia, M., Cohen, F. E., and Prusiner, S. B. (1998) Eight prion strains have PrP^{Sc} molecules with different conformations. *Nat. Med. 4*, 1157–1165.
(16) White, A. R., Enever, P., Tayebi, M., Mushens, R., Linehan, J., Brandner, S., Anstee, D., Collinge, J., and Hawke, S. (2003) Monoclonal antibodies inhibit prion replication and delay the development of prion disease. *Nature 422*, 80–83.
(17) Hill, A. F., Butterworth, R. J., Joiner, S., Jackson, G., Rossor, M. N., Thomas, D. J., Frosh, A., Tolley, N., Bell, J. E., Spencer, M., King, A., Al-Sarraj, S., Ironside, J. W., Lantos, P. L., and Collinge, J. (1999) Investigation of variant Creutzfeldt-Jakob disease and other human prion diseases with tonsil biopsy samples. *Lancet 353*, 183–189.
(18) Glatzel, M., Abela, E., Maissen, M., and Aguzzi, A. (2003) Extraneural pathologic prion protein in sporadic Creutzfeldt-Jakob disease. *N. Engl. J. Med. 349*, 1812–1820.
(19) Wroe, S. J., Pal, S., Siddique, D., Hyare, H., Macfarlane, R., Joiner, S., Linehan, J. M., Brandner, S., Wadsworth, J. D. F., Hewitt, P., and Collinge, J. (2006) Clinical presentation and pre-mortem diagnosis of variant Creutzfeldt-Jakob disease associated with blood transfusion: a case report. *Lancet 368*, 2061–2067.
(20) Saa, P., Castilla, J., and Soto, C. (2006) Ultra-efficient replication of infectious prions by automated protein misfolding cyclic amplification. *J. Biol. Chem. 281*, 35245–35252.
(21) Huang, H. S., Rendulich, J., Stevenson, D., O'Rourke, K., and Balachandran, A. (2005) Evaluation of Western blotting methods using samples with or without sodium phosphotungstic acid precipitation for diagnosis of scrapie and chronic wasting disease. *Can. J. Vet. Res. 69*, 193–199.
(22) Wadsworth, J., Joiner, S., Hill, A. F., Campbell, T. A., Desbruslais, M., Luthert, P. J., and Collinge, J. (2001) Tissue distribution of protease resistant prion protein in variant Creutzfeldt-Jakob disease using a highly sensitive immunoblotting assay. *Lancet 358*, 171–180.
(23) Prusiner, S. B., McKinley, M. P., Bowman, K. A., Bolton, D. C., Bendheim, P. E., Groth, D. F., and Glenner, G. G. (1983) Scrapie prions aggregate to form amyloid-like birefringent rods. *Cell 35*, 349–358.
(24) McKinley, M. P., Bolton, D. C., and Prusiner, S. B. (1983) Fibril-like structures in preparations of scrapie prions purified from hamster brain. *Proc. - Electron Microsc. Soc. Am.* 802–803.
(25) Sim, V. L., and Caughey, B. (2009) Ultrastructures and strain comparison of under-glycosylated scrapie prion fibrils. *Neurobiol. Aging 30*, 2031–2042.
(26) Lee, I. S., Long, J. R., Prusiner, S. B., and Safar, J. G. (2005) Selective precipitation of prions by polyoxometalate complexes. *J. Am. Chem. Soc. 127*, 13802–13803.
(27) Bennion, B. J., and Daggett, V. (2002) Protein conformation and diagnostic tests: The prion protein. *Clin. Chem. 48*, 2105–2114.
(28) Birkmann, E., Henke, F., Funke, S. A., Bannach, O., Riesner, D., and Willbold, D. (2008) A highly sensitive diagnostic assay for aggregate-related diseases, including prion diseases and Alzheimer's disease. *Rejuvenation Res. 11*, 359–363.
(29) Bannach, O., Birkmann, E., Reinartz, E., Jaeger, K.-E., Langeveld, J. P. M., Rohwer, R. G., Gregori, L., Terry, L. A., Willbold, D., and Riesner, D. (2012) Detection of prion

protein particles in blood plasma of scrapie infected sheep. *PLoS ONE, 7*, e36620.
(30) Levine, D. J., Stöhr, J., Falese, L. E., Ollesch, J., Wille, H., Prusiner, S. B., and Long, J. R. (2015) Mechanism of scrapie prion precipitation with phosphotungstate anions. *ACS Chem. Biol. 10*, 1269–1277.
(31) Forte, G., Alimonti, A., Violante, N., Di Gregorio, M., Senofonte, O., Petrucci, F., Sancesario, G., and Bocca, B. (2005) Calcium, copper, iron, magnesium, silicon and zinc content of hair in Parkinson's disease. *J. Trace Elem. Med. Biol. 19*, 195–201.
(32) Gh Popescu, B. F., George, M. J., Bergmann, U., Garachtchenko, A. V., Kelly, M. E., McCrea, R. P. E., Lüning, K., Devon, R. M., George, G. N., Hanson, A. D., Harder, S. M., Chapman, L. D., Pickering, I. J., and Nichol, H. (2009) Mapping metals in Parkinson's and normal brain using rapid-scanning x-ray fluorescence. *Phys. Med. Biol. 54*, 651–663.
(33) Matusch, A., Depboylu, C., Palm, C., Wu, B., Höglinger, G. U., Schäfer, M. K.-H., and Becker, J. S. (2010) Cerebral bioimaging of Cu, Fe, Zn, and Mn in the MPTP mouse model of Parkinson's disease using laser ablation inductively coupled plasma mass spectrometry (LA-ICP-MS). *J. Am. Soc. Mass Spectrom. 21*, 161–171.
(34) Duce, J. A., Bush, A. I., and Adlard, P. A. (2011) Role of amyloid-β–metal interactions in Alzheimer's disease. *Future Neurol. 6*, 641–659.
(35) Millhauser, G. L. (2007) Copper and the prion protein: methods, structures, function, and disease. *Annu. Rev. Phys. Chem. 58*, 299–320.
(36) Sigurdsson, E. M., Brown, D. R., Alim, M. A., Scholtzova, H., Carp, R., Meeker, H. C., Prelli, F., Frangione, B., and Wisniewski, T. (2003) Copper chelation delays the onset of prion disease. *J. Biol. Chem. 278*, 46199–46202.
(37) Bareggi, S. R., and Cornelli, U. (2012) Clioquinol: review of its mechanisms of action and clinical uses in neurodegenerative disorders. *CNS Neurosci. Ther. 18*, 41–46.
(38) Ritchie, C. W., Bush, A. I., Mackinnon, A., Macfarlane, S., Mastwyk, M., MacGregor, L., Kiers, L., Cherny, R., Li, Q.-X., Tammer, A., Carrington, D., Mavros, C., Volitakis, I., Xilinas, M., Ames, D., Davis, S., Beyreuther, K., Tanzi, R. E., and Masters, C. L. (2003) Metal-protein attenuation with iodochlorhydroxyquin (clioquinol) targeting Abeta amyloid deposition and toxicity in Alzheimer disease: a pilot phase 2 clinical trial. *Arch. Neurol. 60*, 1685–1691.
(39) Lannfelt, L., Blennow, K., Zetterberg, H., Batsman, S., Ames, D., Harrison, J., Masters, C. L., Targum, S., Bush, A. I., Murdoch, R., Wilson, J., and Ritchie, C. W. (2008) Safety, efficacy, and biomarker findings of PBT2 in targeting Aβ as a modifying therapy for Alzheimer's disease: a phase IIa, double-blind, randomised, placebo-controlled trial. *Lancet 7*, 779–786.
(40) Jankovic, J., and Sherer, T. (2014) The future of research in Parkinson disease. *JAMA Neurol. 71*, 1351–1352.
(41) Domarle, O., Blampain, G., Agnaniet, H., Nzadiyabi, T., Lebibi, J., Brocard, J., Maciejewski, L., Biot, C., Georges, A. J., and Millet, P. (1998) In vitro antimalarial activity of a new organometallic analog, ferrocene-chloroquine. *Antimicrob. Agents Chemother. 42*, 540–544.
(42) Biot, C., Nosten, F., Fraisse, L., and Ter-Minassian, D. (2011) The antimalarial ferroquine: from bench to clinic. *Parasite 18*, 207–214.
(43) Mjos, K. D., and Orvig, C. (2014) Metallodrugs in medicinal inorganic chemistry. *Chem. Rev. 114*, 4540–4563.

(44) Stock, N., and Biswas, S. (2012) Synthesis of metal-organic frameworks (MOFs): routes to various MOF topologies, morphologies, and composites. *Chem. Rev. 112*, 933–969.
(45) Kundu, T., Mitra, S., Patra, P., Goswami, A., Díaz Díaz, D., and Banerjee, R. (2014) Mechanical downsizing of a gadolinium(III)-based metal-organic framework for anticancer drug delivery. *Chemistry 20*, 10514–10518.
(46) Maeda, H., Wu, J., Sawa, T., Matsumura, Y., and Hori, K. (2000) Tumor vascular permeability and the EPR effect in macromolecular therapeutics: a review. *J. Control. Release 65*, 271–284.
(47) Ruyra, À., Yazdi, A., Espín, J., Carné-Sánchez, A., Roher, N., Lorenzo, J., Imaz, I., and Maspoch, D. (2015) Synthesis, culture medium stability, and in vitro and in vivo zebrafish embryo toxicity of metal-organic framework nanoparticles. *Chemistry 21*, 2508–2518.
(48) Miller, S. R., Heurtaux, D., Baati, T., Horcajada, P., Grenèche, J.-M., and Serre, C. (2010) Biodegradable therapeutic MOFs for the delivery of bioactive molecules. *Chem. Commun. 46*, 4526–4528.
(49) Burrows, A. D., Jurcic, M., Keenan, L. L., Lane, R. A., Mahon, M. F., Warren, M. R., Nowell, H., Paradowski, M., and Spencer, J. (2013) Incorporation by coordination and release of the iron chelator drug deferiprone from zinc-based metal–organic frameworks. *Chem. Commun. 49*, 11260–11262.
(50) Cooper, L., Hidalgo, T., Gorman, M., Lozano-Fernández, T., Simón-Vázquez, R., Olivier, C., Guillou, N., Serre, C., Martineau, C., Taulelle, F., Damasceno-Borges, D., Maurin, G., González-Fernández, Á., Horcajada, P., and Devic, T. (2015) A biocompatible porous Mg-gallate metal-organic framework as an antioxidant carrier. *Chem. Commun. 51*, 5848–5851.
(51) Su, H., Sun, F., Jia, J., He, H., Wang, A., and Zhu, G. (2015) A highly porous medical metal-organic framework constructed from bioactive curcumin. *Chem. Commun. 51*, 5774–5777.
(52) Amo-Ochoa, P., Alexandre, S. S., Hribesh, S., Galindo, M. A., Castillo, O., Gómez-García, C. J., Pike, A. R., Soler, J. M., Houlton, A., Zamora, F., Harrington, R. W., and Clegg, W. (2013) Coordination chemistry of 6-thioguanine derivatives with cobalt: toward formation of electrical conductive one-dimensional coordination polymers. *Inorg. Chem. 52*, 5290–5299.
(53) Amo-Ochoa, P., Castillo, O., Alexandre, S. S., Welte, L., de Pablo, P. J., Rodríguez-Tapiador, M. I., Gómez-Herrero, J., and Zamora, F. (2009) Synthesis of designed conductive one-dimensional coordination polymers of Ni(II) with 6-mercaptopurine and 6-thioguanine. *Inorg. Chem. 48*, 7931–7936.
(54) Amo-Ochoa, P., Castillo, O., Gómez-García, C. J., Hassanein, K., Verma, S., Kumar, J., and Zamora, F. (2013) Semiconductive and magnetic one-dimensional coordination polymers of Cu(II) with modified nucleobases. *Inorg. Chem. 52*, 11428–11437.
(55) Yuan, R.-X., Xiong, R.-G., Abrahams, B. F., Lee, G.-H., Peng, S.-M., Che, C.-M., and You, X.-Z. (2001) A Cu(I) coordination polymer employing a nonsteroidal aromatase inhibitor letrozole as a building block. *J. Chem. Soc., Dalton Trans.* 2071–2073.
(56) Tang, Y.-Z., Zhou, M., Huang, J., Cao, Z., Qi, T.-T., Huang, G.-H., and Wen, H.-R. (2012) Synthesis, crystal structure, and characterization of three new letrozole

complexes. *Z. anorg. allg. Chem. 638*, 372–376.
(57) Zhao, Y. N., Zhang, C. C., Zhai, Q. G., Li, S. N., and Jiang, Y. C. (2013) Solvent-introduced two novel copper (II)–letrozolate compounds: Solvothermal synthesis, crystal structures and photoluminescence property. *Inorg. Chim. Acta 405*, 176–181.
(58) Banerjee, D., Zhang, Z., Plonka, A. M., Li, J., and Parise, J. B. (2012) A calcium coordination framework having permanent porosity and high CO_2/N_2 selectivity. *Cryst. Growth Des. 12*, 2162–2165.
(59) Zhang, J.-P., Zhang, Y.-B., Lin, J.-B., and Chen, X.-M. (2012) Metal azolate frameworks: From crystal engineering to functional materials. *Chem. Rev. 112*, 1001–1033.
(60) Banerjee, R., Phan, A., Wang, B., Knobler, C., Furukawa, H., O'Keeffe, M., and Yaghi, O. M. (2008) High-throughput synthesis of zeolitic imidazolate frameworks and application to CO_2 capture. *Science 319*, 939–943.
(61) Hayashi, H., Côté, A. P., Furukawa, H., O'Keeffe, M., and Yaghi, O. M. (2007) Zeolite A imidazolate frameworks. *Nat Mater 6*, 501–506.
(62) Krynetski, E. Y., Krynetskaia, N. F., Yanishevski, Y., and Evans, W. E. (1995) Methylation of mercaptopurine, thioguanine, and their nucleotide metabolites by heterologously expressed human thiopurine S-methyltransferase. *Mol. Pharmacol. 47*, 1141–1147.
(63) Lennard, L. (1992) The clinical pharmacology of 6-mercaptopurine. *Eur. J. Clin. Pharmacol. 43*, 329–339.
(64) Patel, D. K., Choquesillo-Lazarte, D., Domínguez-Martín, A., Brandi-Blanco, M. P., González-Pérez, J. M., Castiñeiras, A., and Niclós-Gutiérrez, J. (2011) Chelating ligand conformation driving the hypoxanthine metal binding patterns. *Inorg. Chem. 50*, 10549–10551.
(65) Zhang, X.-H., Hao, Z.-M., and Zhang, X.-M. (2011) Spin canting and metamagnetism in the first hybrid cobalt-hypoxanthine open framework with umr topology. *Chem. Eur. J. 17*, 5588–5594.
(66) Horcajada, P., Serre, C., Vallet-Regí, M., Sebban, M., Taulelle, F., and Férey, G. (2006) Metal–organic frameworks as efficient materials for drug delivery. *Angew. Chem. 118*, 6120–6124.
(67) Horcajada, P., Chalati, T., Serre, C., Gillet, B., Sebrie, C., Baati, T., Eubank, J. F., Heurtaux, D., Clayette, P., Kreuz, C., Chang, J.-S., Hwang, Y. K., Marsaud, V., Bories, P.-N., Cynober, L., Gil, S., Férey, G., Couvreur, P., and Gref, R. (2009) Porous metal-organic-framework nanoscale carriers as a potential platform for drug delivery and imaging. *Nat. Mater. 9*, 172–178.
(68) Wang, H.-N., Meng, X., Yang, G.-S., Wang, X.-L., Shao, K.-Z., Su, Z.-M., and Wang, C.-G. (2011) Stepwise assembly of metal-organic framework based on a metal-organic polyhedron precursor for drug delivery. *Chem. Commun. 47*, 7128–7130.
(69) Sun, C.-Y., Qin, C., Wang, C.-G., Su, Z.-M., Wang, S., Wang, X.-L., Yang, G.-S., Shao, K.-Z., Lan, Y.-Q., and Wang, E.-B. (2011) Chiral nanoporous metal-organic frameworks with high porosity as materials for drug delivery. *Adv. Mater. Weinheim 23*, 5629–5632.
(70) Zhuang, J., Kuo, C.-H., Chou, L.-Y., Liu, D.-Y., Weerapana, E., and Tsung, C.-K. (2014) Optimized metal-organic-framework nanospheres for drug delivery: evaluation of small-molecule encapsulation. *ACS Nano. 8*, 2812–2819.

(71) Taylor-Pashow, K. M. L., Rocca, Della, J., Xie, Z., Tran, S., and Lin, W. (2009) Postsynthetic modifications of iron-carboxylate nanoscale metal-organic frameworks for imaging and drug delivery. *J. Am. Chem. Soc. 131*, 14261–14263.
(72) Orellana-Tavra, C., Baxter, E. F., Tian, T., Bennett, T. D., Slater, N. K. H., Cheetham, A. K., and Fairen-Jimenez, D. (2015) Amorphous metal-organic frameworks for drug delivery. *Chem. Commun. 51*, 13878–13881.
(73) di Nunzio, M. R., Agostoni, V., Cohen, B., Gref, R., and Douhal, A. (2014) A "ship in a bottle" strategy to load a hydrophilic anticancer drug in porous metal organic framework nanoparticles: Efficient encapsulation, matrix stabilization, and photodelivery. *J. Med. Chem. 57*, 411–420.
(74) Liédana, N., Galve, A., Rubio, C., Téllez, C., and Coronas, J. (2012) CAF@ZIF-8: One-Step Encapsulation of Caffeine in MOF. *ACS Appl. Mater. Interfaces 4*, 5016–5021.
(75) Hu, Q., Yu, J., Liu, M., Liu, A., Dou, Z., and Yang, Y. (2014) A low cytotoxic cationic metal-organic framework carrier for controllable drug release. *J. Med. Chem. 57*, 5679–5685.
(76) Bloch, E. D., Queen, W. L., Chavan, S., Wheatley, P. S., Zadrozny, J. M., Morris, R., Brown, C. M., Lamberti, C., Bordiga, S., and Long, J. R. (2015) Gradual release of strongly bound nitric oxide from $Fe_2(NO)_2$(dobdc). *J. Am. Chem. Soc. 137*, 3466–3469.
(77) Smaldone, R. A., Forgan, R. S., Furukawa, H., Gassensmith, J. J., Slawin, A. M. Z., Yaghi, O. M., and Stoddart, J. F. (2010) Metal-organic frameworks from edible natural products. *Angew. Chem. Int. Ed. 49*, 8630–8634.
(78) Sun, C.-Y., Qin, C., Wang, X.-L., Yang, G.-S., Shao, K.-Z., Lan, Y.-Q., Su, Z.-M., Huang, P., Wang, C.-G., and Wang, E.-B. (2012) Zeolitic imidazolate framework-8 as efficient pH-sensitive drug delivery vehicle. *Dalton Trans. 41*, 6906–4.
(79) Dietzel, P. D. C., Morita, Y., Blom, R., and Fjellvåg, H. (2005) An in situ high-temperature single-crystal investigation of a dehydrated metal–organic framework compound and field-induced magnetization of one-dimensional metal–oxygen chains. *Angew. Chem. 117*, 6512–6516.
(80) Rosi, N. L., Kim, J., Eddaoudi, M., Chen, B., O'Keeffe, M., and Yaghi, O. M. (2005) Rod packings and metal-organic frameworks constructed from rod-shaped secondary building units. *J. Am. Chem. Soc. 127*, 1504–1518.
(81) Dietzel, P. D. C., Panella, B., Hirscher, M., Blom, R., and Fjellvåg, H. (2006) Hydrogen adsorption in a nickel based coordination polymer with open metal sites in the cylindrical cavities of the desolvated framework. *Chem. Commun. 0*, 959–961.
(82) Caskey, S. R., Wong-Foy, A. G., and Matzger, A. J. (2008) Dramatic tuning of carbon dioxide uptake via metal substitution in a coordination polymer with cylindrical pores. *J. Am. Chem. Soc. 130*, 10870–10871.
(83) Bloch, E. D., Murray, L. J., Queen, W. L., Chavan, S., Maximoff, S. N., Bigi, J. P., Krishna, R., Peterson, V. K., Grandjean, F., Long, G. J., Smit, B., Bordiga, S., Brown, C. M., and Long, J. R. (2011) Selective binding of O_2 over N_2 in a redox-active metal-organic framework with open iron(II) coordination sites. *J. Am. Chem. Soc. 133*, 14814–14822.
(84) Deng, H., Grunder, S., Cordova, K. E., Valente, C., Furukawa, H., Hmadeh, M., Gándara, F., Whalley, A. C., Liu, Z., Asahina, S., Kazumori, H., O'Keeffe, M., Terasaki, O., Stoddart, J. F., and Yaghi, O. M. (2012) Large-pore apertures in a series of metal-organic frameworks. *Science 336*, 1018–1023.

Chapter 2: Mechanism of Scrapie Prion Precipitation with Phosphotungstate Anions

2.1 Introduction

The fundamental event in prion diseases caused by the prion protein (PrP) is the misfolding of normal PrP (PrP^C), which leads to progressive neurodegeneration in many mammals.[1] Such diseases include Creutzfeldt–Jakob disease in humans, scrapie in sheep, bovine spongiform encephalopathy in cattle, and chronic wasting disease in deer and elk.[2] In these prion diseases, endogenous PrP^C adopts a self-propagating conformation, designated PrP^{Sc}, which can autocatalytically convert PrP^C molecules into disease-causing PrP^{Sc}.[3,4] PrP misfolding can be caused by genetic mutations, exposure to PrP^{Sc}, or occur spontaneously, resulting in inherited, acquired, or sporadic disease manifestations, respectively.[5] Over time, PrP^{Sc} accumulates and spreads throughout the brain, leading to severe neuronal deterioration, loss of cognitive function, and ultimately death (Figure 2.1). While diseases caused by PrP^{Sc} are rare in humans, biochemical insights into PrP^{Sc} may provide valuable applications to other, more common neurodegenerative disorders. In recent studies, a self-perpetuating prion mechanism has been described for amyloid β peptides in Alzheimer's disease, α-synuclein in Parkinson's disease, and tau in the tauopathies.[6-11]

A detailed knowledge of the structure of PrP^{Sc} would greatly facilitate efforts to prevent, diagnose, and develop therapeutics for prion diseases. PrP^{Sc} is rich in β-sheet content that renders the large aggregates insoluble and thus difficult to characterize by conventional biophysical techniques. Despite several studies employing such techniques as X-ray fiber diffraction,[12] electron microscopy,[13] and hydrogen–deuterium exchange,[14] the structure of PrP^{Sc} remains elusive. Structural models of PrP^{Sc} have been proposed from X-ray fiber diffraction and electron microscopy of prions isolated from brain tissue.[12,15] However, such fibril preparations generally contain large amounts of crystalline lipids, which may obscure structural features of the protein aggregates.

Biophysical studies require the purification of a relatively large amount of PrP^{Sc}. Historically, prion purification and enrichment required a series of time-intensive gradient or differential centrifugation steps, which resulted in highly purified samples but with a low yield.[16-18] A rapid, alternative method employs an inorganic polyoxometalate (POM) complex known as the phosphotungstate anion (PTA, $[PW_{12}O_{40}]^{3-}$). Since the discovery that PTA selectively promotes precipitation of PrP^{Sc} over PrP^C,[19] it has been widely used to isolate PrP^{Sc} from various tissues of prion-infected animals.[20-25] The success of PTA has stimulated efforts to vary the structure, charge, and composition of related complexes to optimize PrP^{Sc} purification[26] and to influence the resulting type of aggregate assemblies.[15]

PTA precipitation has also been used to concentrate PrP^{Sc} for diagnostic purposes.[27] Currently, a definitive diagnosis of prion diseases caused by PrP^{Sc} can only be made post-mortem. Efforts have been made to develop diagnostic tools for detecting PrP^{Sc} in the

blood of humans and cattle,[28,29] and PTA has been used to facilitate detection of very low amounts of PrP^{Sc} in peripheral tissues of patients with Creutzfeldt–Jakob disease.[30] However, achieving a rapid and reliable method for PrP^{Sc} detection has been hampered by difficulties in discriminating infectious PrP^{Sc} from endogenous PrP^{C}, low titers of PrP^{Sc} in blood, and the presence of lipid and protein contaminants that can complicate the accuracy of determinations.[31]

Despite the widespread use of PTA to isolate PrP^{Sc}, the mechanisms by which PTA effectively precipitates PrP^{Sc} are still largely unknown. PTA does not appear to induce a conformational change of PrP^{C} to PrP^{Sc}, since amyloid seeding assays have shown that PTA does not promote conversion of PrP^{C} to PrP^{Sc} in multiple strains of uninfected mice.[27] Using microscopic and immunological techniques, we found that PTA and sarkosyl promoted the formation of fibrils and increased the density of PrP^{Sc} aggregates. $Na_3[PW_{12}O_{40}]$ (NaPTA) decomposed at neutral pH to give a lacunary $[PW_{11}O_{39}]^{7-}$ (PW_{11}) complex and a single orthotungstate $[WO_4]^{2-}$ unit (WO_4). When used as a precipitant, the lacunary PW_{11} complex of PTA resulted in high yields of PrP^{Sc} and decreased neuronal lipid monosialotetrahexosylganglioside (GM1) content in the samples, while WO_4 was less effective at removing GM1 lipids at equivalent concentrations. These results describe several potential mechanisms for the effective precipitation of PrP^{Sc} by PTA (Figure 2.1).

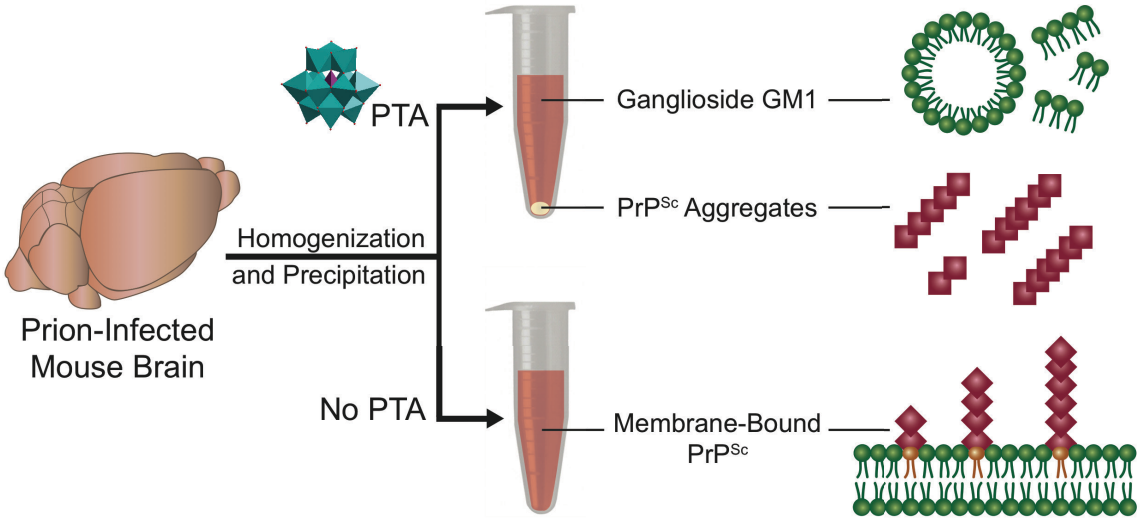

Figure 2.1. Proposed mechanism for the efficacy of the PTA precipitation of scrapie prions from brain homogenate involves the disruption of the PrP^{Sc}–lipid interactions by PTA derivatives to release prion aggregates from buoyant lipid membranes.

2.2 Experimental

2.2.1 Chemicals

NaPTA, sodium tungstate dihydrate, sodium phosphate monobasic, sodium carbonate monobasic,*N*-laurylsarcosine sodium salt (sarkosyl), sucrose, cholera toxin subunit-B peroxidase conjugate, β-mercaptoethanol, trizma hydrochloride, sodium chloride, tween-20, sodium hydroxide, nitric acid, and hydrochloric acid were purchased from Sigma-Aldrich and used without further purification. Deuterium oxide was obtained from Cambridge Isotopes and used as received. Bovine serum albumin (BSA), ABTS substrate, and 8 M GdnHCl were obtained from Thermo Scientific. SDS, 10× TGS running buffer, and 10× Ca^{2+}/Mg^{2+}-free PBS were obtained from Gibco and diluted to the appropriate strength with purified water (18.2 MΩ·cm resistivity). Instant nonfat dry milk was from SACO Foods. Amersham enhanced chemiluminscence (ECL) Western blotting detection reagents were from GE Healthcare. Recombinant mouse PrP(23–230),[32] HRP-conjugated anti-PrP Fab antibody P,[33] and anti-PrP Fab antibodies D18 and HRP-D13[34] were prepared as described.

2.2.2 Prion-Infected Brain Samples

FVB weanling mice (Charles River Laboratories) were inoculated intracerebrally with RML prions prepared from infected CD1 mice. Inoculated mice were sacrificed when symptoms of neurologic dysfunction presented in accordance with protocols approved by the UCSF Institutional Animal Care and Use Committee. The brains were collected and stored at −80 °C. All manipulations of mice, brain tissue, and purified prions were performed in a Biosafety Level 2 facility in accordance with established guidelines from the NIH.

2.2.3 PrP Fibrillization Assays

Brain homogenates (10% w/v) were prepared in Ca^{2+}/Mg^{2+}-free PBS and clarified by centrifugation at 500*g* for 5 min in a tabletop centrifuge. The resulting supernatant was separated into 1-mL aliquots and centrifuged at 100 000*g* for 1 h (Beckman, TLA55 at 48 000 rpm). The high-speed supernatant was discarded, and the pellets remaining in the centrifuge tubes were frozen on ice and stored at −80 °C until use. For the fibrillization assays, brain homogenate samples were resuspended with 200 μL of Ca^{2+}/Mg^{2+}-free PBS with Complete Protease Inhibitor Cocktail (Roche Applied Science, Indianapolis, IN) and then pooled together. The pooled samples were supplemented with increasing concentrations of PTA (0–3.4% w/v), sarkosyl (0–3.5% w/v), or a combination of PTA (0–3.4% w/v) in the presence of 2% w/v sarkosyl. The samples were incubated overnight (16–18 h) at 37 °C under constant shaking (1200 rpm). After incubation, the samples were place on ice, and 50-μL aliquots were taken and analyzed by electron microscopy.

2.2.4 Electron Microscopy

Sample aliquots of 5 μL were adsorbed for 30 s onto Formvar/carbon-coated, 200-mesh copper grids (Ted Pella, Redding, CA) that were glow-discharged prior to use. The grids were then washed briefly with 0.1 and 0.01 M ammonium acetate buffer, pH 7.4, and stained with two 50 μL drops of freshly filtered 2% w/v ammonium molybdate[35] or dried without additional staining. The contrast provided by the bound PTA was sufficient to identify fibrillization products at low magnification.[15] After drying, the samples were

viewed with a FEI Tecnai F20 electron microscope (FEI Company, Hillsborough, OR) at an acceleration voltage of 80 kV. Electron micrographs were recorded on a Gatan (Pleasanton, CA) UltraScan 4000 CCD camera.

2.2.5 Fibril Quantification

The quantification of the PrP^{Sc} fibrillization was performed essentially as described.[15] In brief, 10 electron micrographs were taken at random positions on the grid. Micrographs that contained obvious film defects, dirt particles, and other artifacts were discarded and replaced. All images were taken at a low magnification of 7575× (corresponding to 19.8 Å/pixel) and a higher-than-usual underfocus (5–10 μm) to facilitate the quantification. The micrographs were processed with Adobe Photoshop (San Jose, CA). The number of pixels (representing the area) for each visible fibril in the electron micrographs was determined. Individual fibrils and fibril clusters were selected by using the magic wand tool with a setting of 50–100; the Fresnel fringes caused by the strong underfocus made it easier to delineate each fibril/fibril cluster separately. The histogram menu provided the number of pixels for each particle. Fibrils were classified as such if the length was >40 pixels, equivalent to ~78 nm, and the length/width ratio was at least 2:1. The amount of fibrils was averaged over all 10 micrographs. The stochastic distribution of the fibrils on the support film is reflected in the relatively large standard errors of the mean (SEM).

2.2.6 Sucrose Cushion Centrifugations

Brain homogenate was prepared from RML-infected FVB mice at 20% w/v in Ca^{2+}/Mg^{2+}-free PBS. The homogenate was centrifuged for 5 min at 500*g* at 4 °C, and the pellet was discarded to remove cell debris from the sample. The supernatant was then split into two aliquots, and sarkosyl was added to each aliquot to give a final concentration of 2% w/v sarkosyl. To one sample, 10% PTA solution, pH 7.2, was added (2% final w/v), while the other was left as a control without PTA. The samples were then incubated overnight at 37 °C, and the aliquots were each pipetted onto a two-step sucrose cushion containing 50% sucrose (8 mL) and 80% sucrose layers (2 mL). All sucrose solutions contain 0.5% sarkosyl, 50 mM sodium HEPES, and 1 mM sodium azide. The gradients were centrifuged at 134 000*g* (20 °C) for 16 h in a SW41 Ti swinging bucket rotor (Beckman-Coulter). Fifteen aliquots were taken from each gradient and labeled A–O from low to high density. For fractions A–F, 1 mL samples were collected; for fractions G–O, 500 μL collected. The pellets were resuspended in 1 mL of a 2% sarkosyl solution and labeled as the pellet fraction. All aliquots and gradient pellet samples were analyzed by Western blot using the P-HRP antibody and developed using ECL reagents.

2.2.7 ^{31}P Nuclear Magnetic Resonance

Samples were prepared at 10% w/v PTA in 90:10 H_2O/D_2O mixture and run on a Bruker Avance III NMR spectrometer equipped with a BBO broadband probe operating at 600.13 MHz for ^{1}H and 242.93 MHz for ^{31}P. Sample pH was adjusted with stepwise addition of NaOH and allowed to equilibrate for 1 h before spectra were collected. Additional spectra were collected in more complex buffer solutions containing PBS, sarkosyl, and brain homogenate (Supplementary Figure 2.S3). While the phosphate concentration increased due to the use of PBS as the solvent, the NMR signals corresponding to PTA did not change in these complex buffer solutions.

2.2.8 Preparation of POM Stock Solutions

The 10% w/v (31.6 mM) PTA solutions were prepared by dissolution of NaPTA in deionized water (18.2 MΩ·cm resistivity); the pH of the solution was adjusted to pH 7.1–7.2 with NaOH. $Na_7[PW_{11}O_{39}]$ and $Na_2WO_4 \cdot 2H_2O$ solutions of equivalent concentrations (31.6 mM) were prepared in deionized water, and the pH was adjusted by NaOH or glacial acetic acid to pH 7.1–7.2. The solutions were prepared fresh prior to each experiment.

2.2.9 Synthesis of $Na_7[PW_{11}O_{39}] \cdot 12H_2O$

Procedure was adapted from Brevard et al.[36] Sodium tungstate dihydrate (36.3 g, 0.110 mol) and anhydrous sodium phosphate monobasic (1.38 g, 0.010 mol) were dissolved in 75 mL of deionized water (18.2 MΩ·cm resistivity). The solution was heated to 85–90 °C with vigorous stirring, and concentrated nitric acid was added dropwise to reach pH 4.8. The solution volume was reduced to half by evaporation, and extraction with 3 × 50 mL of acetone afforded the POM in the aqueous layer as a white powder after evaporation of the water.

2.2.10 Preparation of Brain Homogenates for Tungstate Precipitations

Triplicate sets of brain tissue (7 brains/set) from RML-infected FVB mice were thawed and homogenized with Ca^{2+}/Mg^{2+}-free PBS to give a 10% w/v crude brain homogenate. Nuclei and debris were removed by centrifugation at 1500*g* for 5 min, and the supernatant was diluted 1:1 with a sarkosyl detergent solution to a final concentration of 5% brain homogenate in 2% sarkosyl by weight. Samples were stored at −80 °C in 500-μL aliquots.

2.2.11 Tungstate Precipitations from Brain Homogenate

Aliquots (500-μL) of 5% brain homogenate in 2% sarkosyl (w/v) were treated with varying concentrations of tungstates by addition of 0, 8, 16, 32, 64, 96, 128, 192, or 256 μL of the stock solutions at pH 7.1 and a corresponding amount of water to adjust the final volume of each sample to 1012 μL. The samples were incubated at 37 °C with shaking for 1 h and then centrifuged at 14 000*g* for 1 h at room temperature (RT) in a 5415D Eppendorf microcentrifuge equipped with the fixed-angle rotor F-45-24-11. The supernatants were promptly decanted, and the 1.5 mL Eppendorf tubes were left upside-down to facilitate removal of liquid residue from the pellet, which was subsequently removed by cotton swabs. The pellets were stored at −20 °C.

2.2.12 ELISA Plate Preparation

Thermo Immulon 2HB flat-bottom, 96-well microtiter plates were used for ELISA experiments. To each well, 100 μL of 4 μg/mL solution of D18 antibody in 0.1 M carbonate (pH 8.6) was added, and the plates were sealed and incubated with shaking at 4 °C overnight. The plates were washed 5 times with Tris-buffered saline with Tween-20 (TBST) and then blocked with 300 μL/well of 1% BSA in TBST for 1 h at RT. After aspiration of the blocking solution, the plates were sealed and stored at 4 °C until use.

2.2.13 Sandwich ELISA

Three independently prepared sets of POM-precipitated pellets were resuspended in 500 μL of 4 M GdnHCl, heated at 100 °C for 10 min, and cooled on ice for 5 min. The samples were diluted 40-fold with 1% BSA in TBST to prevent antibody denaturation,

and 100 µL of each sample was loaded onto D18-coated plates in triplicate. Each plate also contained a ladder of recombinant mouse PrP(23–230) loaded in known quantities in duplicate or triplicate to establish a standard concentration curve with a four-parameter logistic regression.[37] The plates were incubated overnight at 4 °C and subsequently washed 3× with TBST. The plates were then incubated for 1 h with a 1 µg/mL D13-HRP antibody solution in 1% BSA in PBS, rinsed 3× with TBST, and then developed with ABTS HRP substrate. Plate absorbance was read at 405 nm, and the sample optical densities were correlated to the known calibration curve to determine the level of PrP in each sample. To convert PrP levels from nanograms per well to nanograms per milligram of brain tissue, the well concentrations were multiplied by a factor of 8. The mean level of PrP precipitated at each POM concentration was calculated by taking the average of all samples at the same POM concentration, and the standard error of the mean was determined by taking the standard deviation of the independent averages and dividing by the square-root of three. To calculate the enrichment factor (Equation 2.1) from each POM concentration relative to controls (Table 2.1), the values were normalized to the amount of PrP detected when no POMs were used in the precipitation.

$$\frac{\bar{x}_i}{\bar{x}_c} \pm \frac{\bar{x}_i}{\bar{x}_c}\sqrt{(\bar{x}_i - s_i)^2 + (\bar{x}_c - s_c)^2} \qquad \text{Equation 2.1}$$

where $\bar{x}_i$ = average ng of PrP/mg of brain tissue for POM concentration i, $\bar{x}_c$ = average ng of PrP/mg of brain tissue for control (i = 0 mM POM), s_i = standard error of the mean for POM concentration i, and s_c = standard error of the mean for control (i = 0 mM POM).

2.2.14 Immunoblotting of POM-Precipitated Samples

POM-precipitated pellets were resuspended in 200 µL of SDS sample buffer, diluted 10-fold, heated to 100 °C for 10 min, and allowed to cool to RT. The samples were run on a BioRad Criterion 4–20% polyacrylamide gel, transferred to a PVDF membrane using the iBlot wet transfer system, blocked with a 5% milk solution in TBST, and incubated with 1 mg mL^{-1} D13-HRP antibody overnight at RT. To detect GM1, HRP-conjugated cholera toxin B subunit (Sigma-Aldrich) was added to the D13-HRP-containing milk solution the following day and incubated for 1 h at RT. The membrane was washed 3 times with TBST, incubated with ECL reagents for 1 min, and then developed on film.

2.3 Results and Discussion

2.3.1 PTA and Sarkosyl Promote Formation of PrP^{Sc} Fibrils

In the standard method to precipitate PrP^{Sc} using PTA, prion-infected brain homogenates are incubated with PTA and the detergent sodium lauryl sarcosinate (sarkosyl) in phosphate-buffered saline (PBS) prior to a low-speed centrifugation. To test the influence of each precipitant on the aggregation state of PrP^{Sc}, we incubated brain homogenates (10% w/v) from FVB mice infected with Rocky Mountain Laboratory (RML) scrapie prions with different concentrations of sarkosyl (0–3.5% w/v), PTA (0–3.4% w/v), and combinations of 0–3.4% PTA with 2% sarkosyl. These scrapie-infected mice generally do not show preformed PrP^{Sc} fibrils or amyloid deposits in their brains.[38] The resulting PrP^{Sc} fibrillar aggregates were analyzed by electron microscopy of sample aliquots and

quantified (Figure 2.2a). When neither sarkosyl nor PTA was used, very few fibrils were observed (Figure 2.2b). When used independently, both sarkosyl and PTA induced the formation of large fibrillar structures (Figure 2.2c,d, respectively). With PTA alone, higher concentrations yielded greater numbers of aggregates. The greatest number of fibrils detectable by electron microscopy was found from using a combination of PTA and sarkosyl, with the highest yield of fibrillar aggregates obtained using 2% PTA and 2% sarkosyl (Figure 2.2e), in agreement with established optimal concentrations from earlier studies.[12,15,26]

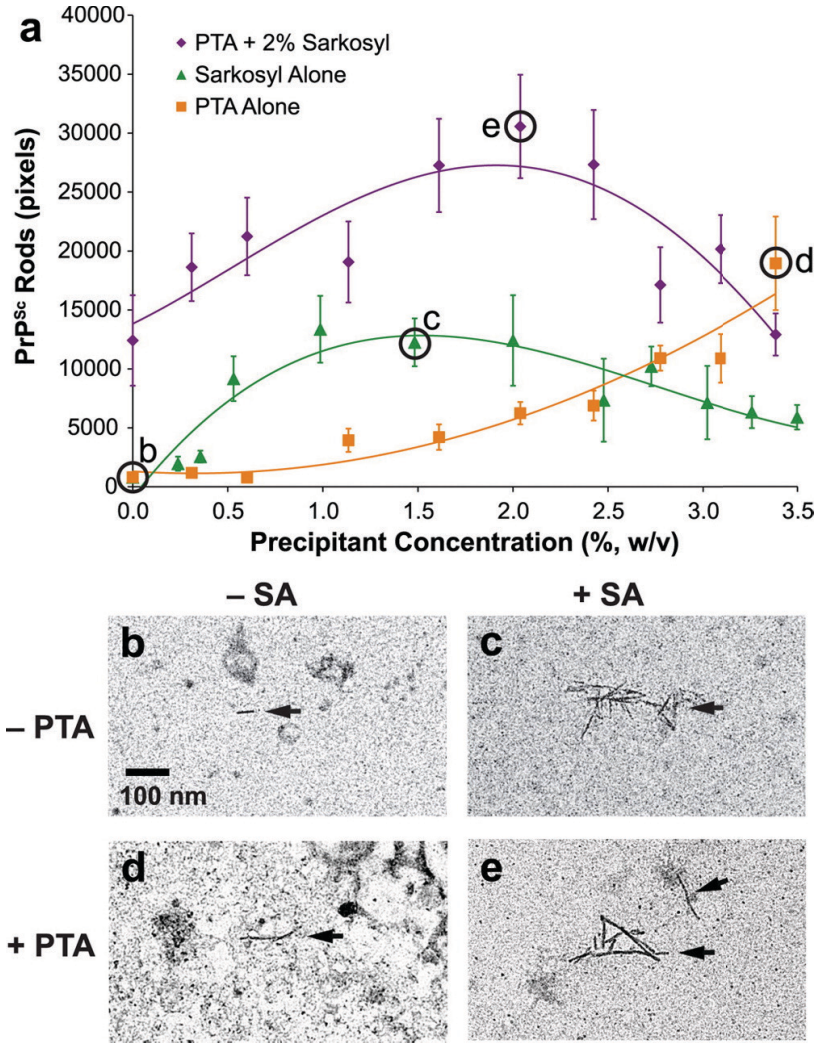

Figure 2.2. Quantification of electron microscopy images (a) shows how preparative methods with no additives (b), sarkosyl detergent alone (c), PTA alone (d), and PTA in combination with sarkosyl (e) influence the amount of PrP^{Sc} fibrils obtained at different reagent concentrations. Error bars in panel a represent the standard error of the mean from 10 representative electron micrographs, and examples of fibrils indicated by the letters in panel a are shown in panels b–e (arrows).

2.3.2 PTA Facilitates PrP^{Sc} Separation from Lipids

We further investigated the influence of PTA and sarkosyl on the hydrodynamic properties of aggregates by centrifugation of RML-infected brain homogenate in a three-step sucrose gradient. Brain homogenate (20% w/v) was prepared from RML-infected mice using PBS and 2% sarkosyl. The homogenate was then incubated at 37 °C overnight with or without 2% PTA, and then 1.5 mL of treated or untreated brain homogenate was loaded onto a sucrose gradient consisting of an 8 mL layer of 50% sucrose above a 2 mL layer of 80% sucrose. After centrifugation at 134 000*g* for 16 h, fractions from lowest to highest density were collected and immunoblotted for PrP levels and for GM1, the main ganglioside in neuronal membranes[39] and a marker for glycolipid raft domains[40,41] (Figure 2.3).

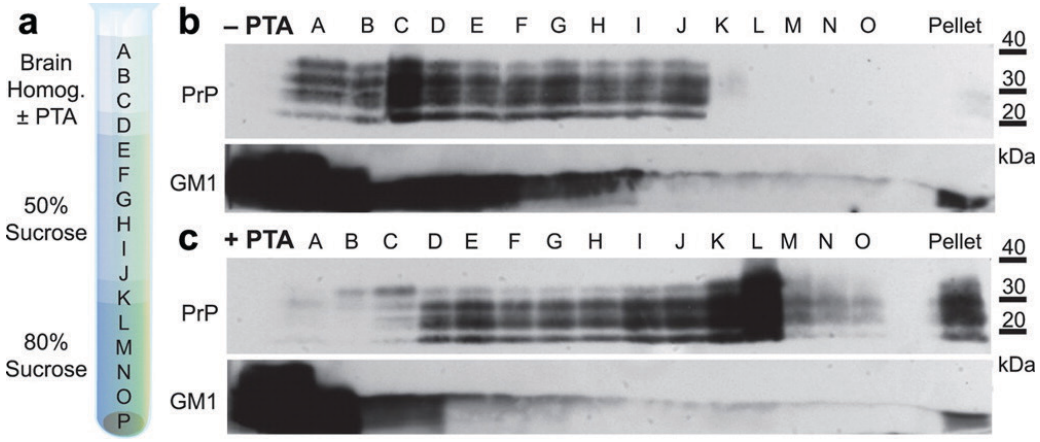

Figure 2.3. Sucrose cushion centrifugations of prion-infected brain homogenates reveal levels of PrP and GM1 by immunoblotting. (a) Schematic representation of the three-step gradient centrifugation, where the brain homogenate was layered on top of sucrose layers of increasing density. The resulting fractions were labeled A–P and correspond to lanes in the immunoblots. (b, c) Western blots of brain homogenate incubated without (b) or with (c) PTA. PrP (upper blots) and GM1 (lower blots) colocalized in the absence of PTA, whereas PrP separated from GM1 in the presence of PTA. Molecular weight markers of migrated protein standards are shown in kilodaltons (kDa).

In the absence of PTA, PrP largely remained in fractions above the 50–80% sucrose interface, with most of the PrP settled at the interface of the aqueous buffer fraction and the first sucrose-containing fraction (Figure 2.4b, lanes C and D). In addition, the highest GM1 content was found to colocalize with PrP in the low-density fractions. This observation is consistent with the presence of a C-terminal glycophosphatidylinositol (GPI) anchor on PrP, which strongly interacts with lipids and increases the buoyancy of both monomeric PrP^{C} and aggregated PrP^{Sc}.[42,43] In the presence of PTA, PrP was found in higher density fractions, with the highest levels found below the 50–80% sucrose interface (Figure 2.4c, lanes K and L) and many aggregates clearly penetrating the 80%

layer. With PTA, GM1 was also separated from the PrP aggregates, as evidenced by GM1 remaining in lower-density fractions while PrP migrated into higher-density fractions, even giving rise to a sizable amount of PrP in the pellet fraction. In this way, PTA also provided effective separation of monomeric PrP^{C} from aggregated PrP^{Sc}, since the buoyant PrP^{C} remained in the less dense GM1-containing fractions while aggregated PrP^{Sc} was more readily precipitated. This effect is further illustrated in samples treated with proteinase K (PK), which degrades PrP^{C} and cleaves PK-resistant PrP^{Sc} into PrP 27–30 (Supplementary Figure 2.S1). Without PTA, the majority of PrP 27–30 was found in the lower density fractions together with GM1 in proteolytically digested samples. Upon addition of PTA, however, PrP 27–30 migrated to the higher density fractions, effectively separating PrP from GM1 lipids, which remained in the low-density fractions.

PTA altered the distribution of PrP and GM1 in sucrose cushion centrifugations, suggesting that PTA may influence the density of PrP aggregates in several different ways. Direct interaction of PrP aggregates with heavy, tungsten-containing compounds like PTA may increase their density and promote the formation of larger PrP^{Sc} aggregates. In order to determine the effects of ionic strength on precipitation efficiency, sucrose cushion centrifugations were also performed on both PK-digested and undigested samples treated with sodium chloride (Supplementary Figure 2.S2). Addition of NaCl facilitated some degree of GM1 separation from PrP in both cases. However, NaCl did not significantly promote precipitation of PrP, suggesting that the efficacy of PTA may involve its direct interaction with PrP rather than simply increasing the ionic strength of the solution.

We speculate that the release of PrP from lipids is also a key factor in promoting fibrillization, as observed in the fibrillization studies using sarkosyl (Figure 2.3). Indeed, transgenic mice expressing PrP without the GPI anchor showed increased propensity to develop amyloid fibrils in their brains.[44,45] These observations suggest that interaction of PrP^{Sc} with lipid membranes may hinder fibril formation, and use of polyanions like PTA may aid in disrupting the membrane–PrP^{Sc} interaction to facilitate fibrillization of PrP^{Sc}, resulting in denser aggregates that are easier to precipitate than their lipid-bound counterparts.

2.3.3 Decomposition of PTA at Varying pH Studied by ^{31}P NMR

To further elucidate the mechanisms of the PTA precipitation, POM speciation was determined under a range of conditions, particularly those typically used for PrP^{Sc} precipitation. Aqueous solutions of PTA at varying pH were studied by ^{31}P NMR (Figure 2.4). This technique is useful in tracking changes in the POM composition because the chemical shift of the central phosphorus atom reflects its unique chemical environment and can be used to determine which species are present. PTA samples were also prepared in complex matrices by dissolving PTA in solutions containing PBS, sarkosyl, and brain tissue at pH 7, which confirmed that PTA speciation did not change in the presence of brain homogenate compared with a water-based solution (Supplementary Figure 2S.3). Furthermore, the speciation of PTA at neutral pH in water or brain homogenate did not change over the course of eight weeks, as observed by ^{31}P NMR (Supplementary Figure 2S.4).

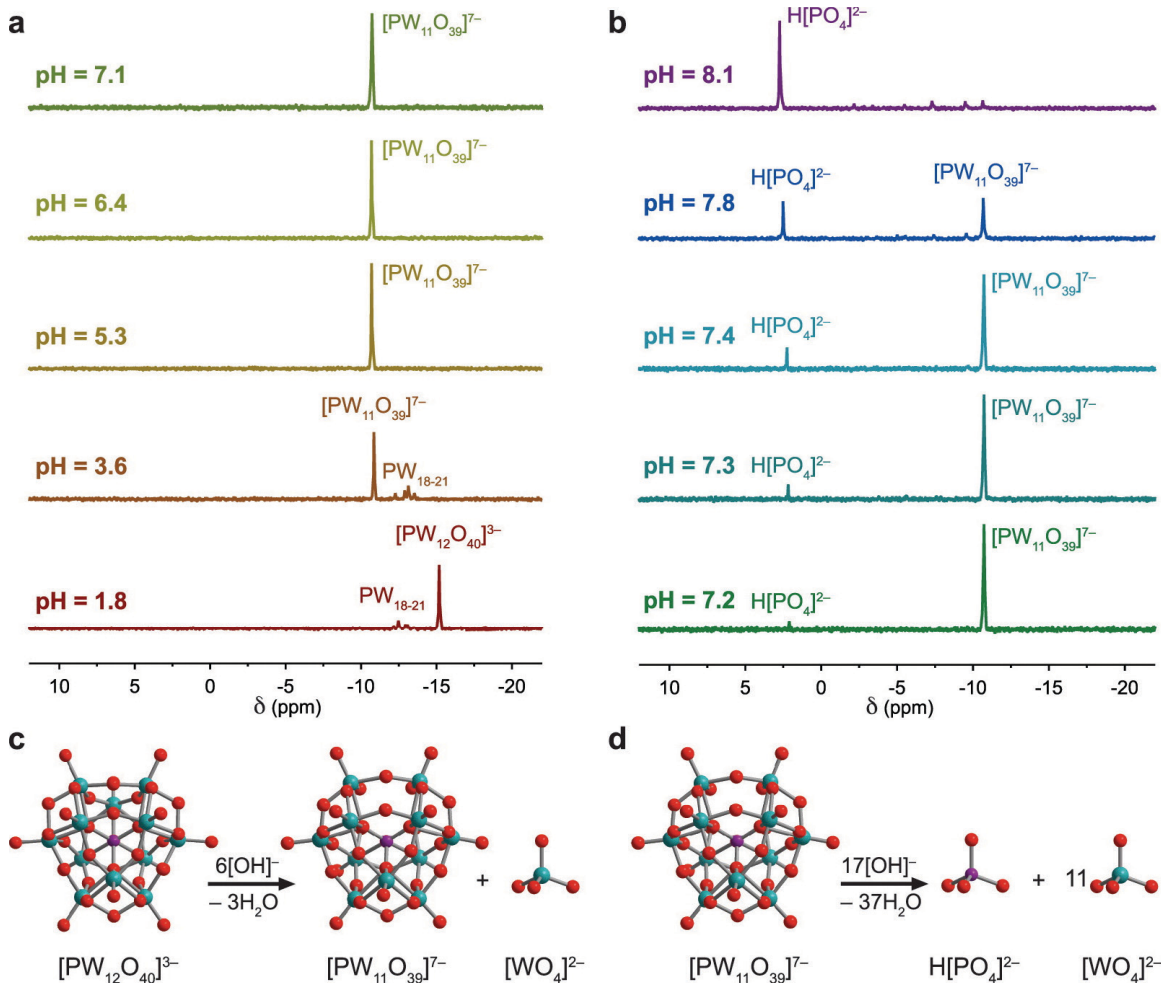

Figure 2.4. ^{31}P NMR demonstrates that PTA anion speciation changes dramatically with pH. (a, b) NMR spectra for acidic to neutral pH conditions (a) and for neutral to alkaline pH conditions (b). (c) Up to pH 7.0, the parent $[PW_{12}O_{40}]^{3-}$ ion decomposes to give a 1:1 mixture of $[PW_{11}O_{39}]^{7-}$ and $[WO_4]^{2-}$. (d) Above pH 7.1, the lacunary $[PW_{11}O_{39}]^{7-}$ ion begins to decompose into $H[PO_4]^{2-}$ and 11 $[WO_4]^{2-}$ complexes. Structural representations for $[PW_{12}O_{40}]^{3-}$, $[PW_{11}O_{39}]^{7-}$, and $[WO_4]^{2-}$ are from crystallographic information files found in refs 46-48, respectively.

PTA is synthesized by acidification of an aqueous solution containing stoichiometric amounts of tungstate and phosphate to give the product $[PW_{12}O_{40}]^{3-}$ (PW_{12}).[46] When this complex is used in biological contexts, the increase in pH from 1 to 7 leads to notable changes in the structure of the POM in solution.[49-51] By NMR spectroscopy, we confirmed that commercial $Na_3[PW_{12}O_{40}]$ (NaPTA) decomposed at neutral pH to give a lacunary $[PW_{11}O_{39}]^{7-}$ (PW_{11}) complex and a single orthotungstate $[WO_4]^{2-}$ unit (WO_4) in a 1:1 ratio (Figure 2.4a). As the pH increased above 7.1, however, we observed decomposition of PW_{11} into its original components, as evidenced by the decreasing signal at −11 ppm and the appearance of free phosphate at 2 ppm (Figure 2.4b).

Decomposition of the parent PW_{12} anion into PW_{11} and WO_4 at neutral pH is represented in Figure 2.4c, and subsequent decomposition of PW_{11} into phosphate and tungstate is shown in Figure 2.4d. The assignments of ^{31}P NMR shifts were confirmed by electrospray ionization mass spectrometry studies at varying pH (Supplementary Figure 2.S5). With different sizes and charge densities, PW_{11} and WO_4 may each have distinct interactions with PrP and have different effects on the yield and purity of PrP^{Sc} obtained from PTA precipitation.

2.3.4 Effect of PTA-Derived Anions on PrP^{Sc} Precipitation

To measure the precipitation efficacy of each PTA component under physiological conditions, increasing concentrations of PW_{11}, WO_4, and mixtures thereof were used to precipitate PrP^{Sc} from brain homogenate. Brain homogenates from RML-infected FVB mice were incubated at 37 °C for 1 h with varying concentrations of POM solutions, ranging from 0.25 to 8 mM. POM stock solutions were made fresh by dissolving the following tungstates in water and adjusting the pH to 7.1: $Na_7[PW_{11}O_{39}]$, Na_2WO_4, a 1:1 mixture of PW_{11} and WO_4, and commercial NaPTA. Following incubation with the POM solutions, the brain samples were centrifuged at 14 000*g* for 1 h.[15,19] The supernatants were discarded, and PrP levels were measured in the pellets by enzyme-linked immunosorbent assay (ELISA) (Figure 2.5) or Western immunoblotting (Figure 2.6).

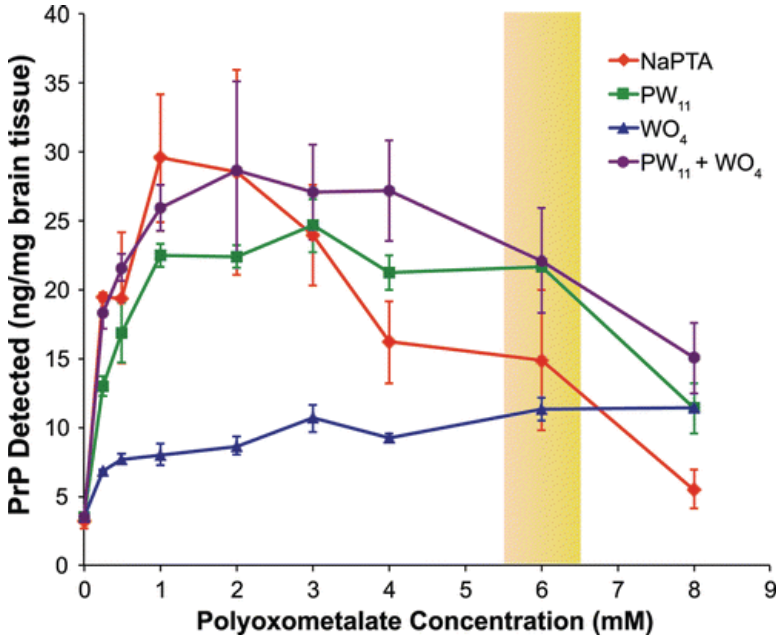

Figure 2.5. ELISA was used to quantify the amount of PrP precipitated from brain homogenates following incubation with varying concentrations of POMs. NaPTA (red), PW_{11} (green), and PW_{11} + WO_4 (purple) show a similar profile, whereas WO_4 (blue) appears to increase linearly in this concentration range. The yellow bar indicates the typical window of PTA concentrations used for PrP^{Sc}precipitations. Error bars represent the standard error of the mean across triplicate measurements of three independent sets of brain homogenate (7 brains/set).

Three independent sets of POM-precipitated samples were exposed to highly denaturing conditions (4 M guanidine hydrochloride at 100 °C) and then subjected to a sandwich ELISA (Figure 2.5). Commercial NaPTA resulted in a steep rise in the levels of detectable PrP when the concentration was increased from 0 to 1 mM and decreased gradually for the higher concentrations up to 8 mM. This trend was also observed for PW_{11} and the 1:1 mixture of $PW_{11}$and WO_4. By comparison, only a modest increase in detectable PrP was observed for equivalent WO_4 concentrations, suggesting that PW_{11} may have greater contribution in the facile detection of PrP than WO_4 by this method. The enhancement of PrP detection using POMs at different concentrations can also be expressed as a ratio of the observed values normalized to control samples where no POMs were used (Table 2.1). However, lipids have been shown to interfere with the detection of cholesterol, proteins, and other biomolecules by ELISA.[52-54] Indeed, several studies have shown that lipids can obscure the detection of PrP^{Sc} by ELISA in blood[31,55] and tissue homogenates.[56]

Table 2.1. Relative Enrichment of PrP Levels at Different Concentrations of POMs.[a]

POM concn (mM)	PTA	PW_{11}	WO_4	PW_{11} + WO_4
0	1.0 ± 0.2	1.0 ± 0.2	1.0 ± 0.2	1.0 ± 0.2
0.25	6.1 ± 0.1	4.1 ± 0.3	2.1 ± 0.1	5.8 ± 0.4
0.5	6.1 ± 1.5	5.3 ± 0.7	2.4 ± 0.2	6.8 ± 0.3
1	9.3 ± 1.5	7.1 ± 0.3	2.5 ± 0.3	8.1 ± 0.6
2	9.0 ± 2.4	7.0 ± 0.3	2.7 ± 0.2	9.0 ± 2.1
3	7.5 ± 1.2	7.7 ± 0.6	3.4 ± 0.3	8.5 ± 1.1
4	5.1 ± 1.0	6.7 ± 0.4	2.9 ± 0.1	8.5 ± 1.2
6	4.7 ± 1.6	6.8 ± 0.1	3.6 ± 0.3	6.9 ± 1.2
8	1.7 ± 0.5	3.6 ± 0.6	3.6 ± 0.1	4.7 ± 0.8

[a]*Compared to PrP levels without precipitant, as detected by ELISA*.

We performed Western immunoblotting to determine the relative level of PrP enrichment achieved by each PTA component using the D13 antibody conjugated to horseradish peroxidase (HRP);[34] GM1 levels were also probed using the HRP-coupled cholera toxin B subunit, which specifically recognizes the ganglioside GM1 (Figure 2.6). GM1 is the predominant ganglioside in neuronal membranes and is often used as marker for lipid rafts.[57,58] While other raft lipids such as cholesterol were not measured directly, the detection of GM1 with cholera toxin-based reagents is straightforward, and the presence of GM1 can be used as an indicator for the general distribution of neuronal lipids in relation to PrP.

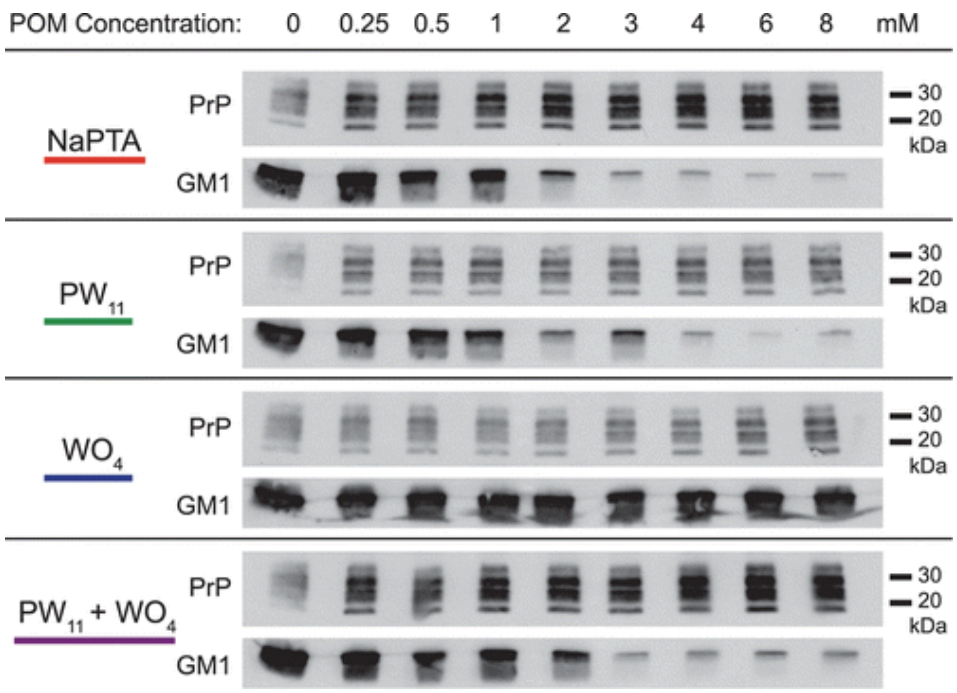

Figure 2.6. Immunoblots show the amounts of PrP and ganglioside GM1 in brain homogenates following incubation with different concentrations (0–8 mM) of POMs, as indicated. From top to bottom, POMs were sodium phosphotungstate (NaPTA), $Na_7[PW_{11}O_{39}]$ (PW_{11}), $Na_2[WO_4]$ (WO_4), and PW_{11} + WO_4. Molecular weight markers of migrated protein standards are shown in kilodaltons (kDa).

At concentrations from 0.25 to 8 mM, NaPTA and the 1:1 mixture of PW_{11} and WO_4 showed similar levels of PrP, in agreement with the decomposition of the parent PW_{12} ion into PW_{11} and WO_4 at physiological pH. Analysis of these POMs alone revealed that both PW_{11} and WO_4contributed to the precipitation efficiency of PTA solutions. However, the separation of lipids from PrP^{Sc} differed substantially for each PTA component at equimolar concentrations. PW_{11} at concentrations >1 mM resulted in a substantial decrease in GM1 levels, whereas WO_4 did not affect GM1 levels. These results suggest that while both PTA components contribute to the precipitation of PrP, PW_{11} may be more effective in disrupting the interaction between PrP and lipids such as GM1, thereby increasing the relative purity of the precipitates.

Comparing the results from the ELISAs and Western blots, the discrepancy in the levels of PrP measured by these two methods at very low concentrations of POM likely results from the presence of GM1, and perhaps other lipids, associated with PrP. In cases where sensitivity of PrP^{Sc} detection is crucial, it is therefore important to use high enough concentrations of PTA (or PW_{11} in particular) to reduce the amount of coprecipitating lipids and facilitate detection of PrP^{Sc} in blood and tissue samples for diagnostic purposes.

2.4 Conclusions

Using spectrochemical, biophysical, and microscopic techniques, we observed that the effective precipitation of PrP^{Sc} by PTA may occur by some combination of facilitated fibril formation, enhanced separation of lipids from PrP^{Sc}, and increased density of PrP^{Sc} aggregates. The increase in the amount of large aggregates obtained when PTA and sarkosyl were used together suggests that the separation of lipids such as GM1 from PrP^{Sc} is a major factor that can influence prion precipitation (Figures 2.2 and 2.3). It is possible that the observed fibrillization is a direct consequence of lipid removal by PTA and sarkosyl, since PrP^{Sc} detached from membranes has been found to readily form amyloid.[44] Additionally, ganglioside GM1, which is the most abundant neuronal ganglioside,[40] was also studied as a marker of total lipid content and an indicator of sample purity. We found decreased levels of GM1 with higher concentrations of NaPTA, PW_{11} + WO_4, and PW_{11} while WO_4 was not as effective at equimolar concentrations (Figure 2.6).

From sucrose cushion centrifugations, incubation with PTA increased the density of PrP aggregates (Figure 2.3). PrP^{Sc} alone has a density of approximately 1.35 g/mL, while an 80% sucrose solution has a density of ~1.41 g/mL.[59] The PrP aggregates that permeated the 80% sucrose cushion and formed the pellet must have a density in excess of 1.41 g/mL. Unlike most proteins, PrP has a high isoelectric point of approximately 9 for the full-length protein,[60] rendering the protein positively charged at neutral pH. This feature of PrP may be used advantageously because manipulation of electrostatic interactions can be achieved using anionic compounds such as PTA and detergents. Our work on the pH-dependent decomposition of polyoxometalates (Figure 2.4) suggests that PrP^{Sc} precipitations using PTA should be carried out on the lower end of the physiological pH range, closer to pH 7.1 rather than 7.4, in order to maintain the integrity of the PW_{11} ion, particularly when greater sample purity is desired.

While both PW_{11} and WO_4 components of PTA contributed to the yield of PrP during precipitation, PW_{11} is primarily responsible for a reduction in coprecipitating GM1 lipids, as evidenced by the levels of ganglioside GM1 by Western blot (Figure 2.6). PW_{11} at concentrations >1 mM substantially reduced the level of coprecipitating lipids, while WO_4 did not at equivalent concentrations. This lipid reduction might explain why precipitation with PW_{11} facilitated detection of PrP by ELISA more effectively than the WO_4 component at concentrations between 0.25 and 6 mM (Figure 2.5). The lipids remaining in the WO_4-incubated samples may mask epitopes on PrP and hinder its binding to the detection antibodies in ELISA. The difference in lipid levels following PW_{11} and WO_4 precipitations may be attributed to the size and charge differences between the two tungstates, because the WO_4 ion has a single heavy tungsten atom and a delocalized −2 charge while PW_{11} is a much larger, heavier anion with a −7 charge. These differences between PW_{11} and WO_4 as well as our experiments with NaCl indicate that electrostatic interactions may be involved in promoting PrP^{Sc} precipitation by their disruption of interactions between PrP^{Sc} and buoyant anionic lipids like GM1. Direct association of dense tungstates with positively charged PrP^{Sc} may also contribute to the precipitation efficiency.

Reducing the amount of coprecipitating lipids such as GM1 may have implications for various areas of prion research, including biophysical studies of protein structure and diagnostic assay development. Lipids have been shown to interfere with protein detection assays, particularly those relying on the specificity of a protein–antibody interaction.[31,55] By reducing the lipid content of biological samples with typically low prion titers, high-throughput detection assays for cattle and human blood may be developed to reduce the risk of contracting variant Creutzfeldt–Jakob disease from meat products or blood transfusions.

By elucidating the mechanisms of PTA precipitation of PrP^{Sc}, we can improve our methods for sample preparation, which may play a crucial role in studies to probe the structure of PrP^{Sc} and to develop robust diagnostic tools. The principles governing the precipitation of PrP^{Sc} may also prove useful in studying other protein-misfolding diseases, in which the hydrophobic nature of protein aggregates promotes undesired binding of lipids to the aggregates.

2.5 Acknowledgements

This work was performed in collaboration with several scientists at the Institute for Neurodegenerative Diseases at the University of California, San Francisco. Lillian E. Falese performed the sucrose cushion experiments, and Professor Holger Wille performed the electron microscopy experiments. Professors Jan Stöhr, Holger Wille, and Stanley B. Prusiner served as advisors on this project and contributed to the writing of the resulting manuscript in conjuction with Professor Jeffrey Long at Berkeley.

We thank the staff at the Hunter's Point Animal Facility for their assistance in providing tissue samples and A.T. Iavarone for assistance with mass spectrometry measurements. We also thank H. Nguyen for her editorial expertise. This work was sponsored by grants from the NIH (AG002132, AG021601, and AG010770) as well as by a gift from the Sherman Fairchild Foundation. D.J.L. was supported by the Department of Defense (DoD) through the National Defense Science & Engineering Graduate Fellowship (NDSEG) Program and the National Science Foundation Graduate Research Fellowship Program (NSF GRFP). We also thank the UC Berkeley NMR Facility (NIH Grant SRR023679A) and QB3/Chemistry Mass Spectrometry Facility for access to instrumentation.

Portions of this work appear in the following publication:
Mechanism of Scrapie Prion Precipitation with Phosphotungstate Anions. Dana J. Levine, Jan Stöhr, Lillian E. Falese, Julian Ollesch, Holger Wille, Stanley B. Prusiner, and Jeffrey R. Long**,** *ACS Chem. Biol.,* **2015** *10* (5), 1269-1277.

2.6 References

(1) Colby, D. W., and Prusiner, S. B. (2011) Prions. *Cold Spring Harbor Perspect. Biol.* 3a006833.
(2) Prusiner, S. B. (2007) Prions, in *Fields Virology* (Knipe, D. M., Howley, P. M., Griffin, D. E., Lamb, R. A., Martin, A, M., Roizman, B., and Straus, S. E., Eds.) 5 ed., pp 3059–3092. Philadelphia.
(3) Prusiner, S. B. (2012) A unifying role for prions in neurodegenerative diseases. *Science 336*, 1511–1513.
(4) Pan, K. M., Baldwin, M., Nguyen, J., Gasset, M., Serban, A., Groth, D., Mehlhorn, I., Huang, Z., Fletterick, R. J., and Cohen, F. E. (1993) Conversion of alpha-helices into beta-sheets features in the formation of the scrapie prion proteins. *Proc. Natl. Acad. Sci. 90*, 10962–10966.
(5) Collinge, J., and Palmer, S. (1992) Molecular genetics of inherited, sporadic and iatrogenic prion disease. *In: Prusiner, SB and Collinge, J and Powell, J and Anderton, B, (eds.) Prion diseases of humans and animals. (95 - 119). Ellis Horwood: London, UK.*
(6) Meyer-Luehmann, M., Coomaraswamy, J., Bolmont, T., Kaeser, S., Schaefer, C., Kilger, E., Neuenschwander, A., Abramowski, D., Frey, P., Jaton, A. L., Vigouret, J.-M., Paganetti, P., Walsh, D. M., Mathews, P. M., Ghiso, J., Staufenbiel, M., Walker, L. C., and Jucker, M. (2006) Exogenous induction of cerebral beta-amyloidogenesis is governed by agent and host. *Science 313*, 1781–1784.
(7) Stöhr, J., Watts, J. C., Mensinger, Z. L., Oehler, A., Grillo, S. K., DeArmond, S. J., Prusiner, S. B., and Giles, K. (2012) Purified and synthetic Alzheimer's amyloid beta (Aβ) prions. *Proc. Natl. Acad. Sci. U.S.A. 109*, 11025–11030.
(8) Luk, K. C., Kehm, V. M., Zhang, B., O'Brien, P., Trojanowski, J. Q., and Lee, V. M. Y. (2012) Intracerebral inoculation of pathological α-synuclein initiates a rapidly progressive neurodegenerative α-synucleinopathy in mice. *J. Exp. Med. 209*, 975–986.
(9) Watts, J. C., Giles, K., Oehler, A., Middleton, L., Dexter, D. T., Gentleman, S. M., DeArmond, S. J., and Prusiner, S. B. (2013) Transmission of multiple system atrophy prions to transgenic mice. *Proc. Natl. Acad. Sci. U.S.A. 110*, 19555–19560.
(10) Clavaguera, F., Akatsu, H., Fraser, G., Crowther, R. A., Frank, S., Hench, J., Probst, A., Winkler, D. T., Reichwald, J., Staufenbiel, M., Ghetti, B., Goedert, M., and Tolnay, M. (2013) Brain homogenates from human tauopathies induce tau inclusions in mouse brain. *Proc. Natl. Acad. Sci. U.S.A. 110*, 9535–9540.
(11) Sanders, D. W., Kaufman, S. K., DeVos, S. L., Sharma, A. M., Mirbaha, H., Li, A., Barker, S. J., Foley, A. C., Thorpe, J. R., Serpell, L. C., Miller, T. M., Grinberg, L. T., Seeley, W. W., and Diamond, M. I. (2014) Distinct tau prion strains propagate in cells and mice and define different tauopathies. *Neuron 82*, 1271–1288.
(12) Wille, H., Bian, W., McDonald, M., Kendall, A., Colby, D. W., Bloch, L., Ollesch, J., Borovinskiy, A. L., Cohen, F. E., Prusiner, S. B., and Stubbs, G. (2009) Natural and synthetic prion structure from X-ray fiber diffraction. *Proc. Natl. Acad. Sci. U.S.A. 106*, 16990–16995.
(13) Govaerts, C., Wille, H., Prusiner, S. B., and Cohen, F. E. (2004) Evidence for assembly of prions with left-handed beta-helices into trimers. *Proc. Natl. Acad. Sci. 101*, 8342–8347.
(14) Smirnovas, V., Baron, G. S., Offerdahl, D. K., Raymond, G. J., Caughey, B., and

Surewicz, W. K. (2011) Structural organization of brain-derived mammalian prions examined by hydrogen-deuterium exchange. *Nat. Struct. Mol. Biol. 18*, 504–506.
(15) Wille, H., Shanmugam, M., Murugesu, M., Ollesch, J., Stubbs, G., Long, J. R., Safar, J. G., and Prusiner, S. B. (2009) Surface charge of polyoxometalates modulates polymerization of the scrapie prion protein. *Proc. Natl. Acad. Sci. U.S.A. 106*, 3740–3745.
(16) Prusiner, S. B., McKinley, M. P., Bowman, K. A., Bolton, D. C., Bendheim, P. E., Groth, D. F., and Glenner, G. G. (1983) Scrapie prions aggregate to form amyloid-like birefringent rods. *Cell 35*, 349–358.
(17) McKinley, M. P., Bolton, D. C., and Prusiner, S. B. (1983) Fibril-like structures in preparations of scrapie prions purified from hamster brain. *Proc. - Electron Microsc. Soc. Am.* 802–803.
(18) Sim, V. L., and Caughey, B. (2009) Ultrastructures and strain comparison of under-glycosylated scrapie prion fibrils. *Neurobiol. Aging 30*, 2031–2042.
(19) Safar, J., Wille, H., Itri, V., Groth, D., Serban, H., Torchia, M., Cohen, F. E., and Prusiner, S. B. (1998) Eight prion strains have PrP^{Sc} molecules with different conformations. *Nat. Med. 4*, 1157–1165.
(20) White, A. R., Enever, P., Tayebi, M., Mushens, R., Linehan, J., Brandner, S., Anstee, D., Collinge, J., and Hawke, S. (2003) Monoclonal antibodies inhibit prion replication and delay the development of prion disease. *Nature 422*, 80–83.
(21) Hill, A. F., Butterworth, R. J., Joiner, S., Jackson, G., Rossor, M. N., Thomas, D. J., Frosh, A., Tolley, N., Bell, J. E., Spencer, M., King, A., Al-Sarraj, S., Ironside, J. W., Lantos, P. L., and Collinge, J. (1999) Investigation of variant Creutzfeldt-Jakob disease and other human prion diseases with tonsil biopsy samples. *Lancet 353*, 183–189.
(22) Glatzel, M., Abela, E., Maissen, M., and Aguzzi, A. (2003) Extraneural pathologic prion protein in sporadic Creutzfeldt-Jakob disease. *N. Engl. J. Med. 349*, 1812–1820.
(23) Wroe, S. J., Pal, S., Siddique, D., Hyare, H., Macfarlane, R., Joiner, S., Linehan, J. M., Brandner, S., Wadsworth, J. D. F., Hewitt, P., and Collinge, J. (2006) Clinical presentation and pre-mortem diagnosis of variant Creutzfeldt-Jakob disease associated with blood transfusion: a case report. *Lancet 368*, 2061–2067.
(24) Saa, P., Castilla, J., and Soto, C. (2006) Ultra-efficient replication of infectious prions by automated protein misfolding cyclic amplification. *J. Biol. Chem. 281*, 35245–35252.
(25) Huang, H. S., Rendulich, J., Stevenson, D., O'Rourke, K., and Balachandran, A. (2005) Evaluation of Western blotting methods using samples with or without sodium phosphotungstic acid precipitation for diagnosis of scrapie and chronic wasting disease. *Can. J. Vet. Res. 69*, 193–199.
(26) Lee, I. S., Long, J. R., Prusiner, S. B., and Safar, J. G. (2005) Selective precipitation of prions by polyoxometalate complexes. *J. Am. Chem. Soc. 127*, 13802–13803.
(27) Colby, D. W., Zhang, Q., Wang, S., Groth, D., Legname, G., Riesner, D., and Prusiner, S. B. (2007) Prion detection by an amyloid seeding assay. *Proc. Natl. Acad. Sci. 104*, 20914–20919.
(28) Bennion, B. J., and Daggett, V. (2002) Protein conformation and diagnostic tests: The prion protein. *Clin. Chem. 48*, 2105–2114.
(29) Birkmann, E., Henke, F., Funke, S. A., Bannach, O., Riesner, D., and Willbold, D. (2008) A highly sensitive diagnostic assay for aggregate-related diseases, including prion

diseases and Alzheimer's disease. *Rejuvenation Res. 11*, 359–363.
(30) Wadsworth, J., Joiner, S., Hill, A. F., Campbell, T. A., Desbruslais, M., Luthert, P. J., and Collinge, J. (2001) Tissue distribution of protease resistant prion protein in variant Creutzfeldt-Jakob disease using a highly sensitive immunoblotting assay. *Lancet 358*, 171–180.
(31) Bannach, O., Birkmann, E., Reinartz, E., Jaeger, K.-E., Langeveld, J. P. M., Rohwer, R. G., Gregori, L., Terry, L. A., Willbold, D., and Riesner, D. (2012) Detection of prion protein particles in blood plasma of scrapie infected sheep. *PLoS ONE, 7*, e36620.
(32) Bocharova, O. V., Breydo, L., Parfenov, A. S., Salnikov, V. V., and Baskakov, I. V. (2005) In vitro conversion of full-length mammalian prion protein produces amyloid form with physical properties of PrP^{Sc}. *J. Mol. Biol. 346*, 645–659.
(33) Safar, J. G., Scott, M., Monaghan, J., Deering, C., Didorenko, S., Vergara, J., Ball, H., Legname, G., Leclerc, E., Solforosi, L., Serban, H., Groth, D., Burton, D. R., Prusiner, S. B., and Williamson, R. A. (2002) Measuring prions causing bovine spongiform encephalopathy or chronic wasting disease by immunoassays and transgenic mice. *Nat. Biotechnol. 20*, 1147–1150.
(34) Williamson, R. A., Peretz, D., Pinilla, C., Ball, H., Bastidas, R. B., Rozenshteyn, R., Houghten, R. A., Prusiner, S. B., and Burton, D. R. (1998) Mapping the prion protein using recombinant antibodies. *J. Virol. 72*, 9413–9418.
(35) Wille, H., and Prusiner, S. B. (1999) Ultrastructural studies on scrapie prion protein crystals obtained from reverse micellar solutions. *Biophys. J. 76*, 1048–1062.
(36) Brevard, C., Schimpf, R., and Tourne, G. (1983) Tungsten-183 NMR: A complete and unequivocal assignment of the tungsten-tungsten connectivities in heteropolytungstates via two-dimensional tungsten-183 NMR techniques. *J. Am. Chem. Soc. 105*, 7059–7063.
(37) Leading Technology Group Pty Ltd. ElisaAnalysis. Elisakit.com, Victoria, Australia.
(38) Godsave, S. F., Wille, H., Pierson, J., Prusiner, S. B., and Peters, P. J. (2013) Plasma membrane invaginations containing clusters of full-length PrP^{Sc} are an early form of prion-associated neuropathology in vivo. *Neurobiol. Aging 34*, 1621–1631.
(39) Sanghera, N., Correia, B. E. F. S., Correia, J. R. S., Ludwig, C., Agarwal, S., Nakamura, H. K., Kuwata, K., Samain, E., Gill, A. C., Bonev, B. B., and Pinheiro, T. J. T. (2011) Deciphering the molecular details for the binding of the prion protein to main ganglioside GM1 of neuronal membranes. *Chem. Biol. 18*, 1422–1431.
(40) Pang, H., Le, P. U., and Nabi, I. R. (2004) Ganglioside GM1 levels are a determinant of the extent of caveolae/raft-dependent endocytosis of cholera toxin to the Golgi apparatus. *J. Cell. Sci. 117*, 1421–1430.
(41) Vey, M., Pilkuhn, S., Wille, H., Nixon, R., Dearmond, S. J., Smart, E. J., Anderson, R., Taraboulos, A., and Prusiner, S. B. (1996) Subcellular colocalization of the cellular and scrapie prion proteins in caveolae-like membranous domains. *Proc. Natl. Acad. Sci. 93*, 14945–14949.
(42) Stahl, N., Baldwin, M. A., Burlingame, A. L., and Prusiner, S. B. (1990) Identification of glycoinositol phospholipid linked and truncated forms of the scrapie prion protein. *Biochemistry 29*, 8879–8884.
(43) Elfrink, K., Ollesch, J., Stöhr, J., Willbold, D., Riesner, D., and Gerwert, K. (2008) Structural changes of membrane-anchored native PrP^{C}. *Proc. Natl. Acad. Sci. 105*, 10815–10819.

(44) Chesebro, B., Trifilo, M., Race, R., Meade-White, K., Teng, C., LaCasse, R., Raymond, L., Favara, C., Baron, G., Priola, S., Caughey, B., Masliah, E., and Oldstone, M. (2005) Anchorless prion protein results in infectious amyloid disease without clinical scrapie. *Science 308*, 1435–1439.
(45) Stöhr, J., Watts, J. C., Legname, G., Oehler, A., Lemus, A., Nguyen, H.-O. B., Sussman, J., Wille, H., DeArmond, S. J., Prusiner, S. B., and Giles, K. (2011) Spontaneous generation of anchorless prions in transgenic mice. *Proc. Natl. Acad. Sci. U.S.A. 108*, 21223–21228.
(46) Keggin, J. F. (1933) Structure of the molecule of 12-phosphotungstic acid. *Nature 131*, 908–909.
(47) Fuchs, J., Thiele, A., and Palm, R. (1981) Struktur und Schwingungsspektrum des *α*-Undekawolframatophosphats $Na_2[N(CH_3)_4]\ {}_4HPW_{11}O_{39}\cdot 7H_2O$. *Z. Naturforsch. B 36*, 544–550.
(48) Okada, K., Morikawa, H., Marumo, F., and Iwai, S. (1974) Sodium tungstate. *Acta Cryst. B 30*, 1872–1873.
(49) Kyle, J. H. (1983) Kinetics of the base decomposition of dodecatungstophosphate(3–) in weakly alkaline solutions. *J. Chem. Soc., Dalton Trans.* 2609.
(50) Zhu, Z., Tain, R., and Rhodes, C. (2003) A study of the decomposition behaviour of 12-tungstophosphate heteropolyacid in solution. *Can. J. Chem. 81*, 1044–1050.
(51) Smith, B. J., and Patrick, V. A. (2004) Quantitative determination of aqueous dodecatungstophosphoric acid speciation by NMR spectroscopy. *Aust. J. Chem. 57*, 261–268.
(52) Ji, J. Z., and Meng, Q. H. (2011) Evaluation of the interference of hemoglobin, bilirubin, and lipids on Roche Cobas 6000 assays. *Clin. Chim. Acta 412*, 1550–1553.
(53) Steen, G., Klerk, A., van der Laan, K., and Eppens, E. F. (2011) Evaluation of the interference due to haemoglobin, bilirubin and lipids on Immulite 2500 assays: a practical approach. *Ann. Clin. Biochem. 48*, 170–175.
(54) Dimeski, G. (2008) Interference testing. *Clin. Biochem. Rev. 29 Suppl 1*, S43–8.
(55) Edgeworth, J. A., Farmer, M., Sicilia, A., Tavares, P., Beck, J., Campbell, T., Lowe, J., Mead, S., Rudge, P., Collinge, J., and Jackson, G. S. (2011) Detection of prion infection in variant Creutzfeldt-Jakob disease: a blood-based assay. *Lancet 377*, 487–493.
(56) Hervé, R., Collin, R., Pinchin, H. E., Secker, T., and Keevil, C. W. (2009) A rapid dual staining procedure for the quantitative discrimination of prion amyloid from tissues reveals how interactions between amyloid and lipids in tissue homogenates may hinder the detection of prions. *J. Microbiol. Methods 77*, 90–97.
(57) Blank, N., Gabler, C., Schiller, M., Kriegel, M., Kalden, J. R., and Lorenz, H. M. (2002) A fast, simple and sensitive method for the detection and quantification of detergent-resistant membranes. *J. Immunol. Methods 271*, 25–35.
(58) Botto, L., Cunati, D., Coco, S., Sesana, S., Bulbarelli, A., Biasini, E., Colombo, L., Negro, A., Chiesa, R., Masserini, M., and Palestini, P. (2014) Role of lipid rafts and GM1 in the segregation and processing of prion protein. *PLoS ONE, 9*, e98344.
(59) Reiser, P., Birch, G. G., and Mathlouthi, M. (1994) Physical Properties, in *Sucrose Properties and Applications* (Mathlouthi, M., and Reiser, P., Eds.), pp 186–222. Glasgow.
(60) Morillas, M., Swietnicki, W., Gambetti, P., and Surewicz, W. K. (1999) Membrane environment alters the conformational structure of the recombinant human prion protein. *J. Biol. Chem. 274*, 36859–36865.

2.7 Supplementary Information

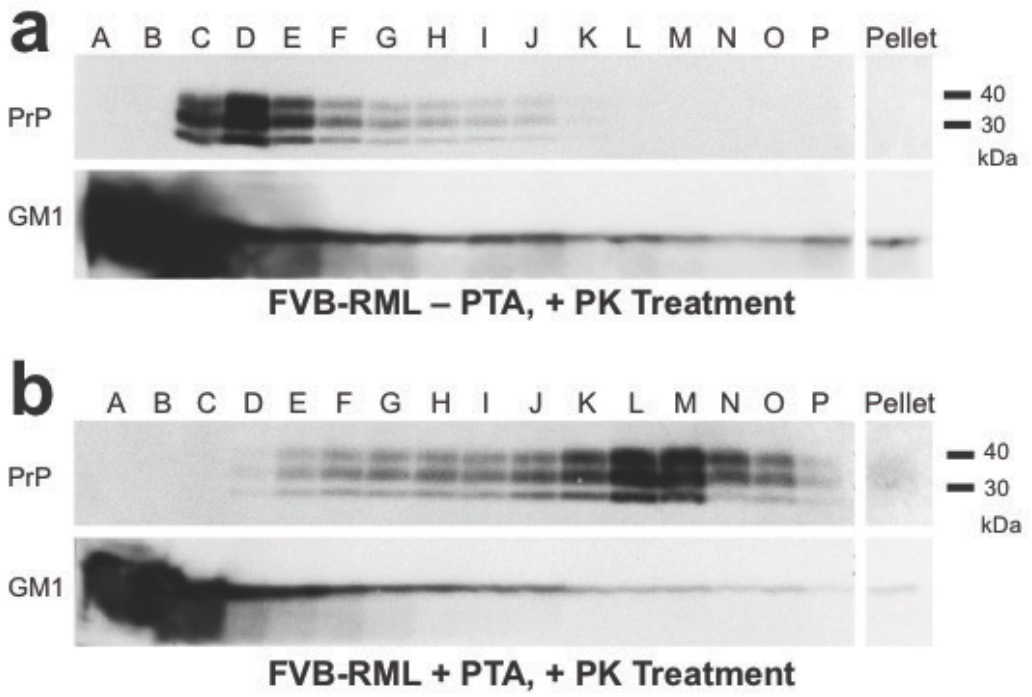

Figure 2.S1. Sucrose cushion centrifugations were performed on prion-infected brain homogenate digested with proteinase K (PK); the samples were incubated without PTA (a) or with PTA (b). The procedure is analogous to that described in the *Methods* with the addition of a PK digestion and subsequent inhibition step prior to incubation without or with PTA. In brief, a 3-mL aliquot of FVB-RML brain homogenate (20% w/v with 2% sarkosyl) was treated with 30 µL of PK solution (2 mg/mL) and incubated for 1 h at 37 °C with shaking. The digestion was then stopped by addition of 31 µL of protease inhibitor solution (0.1 M phenylmethylsulfonyl fluoride) and incubation at 37 °C for 1 h with shaking. Then, two 1.2-mL aliquots were treated with either 300 µL of PBS solution (control) or 10% (w/v) PTA solution and incubated at 37 °C for 24 h with shaking before being loaded onto a three-step sucrose cushion as described in the *Methods* section. Western blot lanes are labeled according to fractions of increasing density as in Figure 2.4a; however, the PK digestion step increases the sample volume, thereby creating an additional fraction. PK degrades PrP^{C} and proteolytically cleaves the N-terminus of PrP^{Sc} to give PrP 27-30. (a) Without PTA, essentially no PrP 27-30 was found in the pellet, with the majority of the protein remaining in the 50% sucrose region, along with most of the GM1 lipids, which were found primarily in the low-density fractions A–E. (b) Addition of PTA resulted in PrP 27-30 moving to higher density fractions in the 80% sucrose regime (lanes K–M), while GM1 remained in the lowest density fractions (primarily A–C). This change in the distribution of GM1 and PrP 27-30 upon addition of PTA is indicative of a disruption in PrP–lipid interactions, which facilitates precipitation of both full-length PrP^{Sc} and truncated PrP 27-30. Molecular weight markers of migrated protein standards are shown in kilodaltons (kDa).

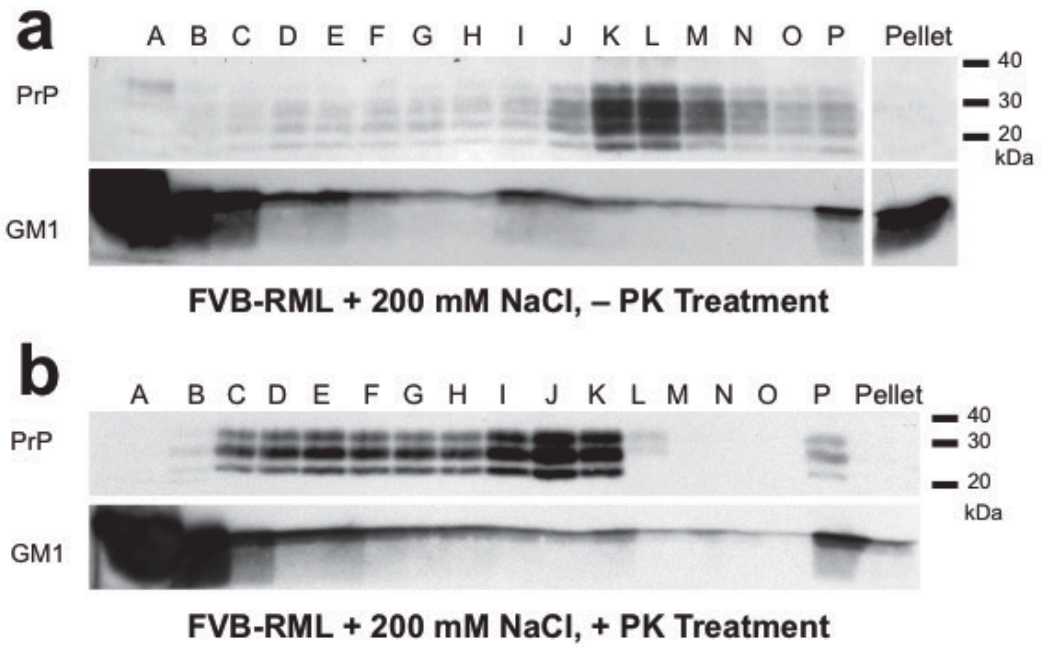

Figure 2.S2. Sucrose cushion centrifugations were performed on prion-infected brain homogenate samples treated with concentrated NaCl; the samples contained either undigested PrP^{Sc} (a) or PK-digested PrP 27-30 (b). Samples were prepared as described in the *Methods* for sucrose cushion centrifugation experiments. In brief, 4 mL of FVB-RML brain homogenate (20% w/v with 2% sarkosyl) were treated with 1 mL of 1 M NaCl (final concentration: 200 mM NaCl). This sample was split into two equal aliquots; one was left undigested and the other was digested with PK as described for Figure 2.S1. These samples were incubated at 37 °C for 24 h with shaking before being loaded onto a three-step sucrose cushion. (a) Undigested samples treated with NaCl resulted in more PrP^{Sc} penetrating the 80% sucrose layer (lanes L–P). However, 200 mM NaCl did not result in substantial precipitation of PrP^{Sc}, suggesting that a high ionic strength alone is not sufficient for PrP^{Sc} precipitation and that the efficacy of PTA is likely due to other factors, such as the density, charge, and structure of the complex. (b) With PK digestion and NaCl treatment, the majority of PrP 27-30 remained in the low-density sucrose layers, above the 50–80% sucrose interface (lanes I–K), while the GM1 also remained in the lowest-density fractions (primarily A and B). Some GM1 was found to colocalize with a dense subset of PrP 27-30 in fraction P, suggesting that NaCl is not particularly effective at removing lipids from PrP 27-30 as compared to PTA. Molecular weight markers of migrated protein standards are shown in kilodaltons (kDa).

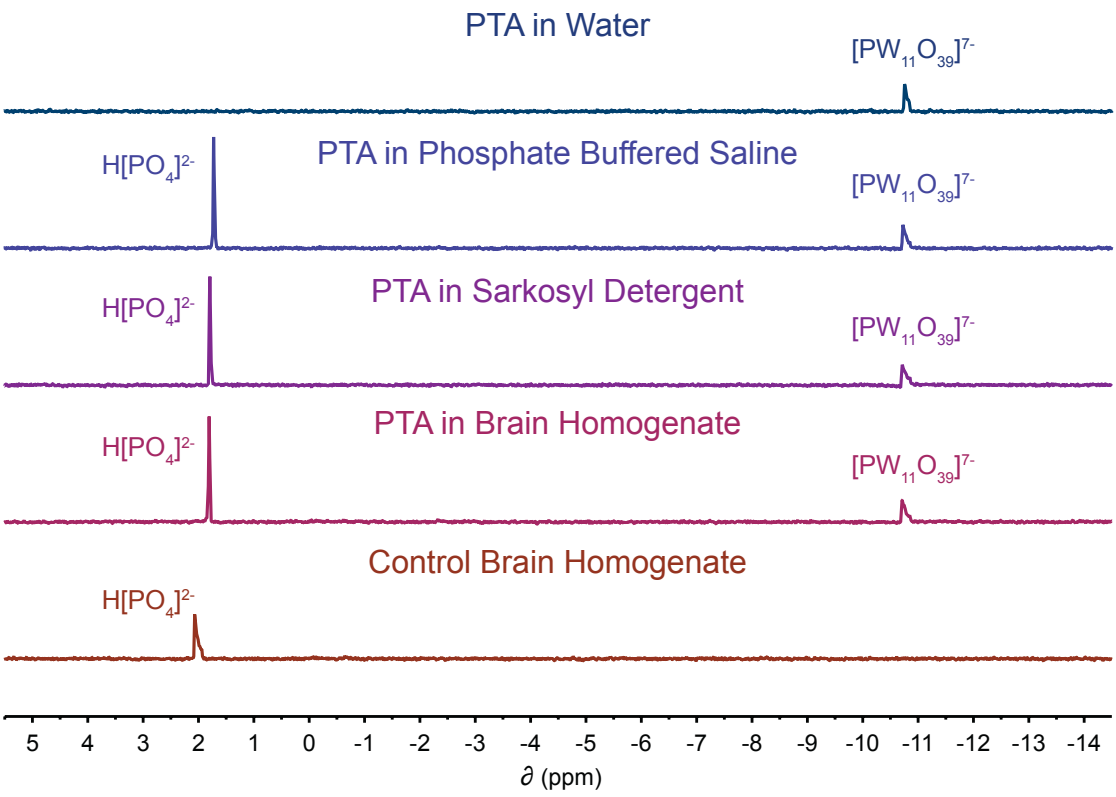

Figure 2.S3. ^{31}P NMR spectra of PTA were collected in increasingly complex aqueous environments. Samples contained 2% PTA (w/v) and 90:10 H_2O:D_2O. The $[PW_{11}O_{39}]^{7-}$ species observed at neutral pH remains unchanged when placed in water, water with PBS, water with PBS and sarkosyl (2% w/v), and brain homogenate prepared with PBS and sarkosyl. Control brain homogenate without PTA confirms the signal corresponding to free phosphate in solution. All NMR spectra were acquired on a Bruker Avance III NMR spectrometer equipped with a BBO broadband probe operating at 600.13 MHz for ^{1}H, and 242.93 MHz for ^{31}P.

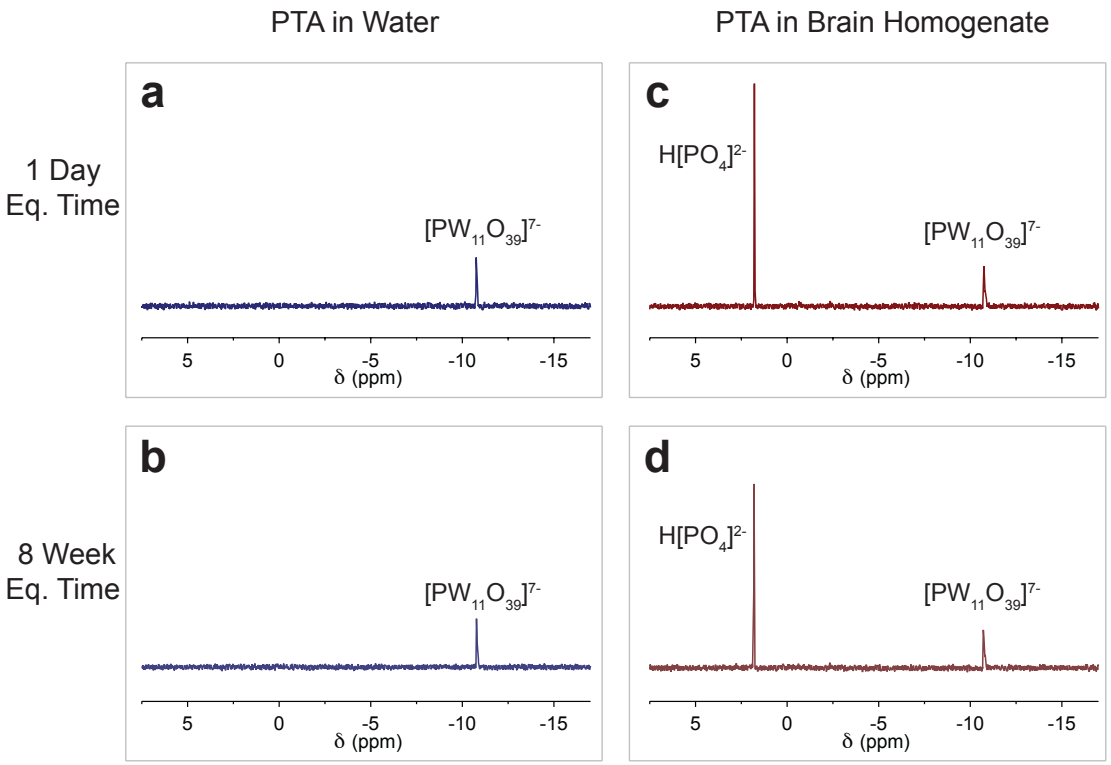

Figure 2.S4. ^{31}P NMR spectra of PTA solutions were collected after short and long equilibration times. The PTA speciation remains unchanged in both water and brain homogenate at pH 7 over an 8-week period as observed by ^{31}P NMR (2% PTA (w/v) in 90:10 H_2O:D_2O).

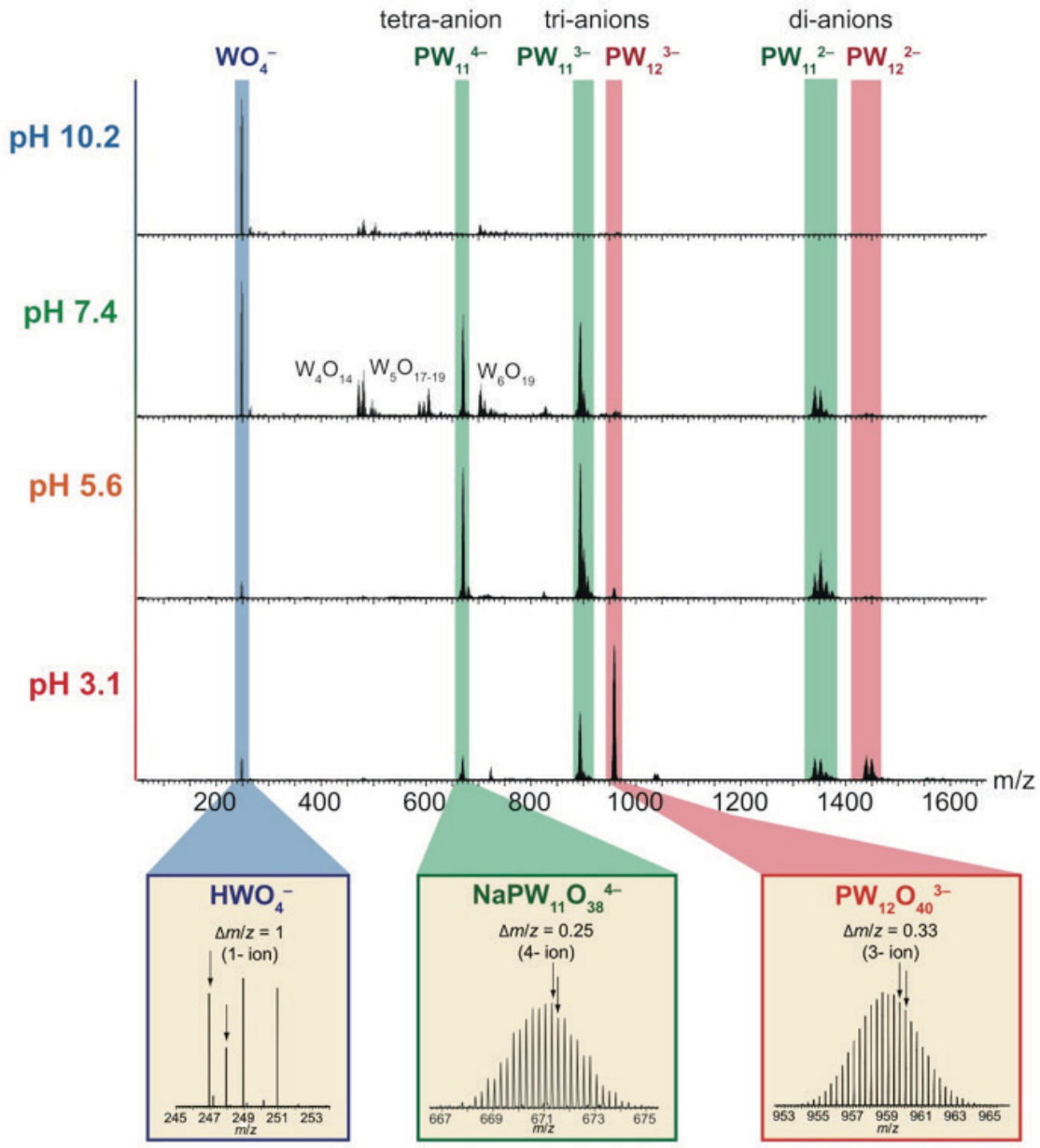

Figure 2.S5. Electrospray ionization mass spectrometry (ESI-MS) in the negative ion mode was used to confirm the identities of PTA species observed at varying pH (y axis). All peaks were identified using the m/z and Δm/z values and matching the experimental patterns to theoretical isotope distributions. Charge states corresponding to $[PW_{12}O_{40}]^{3-}$ (PW_{12}) are highlighted in red, $[PW_{11}O_{39}]^{7-}$ (PW_{11}) in green, and $[WO_4]^{2-}$ (WO_4) in blue. Examples of experimental isotopic distributions are shown in the panels for the mono-anion of WO_4, the tetra-anion of PW_{11}, and the tri-anion of PW_{12}. Mass spectra were acquired on a quadrupole time-of-flight mass spectrometer (Q-Tof Premier, Waters, Milford, MA) equipped with an ESI source.

Chapter 3: pH-Triggered Release of Olsalazine from Calcium-Based Coordination Solids for Treatment of Ulcerative Colitis

3.1 Introduction

Medicinal chemistry has yielded an impressive array of small-molecule therapeutics for the treatment of disease. However, the application of many drug candidates is hindered by the prevalence of side effects, especially if the drug has a narrow therapeutic index. Controlled release is a powerful strategy that serves to improve the therapeutic efficacy of a drug while minimizing side effects in patients. Liposomes, micelles, polymer nano/microspheres, dendrimers, mesoporous silica, and other carriers have been established as useful vehicles for the delivery of therapeutic agents, and many such systems have already obtained FDA approval.

An alternative approach is to mask the therapeutic as a prodrug that is converted to the active compound *in vivo*. The administration of biologically active compounds as prodrugs can greatly enhance their performance by increasing their circulation time, absorption, and potency while protecting the active form of the molecules from degradation. In addition, they can be designed to release their payload in response to stimuli such as changes in pH or redox environment. Metal-based coordination solids provide an especially attractive approach to prodrug design due to their inherent modularity and chemical diversity. In addition to conventional approaches to prodrug design, coordination solids present other features, such as particle size and choice of metal that can be tuned to achieve the desired pharmacokinetic properties.

Metals can be used to form various classes of compounds with drug molecules. In principle, any drug with a Lewis-basic functional group (e.g., $–O^–$, $–S^–$, $–NH_2$) can serve as a ligand to form complexes with biocompatible metals such as Na^+, K^+, Mg^{2+}, and Ca^{2+}. While simple salts are commonly used in drug formulation, drugs with two or more coordinating groups arranged appropriately can also allow the formation of extended networks, which can range in dimensionality from one-dimensional chains to three-dimensional structures (Figure 3.1). The nature of the resulting phase can also be influenced by the synthetic conditions used to make the materials. Such factors as solvent, temperature, metal source, stoichiometry, and reagent concentrations can be tuned to better control the reaction outcome, thereby allowing different materials to be obtained from the same metal and ligand combination. These materials can be amorphous or crystalline, forming coordination polymers or coordination solids, respectively. The three-dimensional structures can be dense or porous after removal of guest solvents, the latter of which are a class of materials known as metal-organic frameworks (MOFs). MOFs as encapsulants of drugs will be discussed in greater detail in the subsequent chapter.

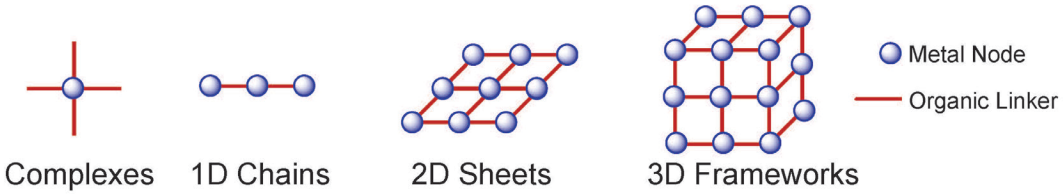

Figure 3.1. Schematic showing the varying dimensionality of extended solids. From left to right, metal nodes and organic linkers can be combined to form complexes, one-dimensional chains, two-dimensional sheets, or three-dimensional frameworks.

There are several examples of metal-organic frameworks that have been made with bioactive molecule as the linker. These include systems with iron and nicotinic acid,[1] zinc and the iron chelator deferiprone,[2] magnesium and the antioxidant gallate,[3] and zinc and curcumin.[4] Coordination solids have also been prepared similarly with thiopurine antimetabolites[5-7] and the chemotherapeutic letrozole.[8-10] Additionally, the company Synthonics is focused on developing several metal-coordinated pharmaceuticals, including a bismuth-based coordination polymer of L-DOPA for treatment of Parkinson's disease.[11]

Olsalazine is an interesting candidate for preparation as a coordination solid, since this medication has side effects and is also a high symmetry ligand. Olsalazine is a prodrug of 5-aminosalicylic acid (5-ASA), which is used in the treatment of ulcerative colitis. Bacterial azoreductases can selectively cleave the azo bond of olsalazine to give two equivalents of the anti-inflammatory 5-ASA locally (Figure 3.2). This is an effective strategy for the delivery of 5-ASA to the colon, since the concentration of gastrointestinal bacteria is highest in this region.[12] While olsalazine is particularly effective at maintaining patients in remission, 12 to 25% of patients experience diarrhea as a side effect, causing many to discontinue treatment.[13,14] This side effect has been attributed to increased anion secretion in the ileum as well as inhibition of NaCl absorption in the small intestine.[15,16] Sensitivity to the azo group has been found to be dose dependent,[14] and these effects have been observed with administration of other azo-containing prodrugs such as balsalazide and sulfasalazine.[17] In minimizing release of olsalazine in the small intestine, we hypothesize that these side effects may be diminished in formulations that maintain olsalazine as a solid until it reaches the target site of the colon.

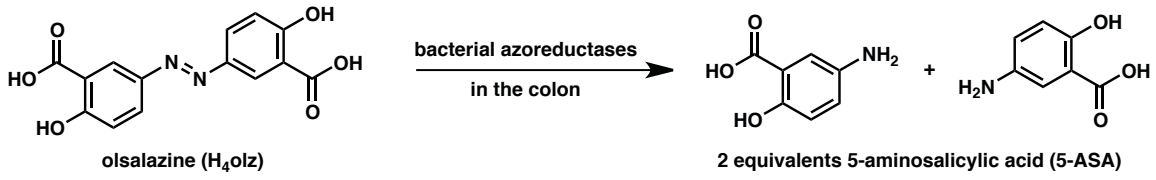

Figure 3.2. Cleavage of olsalazine in the colon by bacteria results in two equivalents of the anti-inflammatory 5-ASA.

In order to modulate release of olsalazine, efforts have been made to incorporate olsalazine in polymer matrices[18,19] and hydrogels;[20] however, the loading of olsalazine in these materials is low due to the high-molecular weight polymers required for their preparation. There are also several reported structures of olsalazine coordination solids, however, none have been tested for drug release. One-, two-, and three-dimensional materials have been prepared with alkaline earth metals,[21] transition metals,[22-25] and lanthanides.[26] All but one publication[21] employ ancillary or pillaring ligands, making them undesirable materials for olsalazine delivery.

In this study, the commercial sodium salt of olsalazine was transformed into various calcium coordination solids including one-dimensional chains, two-dimensional sheets, and a three-dimensional metal-organic framework. These calcium coordination solids are all highly crystalline and have been characterized by TGA, pXRD, and single crystal X-ray diffraction. When exposed to simulated gastrointestinal fluids, all three calcium materials released the drug more gradually when compared to the sodium salt control, which underwent rapid release of the drug. In this manner, the coordination environment of the drug can be used to tune the extent of drug release throughout the body. This strategy could be generalizable to other therapeutic compounds with Lewis basic groups.

3.2 Experimental

3.2.1 Chemicals

All reagents and solvents were obtained from commercial sources at reagent-grade purity or higher. Olsalazine acid was synthesized as described below.

3.2.2 General Characterization Methods

Laboratory powder X-ray diffraction patterns were collected on a Bruker AXS D8 Advance diffractometer equipped with Cu Kα radiation (λ = 1.5418 Å), a Göbel mirror, a Lynxeye linear position-sensitive detector, and mounting the following optics: fixed divergence slit (0.6 mm), receiving slit (3 mm) and secondary-beam Soller slits (2.5°). The generator was set at 40 kV and 40 mA. Thermogravimetric analysis was carried out at a ramp rate of 2 °C min^{-1} under nitrogen flow with a TA Instruments Q5000. Elemental analyses for C, H and N were performed at the Microanalytical Laboratory of the University of California, Berkeley using a PerkinElmer 2400 series II combustion analyzer.

3.2.3 Synthesis of $Ca(H_2olz)\cdot 4H_2O$ One-Dimensional Chains

The metal salt $Ca(NO)_3\cdot 4H_2O$ (112 mg, 0.473 mmol) was dissolved in 5 mL of water and olsalazine acid (68.0 mg, 0.225 mmol) was dissolved in 10 mL water with addition of NaOH (18.0 mg, 0.450 mmol). The olsalazine solution was allowed to reach 90 °C and the metal salt solution was added under heavy stirring. The mixed solution was heated and left stirring overnight. The dark orange powder was collected on a funnel and dried to obtain the microcrystalline powder. Yield: 79.0 mg, 85.1%. EA: calculated C 40.80% H 3.90% N 6.80%; found C 40.51%, H 3.66%, N 6.68.

Alternate synthesis for single crystals: $Ca(OAc)_2 \cdot 2H_2O$ (27.7 mg, 0.160 mmol) was dissolved in 1 mL of water and olsalazine acid (22.7 mg, 0.0750 mmol) was suspended in 4 mL of water with sonication. The combined solutions were then sonicated together and left to heat at 90 °C to produce yellow or red crystals depending on size. A shorter sonication time (1 min) correlated with larger crystals, while longer sonication times (> 5 min) produced a more uniform distribution of crystals by size.

3.2.4 Synthesis of $Ca(H_2olz) \cdot 2H_2O$ Two-Dimensional Sheets

The metal salt $Ca(NO_3)_2 \cdot 4H_2O$ (11 mg, 0.047 mmol) was dissolved in 0.5 ml of water, and olsalazine acid (6.8 mg, 0.023 mmol) was dissolved in 1 mL of water with NaOH (1.8 mg, 0.045 mmol). The solutions were combined, producing a transient yellow precipitate that dissolved upon heating at 90 °C. The vial was left to heat undisturbed at 90 °C, and after 15 min, yellow crystals were evident, and the reaction was allowed to proceed for 2 h to afford the product (4.6 mg, 58% yield). EA: calculated C 44.70%, H 3.20%, N 7.40%; found C 44.46%; H 2.96 %; N 7.39%.

Alternate synthesis: $Ca(NO_3)_2 \cdot 4H_2O$ (18.6 mg, 0.0788 mmol, 2.1 equiv.) and $Na_2(H_2olz)$ (13.0 mg, 0.0375 mmol) were dissolved in 0.5 mL and 2 mL of water, respectively. The solutions were combined, producing a transient yellow precipitate that dissolved upon heating at 90 °C. The vial was left to heat undisturbed at 90 °C to produce yellow crystals. Longer reaction times can be used to produce larger crystals. Note that sonication or stirring of the reaction mixtures described will produce the one-dimensional phase, so it is important to minimize agitation to promote formation of the two-dimensional phase.

3.2.5 Synthesis of $Ca(H_2olz) \cdot 2DMF$ Three-Dimensional Framework

The metal salt $Ca(NO_3)_2 \cdot 2H_2O$ (117 mg, 0.495 mmol) was dissolved in 12 mL of EtOH and olsalazine acid (136 mg, 0.450 mmol) was dissolved in 18 mL of DMF. These solutions were combined in a jar and separated into six 10-mL aliquots in 20-mL scintillation vials. The vials were then heated in a dry bath at 120 °C for 1 d. The solvent mixture was decanted to isolate the product as dark orange needles by filtration (124 mg, 56.5% yield). Note that washing with DMF can partially dissolve the crystals and should be avoided. Alternatively, a bulk powder can be prepared by stirring the reaction mixture described above at 120 °C. EA: Calculated C 49.4%, H 4.6%, N 11.5%; Found C 48.8%; H 4.7%; N 11.4%.

3.2.6 Conversion of $Ca(H_2olz) \cdot 2DMF$ to $Ca(H_2olz) \cdot 2MeOH \cdot H_2O$

Dried crystals of $Ca(H_2olz) \cdot 2DMF$ (124 mg) were immersed in 10 mL of methanol in a 20-mL scintillation vial at 65 °C and placed in a dry bath. The methanol was decanted and replaced with fresh methanol three times. (Yield: 107 mg, 99%). EA: calculated C 39.8%, H 3.8%, N 6.6%; found C 39.5%, H 4.0%, N 6.6%.

3.2.7 Conversion of $Ca(H_2olz) \cdot 2DMF$ or $Ca(H_2olz) \cdot 2MeOH \cdot H_2O$ to $Ca(H_2olz)$

Immersion of $Ca(H_2olz) \cdot 2DMF$ or $Ca(H_2olz) \cdot 2MeOH \cdot H_2O$ in 100 mM aqueous HCl will quickly convert the framework to the collapsed $Ca(H_2olz)$ phase quantitatively. EA. calcd. C 39.8%, H 3.8%, N 6.6%; found C 39.5%, H 4.0%, N 6.6%.

3.2.8 Synthesis of Olsalazine (1)

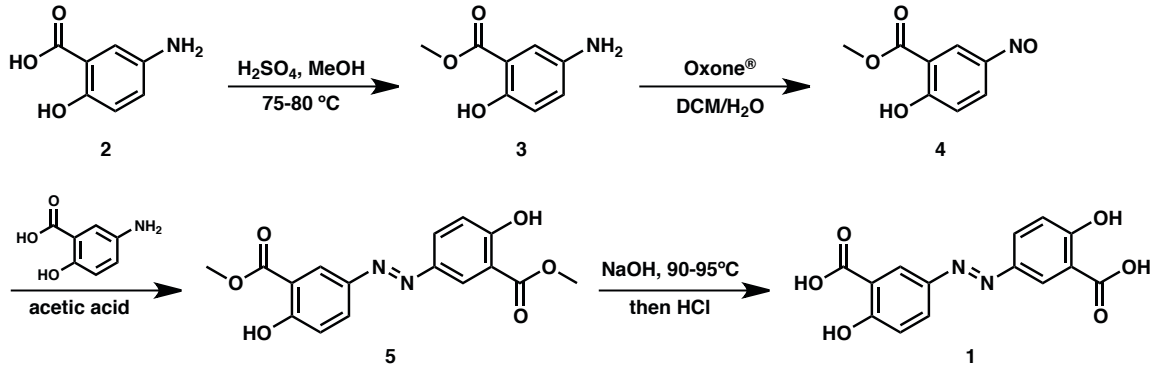

Methyl 5-aminosalicylate (3). 5-Amino salicylic acid (**2**, 20.0 g, 131 mmol) was suspended in methanol (250 mL). Concentrated sulfuric acid (10 mL) was added, and the solution was then heated to reflux (75-80 °C) with stirring. The solution was kept at reflux overnight, then cooled to ambient temperature and concentrated on a rotary evaporator. The resulting pale lavender powder was treated by slow addition of saturated sodium bicarbonate (500 mL). The product was extracted with 3 x 200 mL portions of ethyl acetate. The organic layers were combined and dried over magnesium sulfate, filtered, then concentrated on a rotary evaporator. The residue was dried under vacuum to yield the title compound as a tan solid (10.7 g, 49.2% yield).

Methyl 5-nitrososalicylate (4). To a solution of compound **3** (3.01 g, 18.0 mmol) in DCM (75 mL), a solution of Oxone (11.1 g, 18.0 mmol) in H_2O (75 mL) was added. The biphasic mixture was stirred vigorously at room temperature, as the DCM layer developed a dark green color. The progression of the reaction was monitored by HPLC until the starting material was fully consumed (usually about two hours). The layers were separated, then the aqueous layer was washed with additional DCM (2 x 75 mL). The combined organic layers were filtered through a short silica column, eluting with DCM. The filtrate was concentrated on a rotary evaporator and dried under vacuum to afford the title compound as a bright green solid (1.69 g). Some over-oxidation of nitroso to nitro was evident by LCMS. However, this did not interfere with the subsequent reaction, and the crude mixture was used in the next step without further purification.

Olsalazine methyl ester (5). The crude mixture obtained from the previous step was dissolved in acetic acid (35 mL). To this was added a solution of **3** (1.50 g, 9 mmol) in acetic acid (35 mL). The reaction mixture was stirred at room temperature overnight. The resulting precipitate was collected on a Buchner funnel and washed sequentially with acetic acid and water to afford **5** as a bright yellow solid (1.78 g, 29.9% yield, two steps).

Olsalazine (1). Compound **5** (1.75 g, 5.30 mmol) was dissolved in 50 mL aqueous NaOH (1.06 g, 26.5 mmol). The resulting deep red solution was heated to reflux (90-95 °C) with stirring. After 2 h, the reaction mixture was allowed to cool to ambient temperature. Concentrated HCl was added dropwise with stirring until no further precipitation occurred. The precipitate was collected on a Buchner funnel and washed with water to afford **1** as a yellow solid (1.492 g, 97.6%).

3.2.9 Synthesis of $Na_2(H_2olz)$

Sodium olsalazine was isolated by evaporation of water and methanol during the saponification of the olsalazine ester by sodium hydroxide. Alternatively, sodium olsalazine can be prepared by exposing olsalazine acid to two equivalents of sodium bicarbonate in water, which gave an orange-red solution. Removing the water by rotary evaporation and further drying under vacuum gave sodium olsalazine as an orange-yellow solid. EA. calcd. C 40.20%, H 3.90%, N 6.70%; found C 39.92%, H 3.67%, N 6.58%.

3.2.10 Powder X-ray Diffraction

High-resolution X-ray powder diffraction patterns of the samples were collected at the beamline 17-BM at the Advanced Photon Source (Argonne National Laboratory) with an average wavelength of 0.72768 Å. Scattered intensity was recorded by Perkin Elmer a-Si Flat Panel detector at room temperature. Prior to measurement the samples were manually powdered in a mortar and pestle and sealed in borosilicate glass capillaries of 1 mm diameter (Hilgenberg glass No. 50). The powder data analysis of $Ca(H_2olz)\cdot 2MeOH\cdot H_2O$ (pattern indexing, profile fitting, crystal structure solution and refinement) was performed with the program TOPAS 4.1.[27] The pattern indexing was done with the singular value decomposition method,[28] resulting in monoclinic unit cell. The space group was assumed to be *Cc*, which was later confirmed by the structure solution and refinement. Precise lattice parameters were determined by a Pawley fit.[29] The crystal structure of the $Ca(H_2olz)\cdot 2MeOH\cdot H_2O$ was solved by the global optimization method of simulated annealing (SA) in real space.[30] The structure solution was performed in the *Cc* space group using one rigid body for the olsalazine molecule, two methanol rigid bodies, one calcium cation and one oxygen atom representing a water molecule in the asymmetric unit. For the definition of the connectivity between the atoms within the rigid bodies, *z* matrix notation was used. During the SA runs, three rotations and three translations for each rigid body together with all possible torsion angles were set as flexible. An overall temperature factor for each atom type was included in the SA process. Once a global minimum was found, the crystal structures were subjected to Rietveld refinement,[31] in which bond lengths and angles were refined within the rigid bodies, together with free refinement of all profile and lattice parameters. The refinement converged with the following figures of merit: R_{exp} = 0.0153, R_{exp}' = 0.0311, R_{wp} = 0.0541, R_{wp}' = 0.1104, R_p = 0.0396, R_p' = 0.1035, *GOF* = 3.55 and R_{Bragg} = 0.0205. The final Rietveld plot is presented in Figure 3.S5. Hydrogen atoms were added at calculated positions by the program Mercury.[32] Crystallographic details are provided in the Supplementary Information.

3.2.11 Single Crystal X-ray Diffraction

X-ray diffraction analyses were performed on single crystals of $Ca(H_2olz)\cdot 2H_2O$ and $Ca(H_2olz)\cdot 2DMF$, which were isolated from the mother liquor, coated with Paratone-N oil, and mounted on MiTeGen loops. Crystals were frozen at a temperature of 100 K by an Oxford Cryosystems Cryostream 700 plus. Data for $Ca(H_2olz)\cdot 2H_2O$ and $Ca(H_2olz)\cdot 2DMF$ were collected at Beamline 11.3.1 at the Advanced Light Source, Lawrence Berkeley National Laboratory using synchrotron radiation (λ = 0.7749 Å). Raw data were integrated and corrected for Lorentz and polarization effects using Bruker AXS SAINT software.[33] Absorption corrections were applied using SADABS.[34] Space group

assignments were determined by examination of systematic absences, E-statistics, and successive refinement of the structures. The structures were solved using direct methods with SHELXS[35,36] and refined using SHELXL[37] operated in the OLEX2[38] interface. None of the crystals showed significant decay during data collection. Thermal parameters were refined anisotropically for all non-hydrogen atoms. Hydrogen atoms were placed in ideal positions and refined using a riding model for both structures.

3.2.12 Preparation of Pellets

Pellets were prepared from all materials using a circular die with a 4 mm diameter and pressed in a vise for 15 min under a consistent pressure. All pellets had a mass of 5.0 mg (± 0.2 mg) and an approximate thickness of 0.35 mm.

3.2.13 Olsalazine Drug Release Assay

The drug release studies were performed under conditions to simulate the passage of a solid pill through the gastrointestinal tract by placing the pellets in a solution of increasing pH. Dissolution was observed for 5 mg (± 0.2 mg) pellets in 50 mL conical tubes, which were placed horizontally in a shaking incubator with bidimensional stirring at 60 rpm at 37 ºC. 250 µL aliquots were collected every hour, and each material was tested in triplicate. The pellets were first exposed to 20 mL of the simulated gastric fluid solution for 2 hours. 16.6 mL of phosphate solution was then added to produce a simulated intestinal fluid solution of pH 6.0 and left to shake for 2 hours. Then, 14.4 mL of phosphate solution was added to produce simulated colonic fluid at pH 7.3, and the samples were left to shake for 6 hours. Simulated gastric fluid was prepared as 100 mM HCl. The basic phosphate stock solution was prepared as 45 mM NaOH and 170 mM Na_2HPO_4 resulting in a pH 11.1 solution. This method was adapted from reference [39].

3.2.14 Quantification of Olsalazine Release

Olsalazine release was measured by absorbance in 96-well Corning Costar (Tewksbury, MA) 3915 black plates. Absorbance was measured at λ = 360 nm by a Molecular Devices SpectraMax Paradigm plate reader. 75 µL aliquots from each timepoint were plated in duplicate, and each sample was measured against a calibration curve of Na_2(olz) in PBS. To account for the changes in volume throughout the experiment, the following equations was used to calculate the amount of olsalazine in solution at each time point:

$$x_n = [C]_n \times V_n \qquad \text{Equation 3.1}$$

$$x_n = x_{n-1} + [([C]_n - [C]_{n-1})(V_{n-1} - V_A)] \qquad \text{Equation 3.2}$$

where:
x_n = Total mol olsalazine released at time n
x_{n-1} = Total mol olsalazine released at time $n-1$
$[C]_n$ = Concentration at time n
$[C]_{n-1}$ = Concentration at time $n-1$
V_n = volume at time n
V_{n-1} = volume at time $n-1$
V_A = volume of aliquot removed

3.3 Results and Discussion

3.3.1 $Ca(H_2olz)\cdot 4H_2O$ One-Dimensional Chains

The structure of $Ca(H_2olz)\cdot 4H_2O$ featuring one-dimensional chains (Figure 3.3) has been reported previously where the material was made by slow evaporation from a water-ethanol mixture.[40] However, we have been able to access this structure through a rapid and straightforward synthesis requiring only water as the solvent and a reaction time of hours instead of weeks. The structure consists of pentagonal bipyramidal Ca^{2+} ions each coordinated to four water molecules and three carboxylate oxygen atoms from two different olsalazine molecules, with one carboxylate coordinating in a monodentate fashion and the other in a bidentate fashion. Each olsalazine bridges two Ca^{2+} atoms to produce one-dimensional chains.

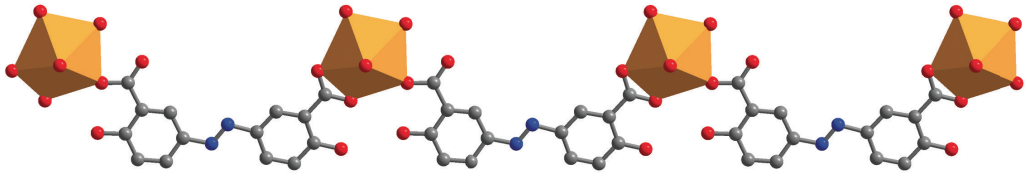

Figure 3.3. A portion of the crystal structure of $Ca(H_2olz)\cdot 4H_2O$ one-dimensional chains, as reported previously.[40] Grey, blue, and red spheres represent carbon, nitrogen, and oxygen atoms, respectively. Orange surfaces represent the polyhedra formed by the first coordination sphere of the Ca^{2+} ions; hydrogen atoms are omitted for clarity.

3.3.2 $Ca(H_2olz)\cdot 2H_2O$ Two-Dimensional Sheets

We have discovered a new two-dimensional phase, $Ca(H_2olz)\cdot 2H_2O$, and determined its structure by single crystal X-ray diffraction (Figure 3.4). These sheets within this crystal structure are comprised of pentagonal bipyramidal Ca^{2+} atoms, which are each coordinated to two water molecules; the remaining sites on calcium are coordinated to bridging bidentate carboxylate groups from olsalazine. This phase can be obtained by a similar method to the one-dimensional chains. However, a crucial difference lies in whether the solution is agitated or left standing. Sonication or stirring of the reaction mixture will produce the one-dimensional phase, while leaving the reaction undisturbed will favor the two-dimensional phase, suggesting a delicate balance in the reaction kinetics that can push the material to form one phase versus the other.

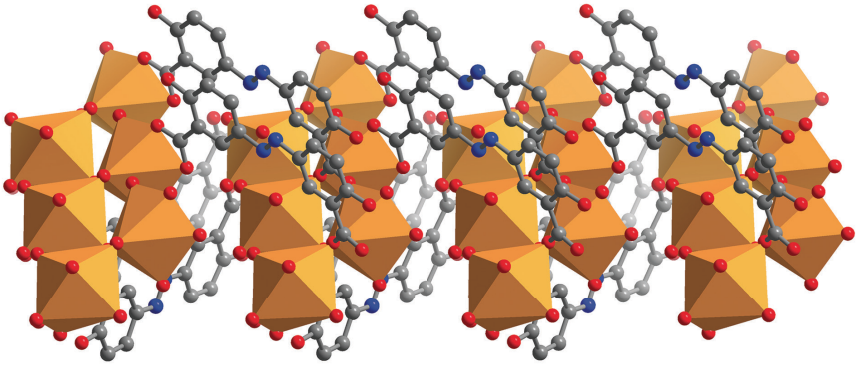

Figure 3.4. A portion of the crystal structure of $Ca(H_2olz)\cdot 2H_2O$ two-dimensional sheets. Grey, blue, and red spheres represent carbon, nitrogen, and oxygen, respectively. Orange surfaces represent the polyhedra formed by the first coordination sphere of the Ca^{2+} ions; hydrogen atoms are omitted for clarity.

3.3.3 $Ca(H_2olz)\cdot 2DMF$ Three-Dimensional Framework

A three-dimensional metal-organic framework with calcium and olsalazine can be prepared solvothermally from a mixture of DMF and ethanol to produce large single crystals of $Ca(H_2olz)\cdot 2DMF$ (Figure 3.5). The framework crystallizes in the space group *Cc* as twinned crystals, and the unit cell parameters are: $a = 24.40(2)$ Å, $b = 8.975(4)$ Å, $c = 10.381(6)$ Å, $\alpha = 90°$, $\beta = 97.619(2)°$, $\gamma = 90°$. In this structure, the Ca^{2+} ions exhibit an octahedral coordination environment with two DMF molecules bound in the axial positions and carboxylate oxygen atoms from four different olsalazine ligands in the equatorial positions. This material is the first three-dimensional framework reported with olsalazine as the sole ligand.

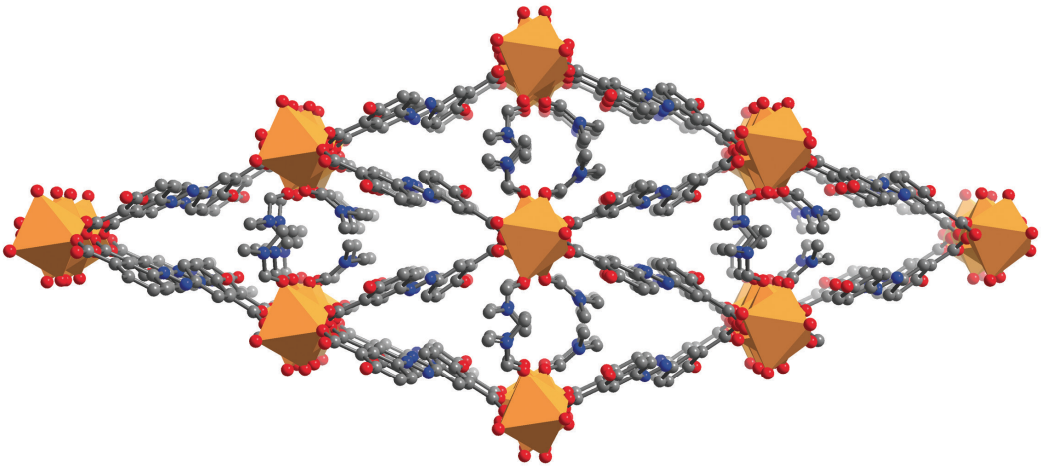

Figure 3.5. A portion of the crystal structure of the three-dimensional metal-organic framework $Ca(H_2olz)\cdot 2DMF$. Grey, blue, and red spheres represent carbon, nitrogen, and oxygen, respectively. Orange surfaces represent the polyhedra formed by the first coordination sphere of the Ca^{2+} ions; hydrogen atoms are omitted for clarity.

3.3.4 Flexibility of Ca(H_2olz) Framework Upon Solvent Exchange

The Ca(H_2olz)·2DMF framework demonstrates remarkable flexibility and undergoes significant structural changes upon immersion in different solvents. The dramatic flexing of this material after solvent exchange destroys the single crystals, thereby requiring powder X-ray diffraction for structural analysis. With exposure of Ca(H_2olz)·2DMF to wet methanol, the two coordinated DMF molecules are replaced by one methanol and one water molecule; an additional methanol molecule resides in the pore (Figure 3.6). Connectivity of the olsalazine ligand to calcium is maintained throughout this flexing. However, there is a dramatic shift in the positions of the solvent molecules. In the original structure, the DMF molecules are *trans* to one another, whereas the bound solvent molecules in the methanol structure are *cis* to one another with an additional methanol molecule in the pore. The material can be reversibly solvated by exchanging DMF and methanol. Similar behavior has been observed in a cobalt benzotriazolide-5-carboxylato framework where the frameworks can undergo flexing to accommodate DMF or methanol.[41]

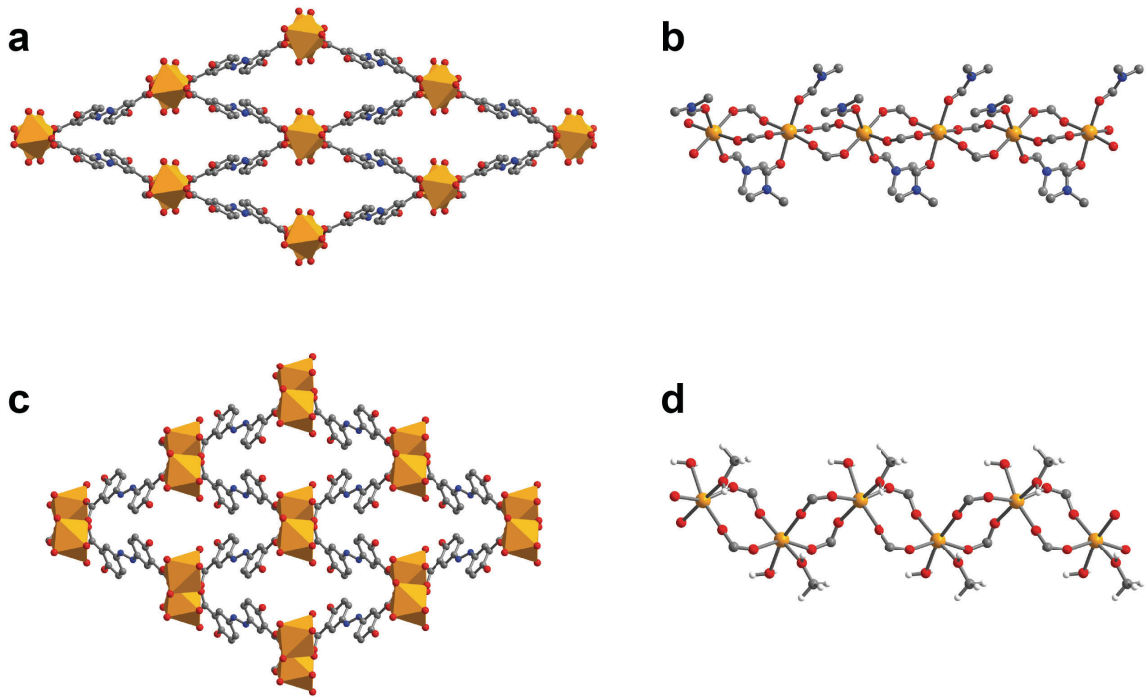

Figure 3.6. Structural changes of the Ca(H_2olz) three-dimensional framework under different solvation conditions. The Ca(H_2olz)·2DMF structure is shown as (a) viewed down *c*-axis and (b) viewed down *b*-axis. The Ca(H_2olz)·2MeOH·H_2O structure is shown as (c) viewed down *c*-axis and (d) viewed down *b*-axis. Solvent molecules omitted from (a) and (c) to emphasize structural changes to framework. Some hydrogen atoms omitted for clarity.

Upon exposure of either the DMF or methanol phases to 100 mM HCl, another highly crystalline phase is obtained. The structure of this phase was not determined by powder X-ray diffraction because the unit cell parameters could not be solved. The original DMF or methanol phases cannot be readily obtained by re-immersing the material in these solvents, suggesting that the ligand coordination mode has changed (Figure 3.7). By TGA, this phase exhibits a single mass loss at ~250 ºC, which is consistent with a collapsed, dense phase containing no solvent. This Ca(H_2olz) material much higher percentage of the active pharmaceutical ingredient (88%) than the commercially available disodium olsalazine (79%), making it an attractive alternative to the current formulation as the sodium salt.

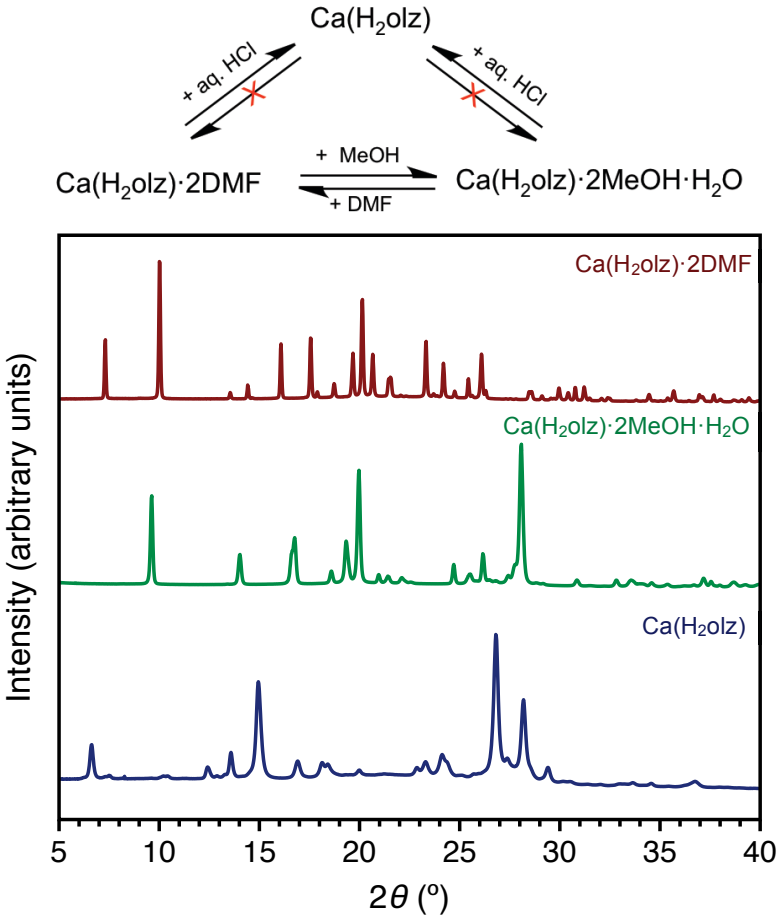

Figure 3.7. Flexibility of the Ca(H_2olz) three-dimensional metal-organic framework exhibited by powder X-ray diffraction (λ = 1.5418 Å). Schematic illustrates the reversibility between the DMF and methanol-solvated structures and the irreversible change that occurs after exposure to 100 mM HCl. Powder X-ray diffraction patterns shown from top to bottom: Ca(H_2olz)·2DMF as synthesized, Ca(H_2olz)·2MeOH·H_2O, and HCl-treated Ca(H_2olz). When either the DMF or methanol-solvated phases are immersed in 100 mM HCl, a collapsed dense phase is obtained, which cannot be used to regenerate either the DMF or methanol structure without partial dissolution of the framework.

3.3.5 Olsalazine Release Assays

The one-, two-, and three-dimensional calcium-olsalazine coordination solids were tested against sodium olsalazine, which is the commercial composition of the medication (sold as Dipentum®). In order to simulate the passage of a pill through the gastrointestinal tract, pellets of each material were pressed and exposed to solutions that mimic the pH and transit times of the stomach, small intestine, and colon (Figure 3.8a). In this study, time points were taken every hour to follow the dissolution of the materials and the corresponding release of olsalazine. The release was carried out in three phases where the first two hours were at pH 1.1, the next two hours were at pH 6.0, and the final six hours were at pH 7.3. The vessels containing the pellet in 20 to 50 mL release media were shaken at 60 rpm at 37 ºC to simulate the motion and temperature of the body.

It is important to note that the pellets were prepared from pure material without binders or other agents typically used for pill preparation in the pharmaceutical industry. This was done in order to better measure intrinsic dissolution rates of each material. However, some pellets disintegrated once in contact with solution, which could have accelerated the observed dissolution rates due to the increase in surface area. Notably, the three-dimensional Ca(H_2olz) framework consistently resisted disintegration and remained an intact pellet throughout the experiment, whereas the other materials all exhibited disintegration.

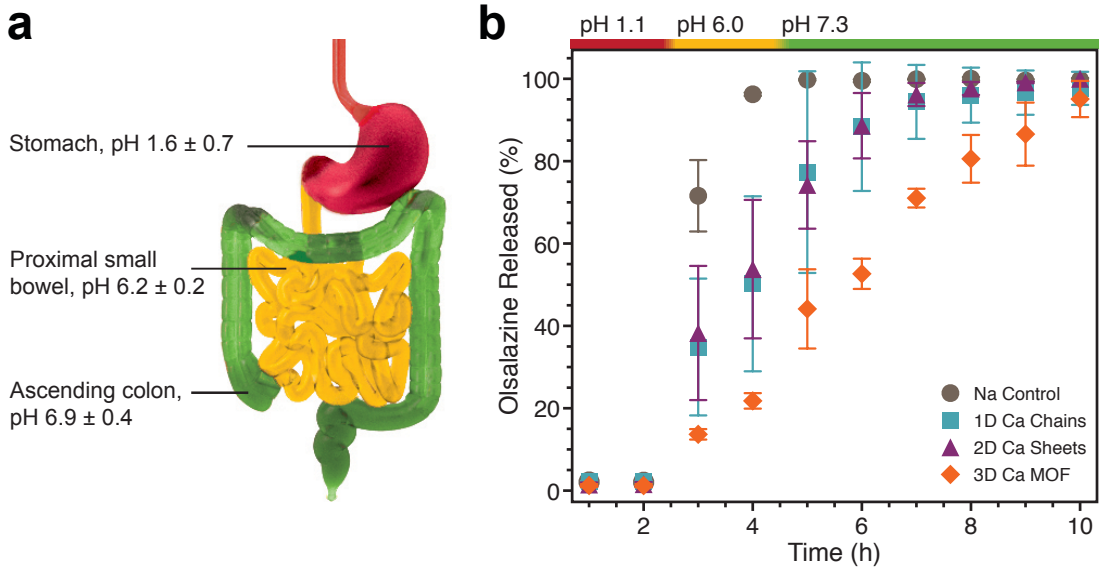

Figure 3.8. (a) Schematic of typical pH ranges observed in the gastrointestinal tract if a pill is administered 30 min before eating (values from ref. 42). (b) Drug release of Ca(H_2olz) materials and Na_2(H_2olz) control at increasing pH from pH 1.1 (red), pH 6.0 (yellow), and pH 7.3 (green). Drug release data is shown for Na_2(H_2olz) control (grey circles), Ca(H_2olz)·4H_2O 1D chains (teal squares), Ca(H_2olz)·2H_2O 2D sheets (purple triangles), and Ca(H_2olz) 3D framework (orange diamonds).

All three of the $Ca(H_2olz)$ materials outperformed $Na_2(H_2olz)$ in this simulated gastrointestinal environment (Figure 3.8b). While all materials resisted dissolution at pH 1.1, $Na_2(H_2olz)$ dissolved far more rapidly at pH 6.0 and above. This is particularly clear when comparing the amount of drug released at the four-hour time point where over 95% of the $Na_2(H_2olz)$ had been released while only about 50% of olsalazine had been released from the one-dimensional $Ca(H_2olz)\cdot 4H_2O$ chains or the two-dimensional $Ca(H_2olz)\cdot 2H_2O$ sheets. Even more impressive, the three-dimensional $Ca(H_2olz)$ framework had released less than 25% of the drug at the same point. While some of this advantage of the three-dimensional material over the others could be attributed to differences in pellet integrity, it is nevertheless clear that the one- and two-dimensional calcium materials show slower release over the sodium control. The slower dissolution rate of the calcium coordination solids over the sodium salt may be due to differences in coordination strength when comparing dicationic calcium versus monocationic sodium. Furthermore, the extended network of the calcium coordination solids may increase the hydrophobicity and hamper hydrolysis of the material more effectively than the sodium salt. Together, these features may make calcium-olsalazine coordination solids a viable alternative to the current sodium formulation of olsalazine.

3.4 Conclusions

We have formed various biocompatible calcium coordination solids with olsalazine. One-dimensional chains of $Ca(H_2olz)\cdot 4H_2O$ have been made through a faster synthesis than previously reported with conditions that require only water as the solvent. A new two-dimensional phase of $Ca(H_2olz)\cdot 2H_2O$ was also prepared, and its sheet-like structure was determined by single crystal X-ray diffraction. A new three-dimensional framework of $Ca(H_2olz)\cdot 2DMF$ was also discovered, and it exhibits remarkable flexibility upon immersion in different solvents such as methanol and aqueous acid. Upon exposure of this material to aqueous HCl, we produce a dense $Ca(H_2olz)$ phase with no solvent bound.

We have also tested these $Ca(H_2olz)$ materials for release of the drug under simulated gastrointestinal conditions. We found that all three calcium-olsalazine materials tested were more resistant to release of olsalazine under conditions simulating the small intestine as compared to the commercial sodium-olsalazine formulation. While olsalazine is an effective medication for the treatment of ulcerative colitis, severe side effects have been attributed to high levels of the soluble drug in the small intestine. We propose that these issues could be ameliorated by using our pH-responsive calcium-olsalazine materials that minimize release of olsalazine under the acidic conditions of the stomach and small intestine while selectively releasing the bulk of the drug under the neutral conditions of the colon.

Furthermore, both the two-dimensional $Ca(H_2olz)\cdot 2H_2O$ and three-dimensional $Ca(H_2olz)$ phases have a higher percentage of the active pharmaceutical ingredient by weight (80% and 88%, respectively) than the commercially available disodium olsalazine (79%). Since patients are often required to take 2-3 gram doses of olsalazine per day, a higher efficiency product by weight would be another marked improvement over the

current sodium salt formulation. Thus, these calcium-olsalazine coordination solids are promising materials for use in treatment of ulcerative colitis. We hope that this metal coordination strategy can be adapted to modulate release of other drug systems in the future.

3.5 Acknowledgements

I thank M. I. Gonzalez for performing structure determination by single crystal X-ray diffraction and for optical microscopy images, T. Runcevski for structure determination by powder X-ray diffraction, C. M. Legendre for assistance with material synthesis and release studies, J. Oktawiec for collection of powder X-ray diffraction data, K. A. Colwell for scanning electron microscopy studies, and J. R. Long for support. D.J.L. was funded by the Soroptimist International Founder Region Dissertation Fellowship. We also thank the Advanced Light Source at the Lawrence Berkeley National Laboratory (Contract No. DE-AC02-05CH11231) and the Advanced Photon Source at the Argonne National Laboratory (Contract No. DE-AC02-06CH11357) for access to instrumentation.

3.6 References

(1) Miller, S. R., Heurtaux, D., Baati, T., Horcajada, P., Grenèche, J.-M., and Serre, C. (2010) Biodegradable therapeutic MOFs for the delivery of bioactive molecules. *Chem. Commun. 46*, 4526–4528.
(2) Burrows, A. D., Jurcic, M., Keenan, L. L., Lane, R. A., Mahon, M. F., Warren, M. R., Nowell, H., Paradowski, M., and Spencer, J. (2013) Incorporation by coordination and release of the iron chelator drug deferiprone from zinc-based metal–organic frameworks. *Chem. Commun. 49*, 11260–11262.
(3) Cooper, L., Hidalgo, T., Gorman, M., Lozano-Fernández, T., Simón-Vázquez, R., Olivier, C., Guillou, N., Serre, C., Martineau, C., Taulelle, F., Damasceno-Borges, D., Maurin, G., González-Fernández, Á., Horcajada, P., and Devic, T. (2015) A biocompatible porous Mg-gallate metal-organic framework as an antioxidant carrier. *Chem. Commun. 51*, 5848–5851.
(4) Su, H., Sun, F., Jia, J., He, H., Wang, A., and Zhu, G. (2015) A highly porous medical metal-organic framework constructed from bioactive curcumin. *Chem. Commun. 51*, 5774–5777.
(5) Amo-Ochoa, P., Alexandre, S. S., Hribesh, S., Galindo, M. A., Castillo, O., Gómez-García, C. J., Pike, A. R., Soler, J. M., Houlton, A., Zamora, F., Harrington, R. W., and Clegg, W. (2013) Coordination chemistry of 6-thioguanine derivatives with cobalt: toward formation of electrical conductive one-dimensional coordination polymers. *Inorg. Chem. 52*, 5290–5299.
(6) Amo-Ochoa, P., Castillo, O., Alexandre, S. S., Welte, L., de Pablo, P. J., Rodríguez-Tapiador, M. I., Gómez-Herrero, J., and Zamora, F. (2009) Synthesis of designed conductive one-dimensional coordination polymers of Ni(II) with 6-mercaptopurine and 6-thioguanine. *Inorg. Chem. 48*, 7931–7936.
(7) Amo-Ochoa, P., Castillo, O., Gómez-García, C. J., Hassanein, K., Verma, S., Kumar, J., and Zamora, F. (2013) Semiconductive and magnetic one-dimensional coordination polymers of Cu(II) with modified nucleobases. *Inorg. Chem. 52*, 11428–11437.
(8) Yuan, R.-X., Xiong, R.-G., Abrahams, B. F., Lee, G.-H., Peng, S.-M., Che, C.-M.,

and You, X.-Z. (2001) A Cu(I) coordination polymer employing a nonsteroidal aromatase inhibitor letrozole as a building block. *J. Chem. Soc., Dalton Trans.* 2071–2073.
(9) Tang, Y.-Z., Zhou, M., Huang, J., Cao, Z., Qi, T.-T., Huang, G.-H., and Wen, H.-R. (2012) Synthesis, crystal structure, and characterization of three new letrozole complexes. *Z. anorg. allg. Chem. 638*, 372–376.
(10) Zhao, Y. N., Zhang, C. C., Zhai, Q. G., Li, S. N., and Jiang, Y. C. (2013) Solvent-introduced two novel copper (II)–letrozolate compounds: Solvothermal synthesis, crystal structures and photoluminescence property. *Inorg. Chim. Acta 405*, 176–181.
(11) Price, J. D., Piccariello, T., and Oberlender, R. A. (2010) Bismuth-containing compounds, coordination polymers, methods for modulating pharmacokinetic properties of biologically active agents, and methods for treating patients. US Patent Office.
(12) Oz, H. S., and Ebersole, J. L. (2008) Application of prodrugs to inflammatory diseases of the gut. *Molecules 13*, 452–474.
(13) H, S.-G., G, J., and W, K. (1986) Azodisal sodium in the treatment of ulcerative colitis: A study of tolerance and relapse-prevention properties. *Gastroenterology 90*, 1024–1030.
(14) Sandberg-Gertzén, H., Järnerot, G., Bukhave, K., Lauritsen, K., and Rask-Madsen, J. (1986) Effect of azodisal sodium and sulphasalazine on ileostomy output of fluid and PGE2 and PGF2 alpha in subjects with a permanent ileostomy. *Gut 27*, 1306–1311.
(15) Goerg, K. J., Wanitschke, R., Diehl, P. H., and Meyer zum Büschenfelde, K. H. (1988) Secretory effect of azodisalicylate (azodisal sodium) on the short circuited mucosa of the rat ileum in vitro. *Gut 29*, 336–341.
(16) Pamukcu, R., Hanauer, S. B., and Chang, E. B. (1988) Effect of disodium azodisalicylate on electrolyte transport in rabbit ileum and colon in vitro: comparison with sulfasalazine and 5-aminosalicylic acid. *Gastroenterology 95*, 975–981.
(17) Kles, K. A., Vavricka, S. R., Turner, J. R., Musch, M. W., Hanauer, S. B., and Chang, E. B. (2005) Comparative analysis of the in vitro prosecretory effects of balsalazide, sulfasalazine, olsalazine, and mesalamine in rabbit distal ileum. *Inflamm. Bowel Dis. 11*, 253–257.
(18) Mahkam, M., Assadi, M. G., Zahedifar, R., Ramesh, M., and Davaran, S. (2004) Linear type azo-containing polyurethanes for colon-specific drug delivery. *J. Bioact. Compat. Polym. 19*, 45–53.
(19) Lai, J., Wang, L.-Q., Tu, K., Zhao, C., and Sun, W. (2005) Linear azo polymer containing conjugated 5,5′-azodisalicylic acid segments in the main chain: synthesis, characterization, and degradation. *Macromol. Rapid Commun. 26*, 1572–1577.
(20) Li, X., Li, J., Gao, Y., Kuang, Y., Shi, J., and Xu, B. (2010) Molecular nanofibers of olsalazine form supramolecular hydrogels for reductive release of an anti-inflammatory agent. *J. Am. Chem. Soc. 132*, 17707–17709.
(21) Tang, Y.-Z., Tan, Y.-H., Chen, S.-H., Chao, Y.-W., and Wang, P. (2008) Synthesis, characterization and crystal structures of two alkaline-earth metal complexes of olsalazine. *J. Coord. Chem. 61*, 1244–1252.
(22) Tan, Y.-H., Huang, Z.-Q., Chen, S.-H., Xie, X.-B., and Xia, L.-B. (2007) *catena*-Poly[[tetraaquamanganese(II)]-μ-6,6′-dihydroxy-3,3′-diazenediyldibenzoato-κ^2 O:O′]. *Acta Crystallogr. Sect. E.-Struct Rep. Online 63*, m2948–m2949.
(23) Xiao, D.-R., Sun, D.-Z., Liu, J.-L., Zhang, G.-J., Chen, H.-Y., He, J.-H., Yan, S.-W., Yuan, R., and Wang, E.-B. (2011) Two unprecedented entangled metal–olsalazine

complexes with coexistence of 2D → 3D polycatenation and meso-helix. *Eur. J. Inorg. Chem. 2011*, 4656–3663.
(24) Chen, H.-Y., Xiao, D.-R., Yan, S.-W., He, J.-H., Yang, J., Wang, X., Yuan, R., and Wang, E.-B. (2012) Two three-dimensional pillared metal-olsalazine complexes based on infinite rod-shaped secondary building units. *Inorg. Chim. Acta 387*, 283–288.
(25) Tang, Y.-Z., Tan, Y.-H., Chen, S.-H., and Chao, Y.-W. (2007) A novel two-dimensional coordination polymer based on rhombic tetrameric subunit Zn_4O_4 as building block. *Z. anorg. allg. Chem. 633*, 332–335.
(26) Tang, Y.-Z., Tan, Y.-H., Ge, Z.-T., Liu, Z.-X., Liao, C.-F., and Xie, X.-B. (2009) Synthesis and crystal structures of two rare-earth metal polymers of olsalazine. *J. Coord. Chem. 62*, 2682–2688.
(27) Bruker AXS. (2007) TOPAS-Academic, Version 4.1.
(28) Coelho, A. A., IUCr. (2003) Indexing of powder diffraction patterns by iterative use of singular value decomposition. *J. Appl. Cryst. 36*, 86–95.
(29) Pawley, G. S. (1981) Unit-cell refinement from powder diffraction scans. *J. Appl. Cryst. 14*, 357–361.
(30) Andreev, Y. G., MacGlashan, G. S., and Bruce, P. G. (1997) Ab initio solution of a complex crystal structure from powder-diffraction data using simulated-annealing method and a high degree of molecular flexibility. *Phys. Rev. B 55*, 12011–12017.
(31) Rietveld, H. M., IUCr. (1969) A profile refinement method for nuclear and magnetic structures. *J. Appl. Cryst. 2*, 65–71.
(32) Mercury CSD. (2013) Version 3.3 (Build RC5).
(33) Bruker Analytical X-ray Systems Inc. SAINT and APEX 2 Software for CCD Diffractometers. Madison, WI, USA.
(34) Sheldrick, G. M. SADABS, Bruker Analytical X-ray Systems Inc. Madison, WI, USA.
(35) Sheldrick, G. M. (2014) SHELXS. *University of Göttingen, Germany*.
(36) Sheldrick, G. M. (2007) A short history of SHELX. *Acta Crystallogr. Sect. A 64*, 112–122.
(37) Sheldrick, G. M. (2014) SHELXL. *University of Göttingen, Germany*.
(38) Dolomanov, O. V., Bourhis, L. J., Gildea, R. J., Howard, J. A. K., and Puschmann, H. (2009) OLEX2: a complete structure solution, refinement and analysis program. *J. Appl. Cryst. 42*, 339–341.
(39) Chuong, M. C., Christensen, J. M., and Ayres, J. W. (2008) New dissolution method for mesalamine tablets and capsules. *Dissolution Technol. 15*, 7–14.
(40) Tang, Y.-Z., Tan, Y.-H., Chen, S.-H., Chao, Y.-W., and Wang, P. (2008) Synthesis, characterization and crystal structures of two alkaline-earth metal complexes of olsalazine. *J. Coord. Chem. 61*, 1244–1252.
(41) Lanza, A., Germann, L. S., Fisch, M., Casati, N., and Macchi, P. (2015) Solid-state reversible nucleophilic addition in a highly flexible MOF. *J. Am. Chem. Soc. 137*, 13072–13078.
(42) Ibekwe, V. C., Fadda, H. M., McConnell, E. L., Khela, M. K., Evans, D. F., and Basit, A. W. (2008) Interplay between intestinal pH, transit time and feed status on the in vivo performance of pH responsive ileo-colonic release systems. *Pharm. Res. 25*, 1828–1835.

3.7 Supplementary Information

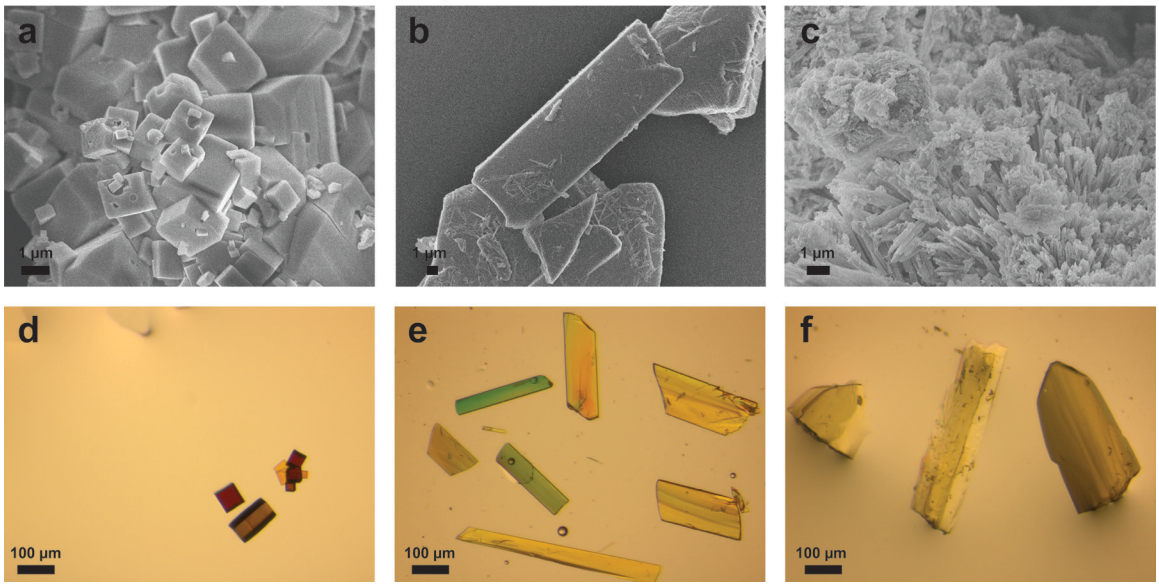

Figure 3.S1. Scanning electron microscopy images (a-c) and optical microscopy images (d-f) of microcrystalline and single crystal Ca(H_2olz) materials show that the synthetic conditions can be tuned to control particle size while maintaining the same crystal morphology. 1D Ca(H_2olz)·4H_2O chains (a,d), 2D Ca(H_2olz)·2H_2O sheets (b,e), and 3D Ca(H_2olz)·2DMF MOF (c,f).

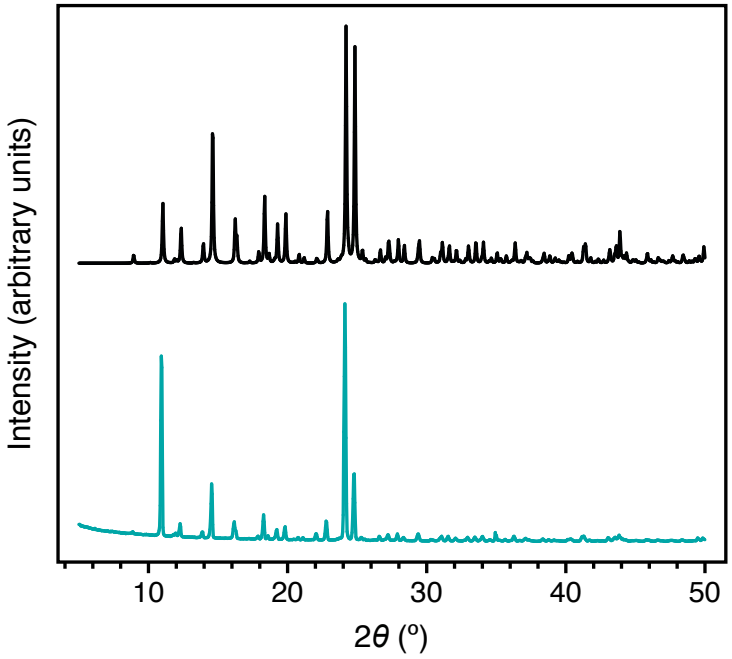

Figure 3.S2. Comparison of the predicted (black) and experimental (teal) powder X-ray diffraction patterns for $Ca(H_2olz)\cdot 4H_2O$ one-dimensional chains.

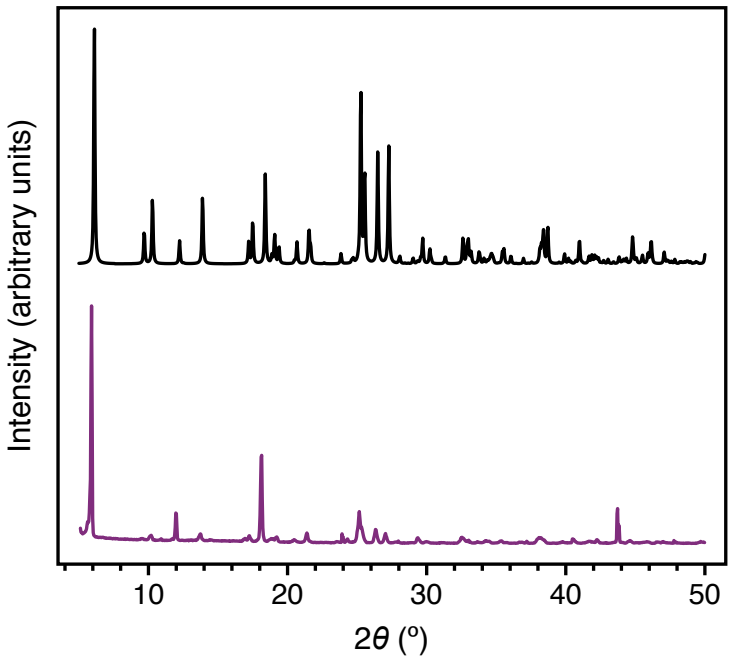

Figure 3.S3. Comparison of the predicted (black) and experimental (purple) powder X-ray diffraction patterns for $Ca(H_2olz)\cdot 2H_2O$ two-dimensional sheets.

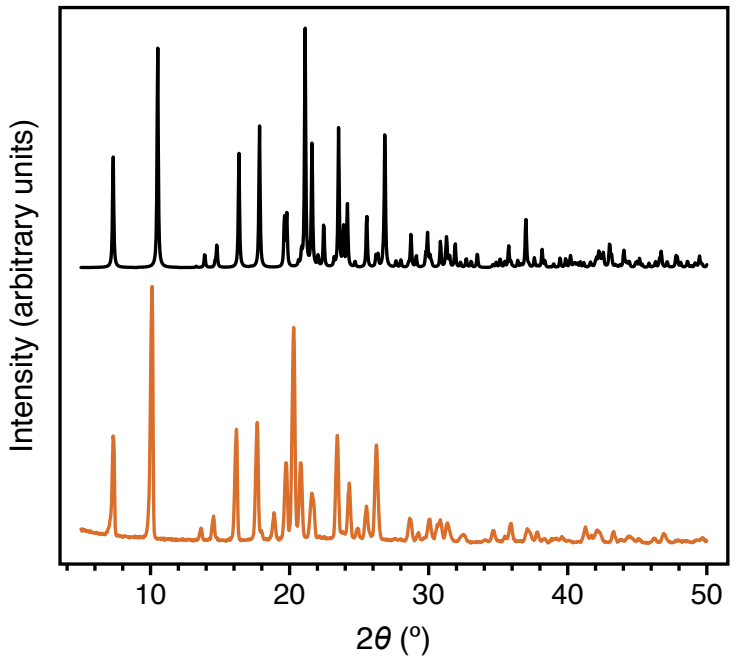

Figure 3.S4. Comparison of the predicted (black) and experimental (orange) powder X-ray diffraction patterns for Ca(H_2olz)·2DMF three-dimensional metal-organic framework.

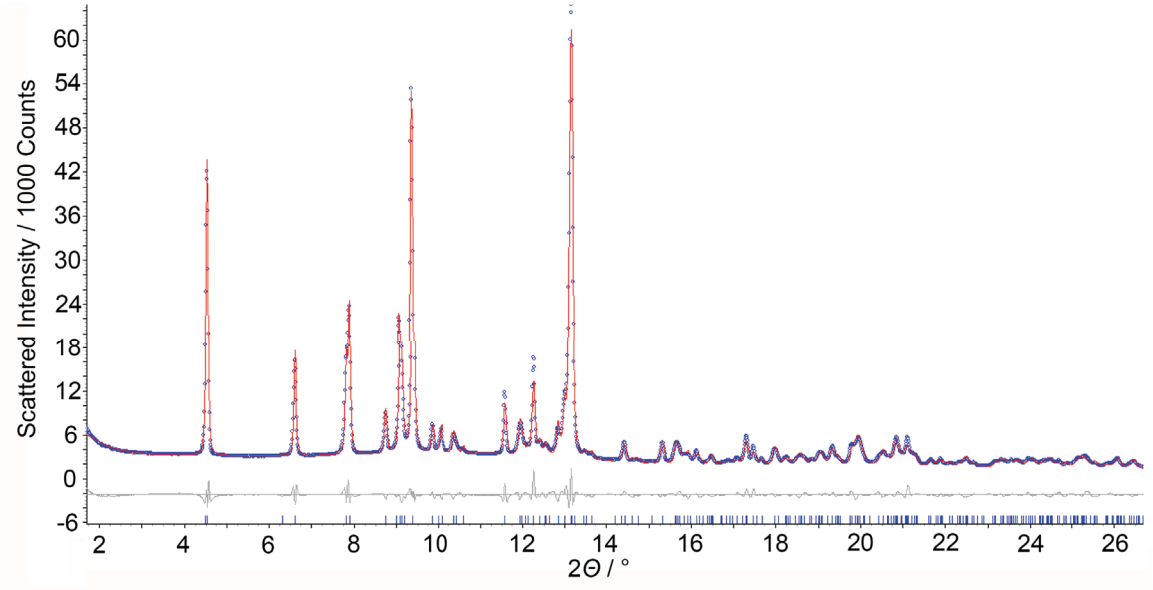

Figure 3.S5. Rietveld refinement plot of Ca(H_2olz)·2MeOH·H_2O (λ = 0.41397 Å). Measured scattered intensity is presented with blue dots; the best fit with read line and the corresponding difference plot with gray line. The Bragg reflections are given with blue bars.

Table 3.S1. Crystal data and structure refinement for $Ca(H_2olz)\cdot 2H_2O$.

Empirical formula	$C_{14}H_{12}N_2O_8Ca$	
Formula weight	376.34	
Temperature	100(2) K	
Wavelength	0.7749 Å	
Crystal system	Monoclinic	
Space group	$P12_11$	
Unit cell dimensions	a = 9.3413(5) Å	α = 90°.
	b = 5.4114(3) Å	β = 102.423(4)°.
	c = 14.8190(8) Å	γ = 90°.
Volume	731.55(7) Å^3	
Z	2	
Density (calculated)	1.708 Mg/m^3	
Absorption coefficient	0.609 mm^{-1}	
F(000)	388	
Crystal size	0.1 x 0.1 x 0.06 mm^3	
Theta range for data collection	2.434 to 35.328°.	
Index ranges	$-13 \leqq h \leqq 13, -8 \leqq k \leqq 8, -22 \leqq l \leqq 22$	
Reflections collected	13254	
Independent reflections	4993 [R(int) = 0.0521]	
Completeness to theta = 27.706°	99.9 %	
Absorption correction	Semi-empirical from equivalents	
Max. and min. transmission	0.964 and 0.860	
Refinement method	Full-matrix least-squares on F^2	
Data / restraints / parameters	4993 / 5 / 240	
Goodness-of-fit on F^2	1.006	
Final R indices [I>2sigma(I)]	R1 = 0.0437, wR2 = 0.0792	
R indices (all data)	R1 = 0.0598, wR2 = 0.0840	
Absolute structure parameter	0.053(18)	
Extinction coefficient	n/a	
Largest diff. peak and hole	0.521 and –0.404 e.Å^{-3}	

Table 3.S2. Crystal data and structure refinement for $Ca(H_2olz)\cdot 2DMF$.

Empirical formula	$C_{20}H_{22}N_4O_8$ Ca	
Formula weight	486.49	
Temperature	100(2) K	
Wavelength	0.7749 Å	
Crystal system	Monoclinic	
Space group	*Cc*	
Unit cell dimensions	a = 24.2849(11) Å	α = 90°
	b = 9.0194(5) Å	β = 97.936(3)°
	c = 10.3673(5) Å	γ = 90°
Volume	2249.06(19) Å^3	
Z	4	
Density (calculated)	1.437 Mg/m^3	
Absorption coefficient	0.420 mm^{-1}	
F(000)	1016	
Crystal size	0.03 x 0.025 x 0.025 mm^3	
Theta range for data collection	2.630 to 31.133°.	
Index ranges	$-32 \leqq h \leqq 32, -11 \leqq k \leqq 11, -13 \leqq l \leqq 13$	
Reflections collected	29931	
Independent reflections	5796 [R(int) = 0.0562]	
Completeness to theta = 27.706°	99.9 %	
Absorption correction	Semi-empirical from equivalents	
Max. and min. transmission	0.990 and 0.888	
Refinement method	Full-matrix least-squares on F^2	
Data / restraints / parameters	5796 / 2 / 307	
Goodness-of-fit on F^2	1.048	
Final R indices [I>2sigma(I)]	R1 = 0.0576, wR2 = 0.1463	
R indices (all data)	R1 = 0.0783, wR2 = 0.1600	
Absolute structure parameter	–0.03(2)	
Extinction coefficient	n/a	
Largest diff. peak and hole	0.580 and –0.450 e.Å^{-3}	

Table 3.S3. Powder data and structure refinement for $Ca(H_2olz)\cdot 2MeOH\cdot H_2O$.

Empirical formula	$C_{16}H_{16}N_2O_8Ca$	
Formula weight	422.41	
Crystal system	monoclinic	
Space group	*Cc*	
Unit cell dimensions	*a* = 18.6277(3) Å	α = 90°
	b = 10.572(4) Å	β = 84.64(1)°
	c = 9.1180(3) Å	γ = 90°
Volume	1787.8(9) $Å^3$	
Z	4	
Experimental crystal description	powder	
Experimental crystal color	yellow	
Experimental crystal density method	not measured	
Experimental absorptioncorrection type	none	
Refine ls hydrogen treatment	noref	
Refine ls number parameters	89	
Diffraction ambient temperature	293 K	
Cell measurement temperature	293 K	
Diffraction radiation type	synchrotron	
Diffraction radiation wavelength	0.41397 Å	
Diffraction measurement device type	synchrotron	

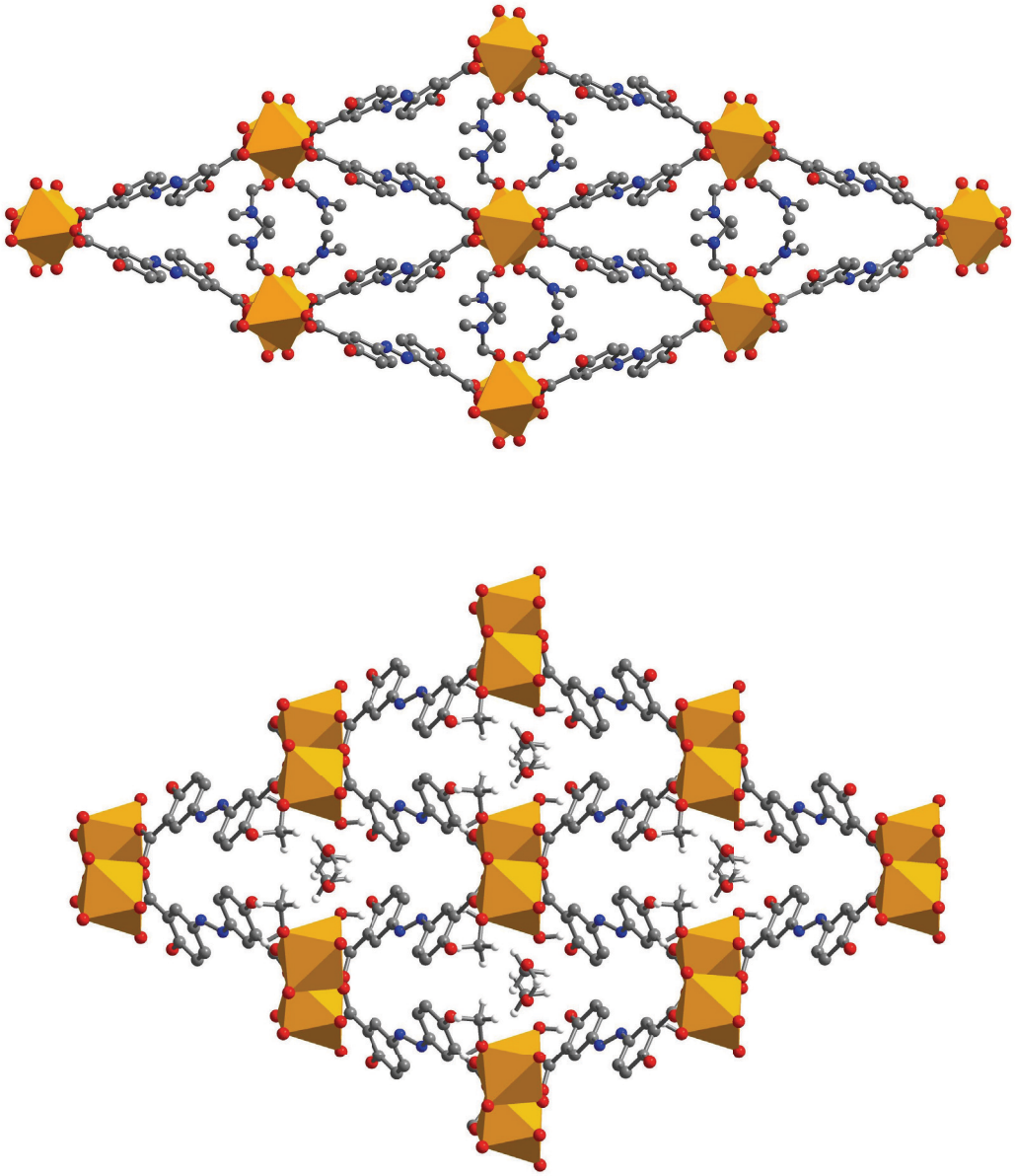

Figure 3.S6. Structural changes of the Ca(H_2olz) three-dimensional framework under different solvation conditions as viewed down the *c*-axis. Top: A portion of the structure of Ca(H_2olz)·2DMF. Bottom: A portion of the structure of Ca(H_2olz)·2MeOH·H_2O. Grey, blue, red, and white spheres represent carbon, nitrogen, oxygen, and hydrogen, respectively. Orange surfaces represent the polyhedra formed by the first coordination sphere of the Ca^{2+} ions; some hydrogen atoms are omitted for clarity.

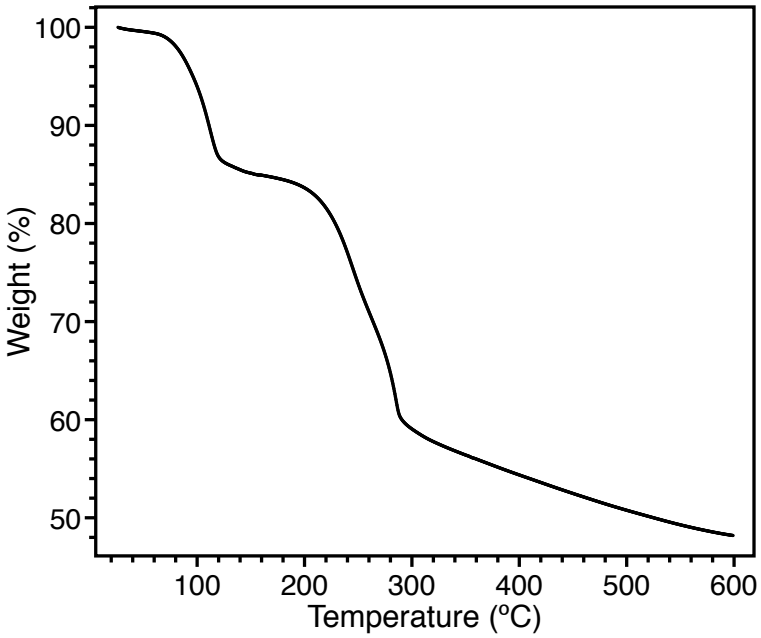

Figure 3.S7. Thermogravimetric analysis of $Ca(H_2olz)\cdot 4H_2O$ one-dimensional chains. First weight loss event corresponds to loss of two water molecules. Subsequent weight loss corresponds to loss of the remaining two water molecules and decomposition of the material.

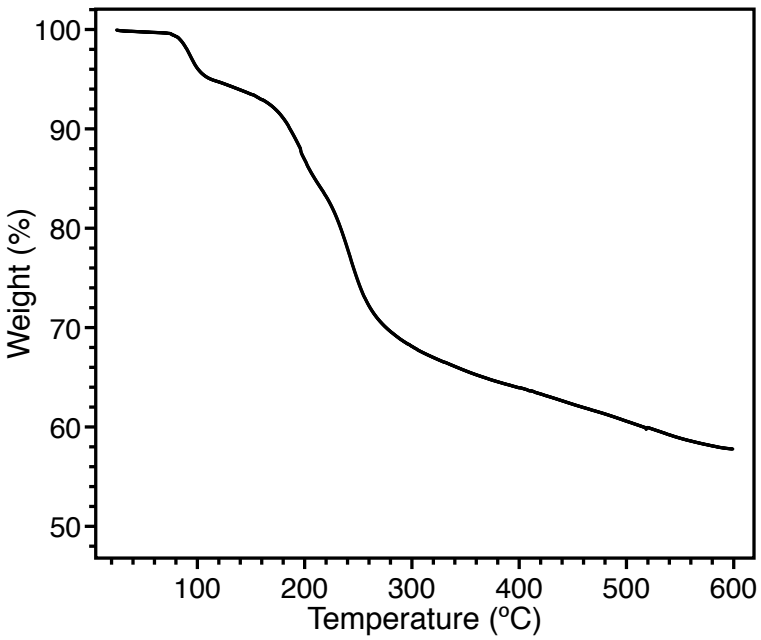

Figure 3.S8. Thermogravimetric analysis of $Ca(H_2olz)\cdot 2H_2O$ two-dimensional sheets. First weight loss event corresponds to loss of one water molecule, which is followed by loss of the second water molecule and material decomposition.

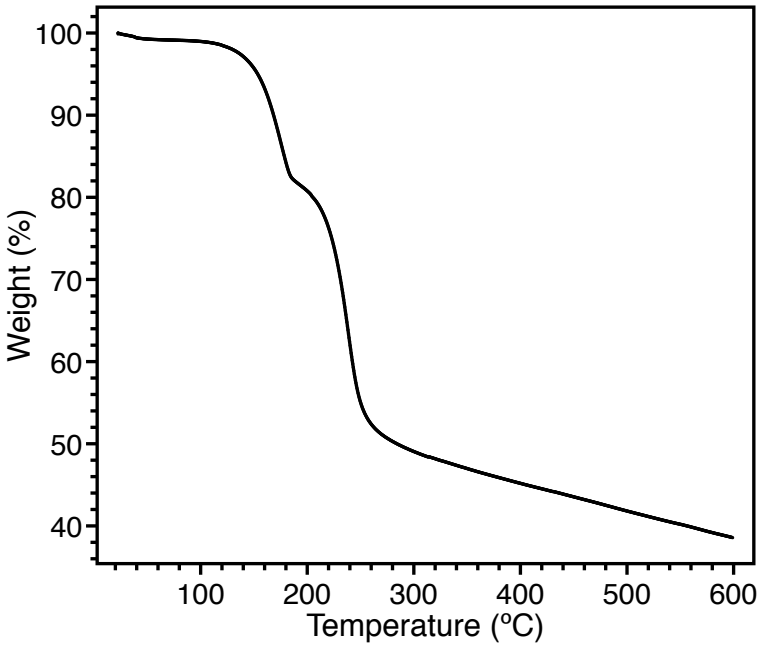

Figure 3.S9. Thermogravimetric analysis of $Ca(H_2olz)\cdot 2DMF$. First weight loss event corresponds to loss of two DMF molecules, which is followed by material decomposition.

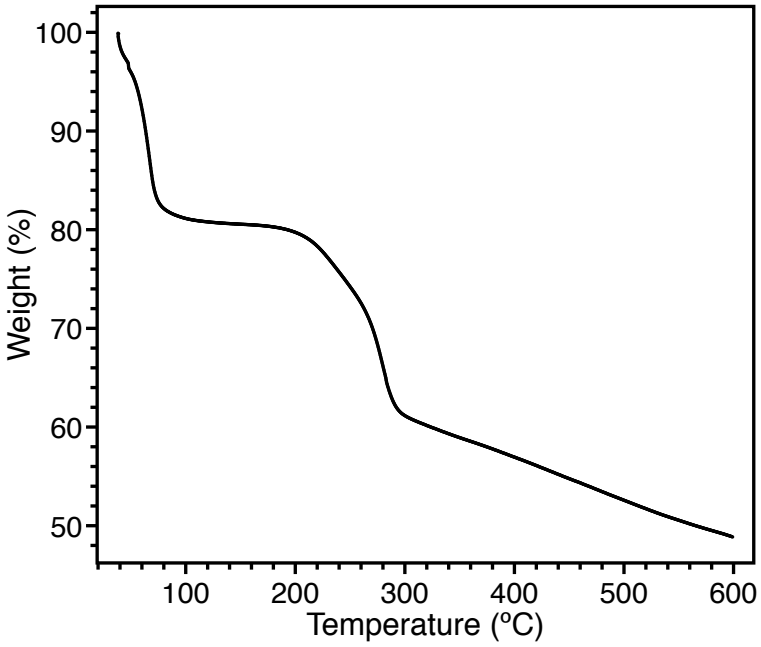

Figure 3.S10. Thermogravimetric analysis of $Ca(H_2olz)\cdot 2MeOH\cdot H_2O$.

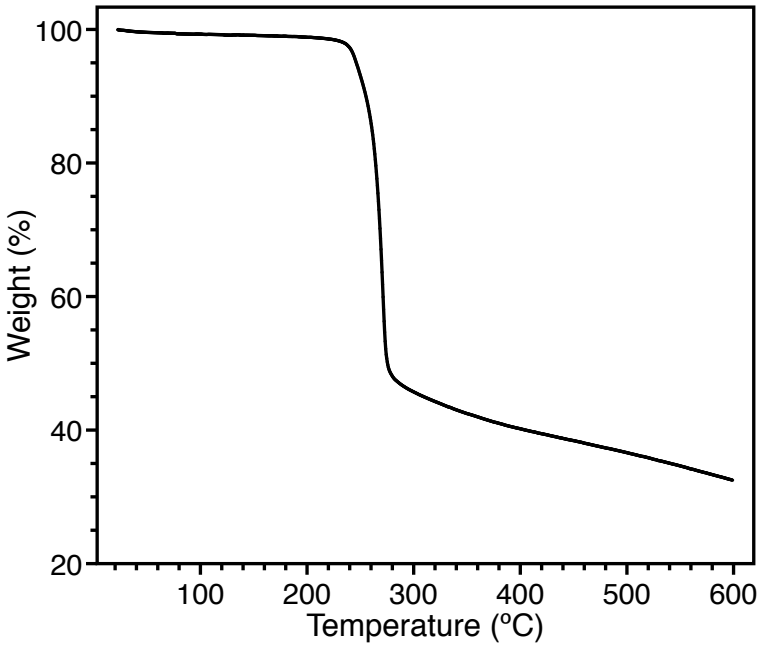

Figure 3.S11. Thermogravimetric analysis of $Ca(H_2olz)$ after immersion of DMF solvate in 100 mM HCl for 24 h. The single weight loss event at high temperature is consistent with decomposition, confirming that the material has no bound solvent in the pores.

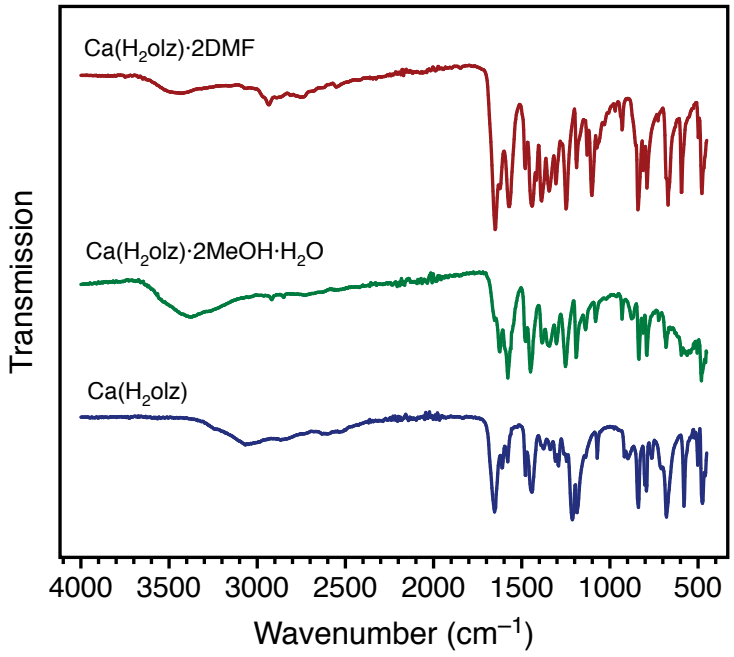

Figure 3.S12. FTIR spectra of three-dimensional $Ca(H_2olz)$ derivatives. From top: $Ca(H_2olz)\cdot 2DMF$, $Ca(H_2olz)\cdot 2MeOH\cdot H_2O$, and $Ca(H_2olz)$.

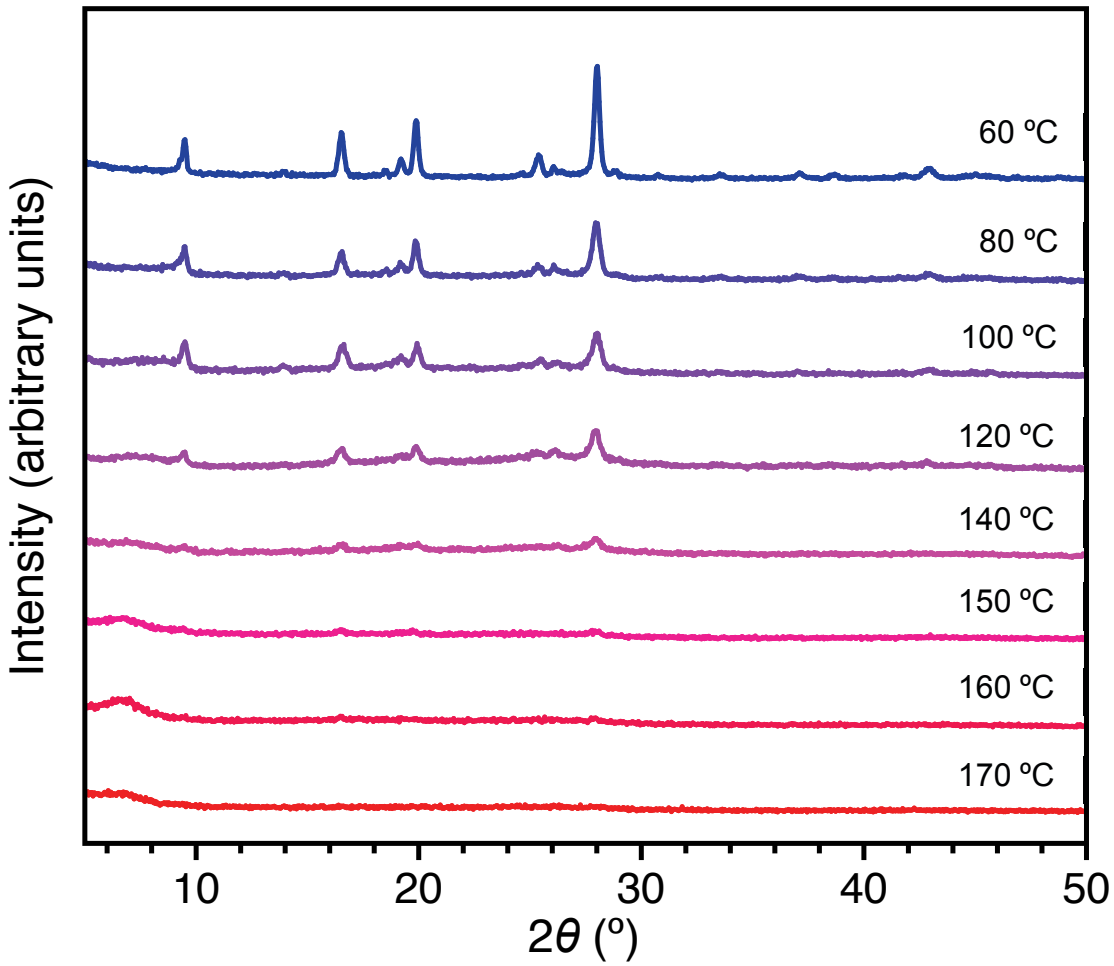

Figure 3.S13. Effects of heating on $Ca(H_2olz)\cdot 2MeOH\cdot H_2O$ crystallinity. The sample of $Ca(H_2olz)\cdot 2MeOH\cdot H_2O$ was heated at the indicated temperature under nitrogen for one hour, and the powder pattern was then collected in air. The sample was then placed back under nitrogen, with subsequent powder patterns measured in air. The exposure of the sample to air after desolvation results in a progressive loss of crystallinity and the sample changes from yellow to maroon to black. However, crystallinity of the material was regained after immersion of the amorphous sample in coordinating solvents like MeCN, MeOH, EtOH, H_2O, DMF. This was also achieved by vapor diffusion with these solvents, suggesting the connectivity remained the same during heating with loss of local order as the pores collapsed into different conformations across the material.

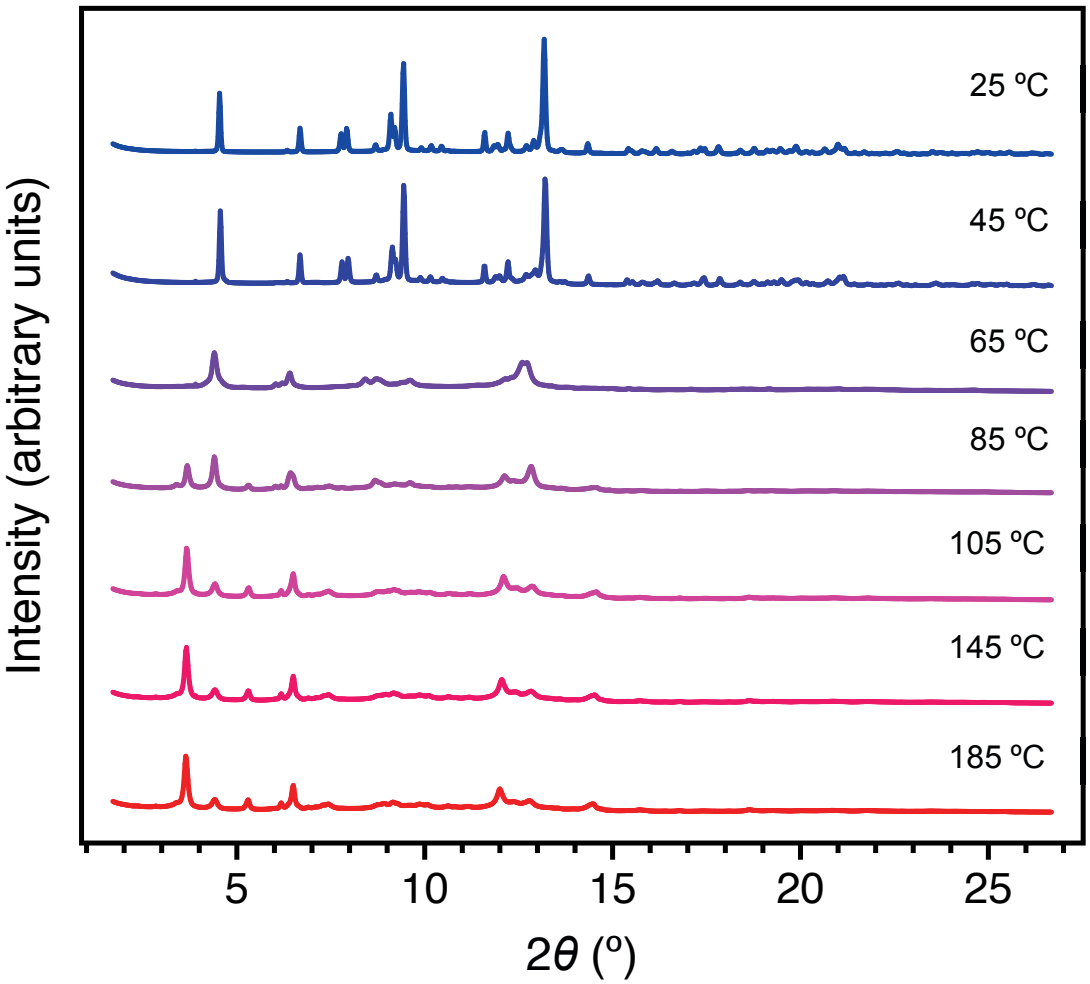

Figure 3.S14. Effects of heating on $Ca(H_2olz)\cdot 2MeOH\cdot H_2O$ crystallinity. The sample of $Ca(H_2olz)\cdot 2MeOH\cdot H_2O$ was heated at the indicated temperature under nitrogen flow at increasing temperatures in a glass capillary at APS. The material undergoes several phase transitions upon heating and changes from yellow to maroon in color, however, only the low temperature phase could be resolved structurally. Porosity of the framework after activation at 65 ºC and 100 ºC was probed by N_2 and H_2, but the isotherms did not show any uptake up to 1 bar. Perhaps at very high pressures, the framework could flex to accommodate gas binding.

Chapter 4: Porous Olsalazine-Based Metal-Organic Frameworks with Open Metal Sites as Platforms for Strong Hydrogen Adsorption and Drug Delivery

4.1 Introduction

Metal-organic frameworks (MOFs) are an important class of materials whose high internal surface areas and tunable pore environments make them useful for a variety of applications including gas sorption,[1-3] catalysis,[4,5] and drug delivery.[6-8] A series of isoreticular frameworks known collectively as MOF-74 are made from dicationic metals and 2,5-dioxido-1,4-benzenedicarboxylate (dobdc^{4-}) and feature hexagonal pores with coordinatively unsaturated open metal sites at the vertices (Figure 4.1a).[9-13] The pore size of these frameworks can also be expanded by using analogous ligands, such as 4,4′-dioxido-3,3′-biphenyldicarboxylate (dobpdc^{4-}), that preserve the motifs of the parent ligand while varying the distance and positions of the coordinating groups (Figure 4.1b).[14,15] Further variations can be introduced by using structural isomers of the ligands, which can influence the pore environment and the electronics of the open metal sites.[16,17]

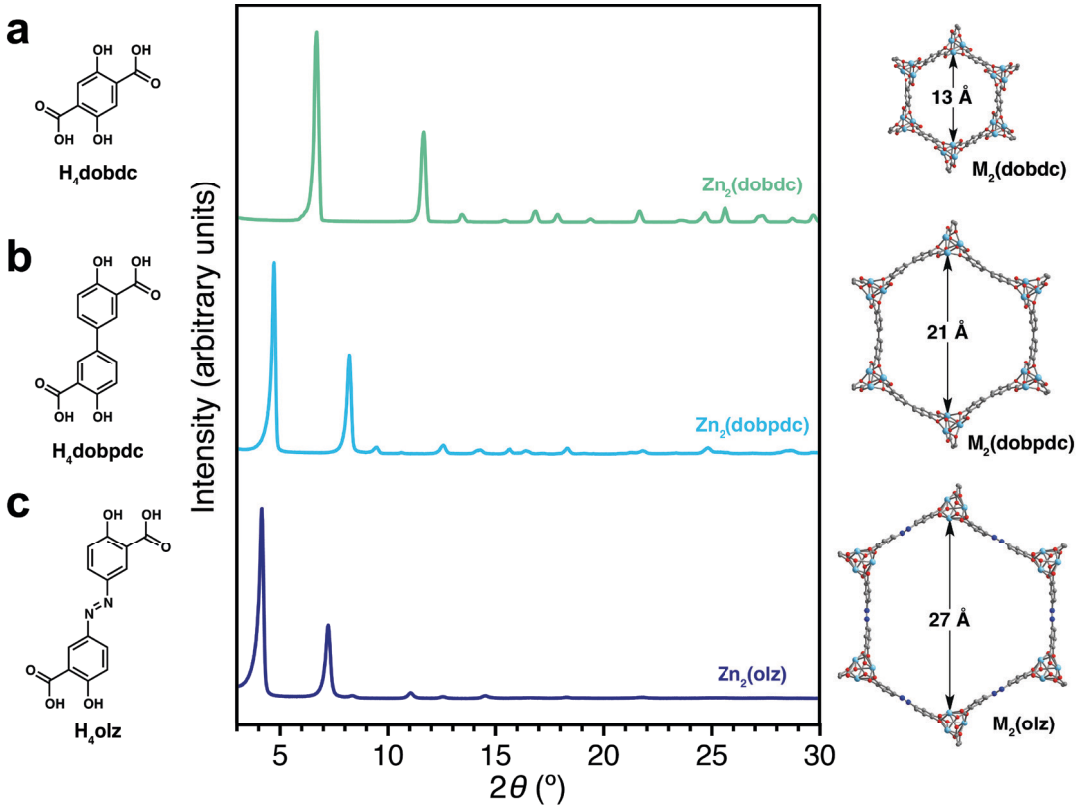

Figure 4.1. Comparison of isoreticular MOF-74 frameworks (a) M_2(dobdc), (b) M_2(dobpdc), and (c) M_2(olz). Left: Structure of protonated ligands. Center: Experimental powder X-ray diffraction patterns of Zn frameworks. Right: Structural representation of frameworks with pore size indicated. Solvent omitted for clarity.

Olsalazine has a number of properties that make it an interesting candidate ligand for expansion of MOF-74. Due to its azo bridge, olsalazine is slightly longer than the dobpdc ligand, allowing it to accommodate larger guest molecules in the expanded pore of the framework. Olsalazine is also effectively nontoxic,[18] which is an advantage for materials in most applications. In this study, a new family of expanded MOF-74 materials were synthesized with olsalazine to form M_2(olz), where M = Mg, Fe, Co, Ni, and Zn (Figure 4.1c). These materials can be activated and exhibit high surface areas and strong hydrogen adsorption, which has been studied by gas sorption studies and infrared spectroscopy.

Olsalazine is itself a prodrug of the anti-inflammatory 5-aminosalicylic acid used in the treatment of ulcerative colitis;[19] it has also been shown to inhibit development of colorectal cancer.[20-22] The compound is often taken as daily multi-gram doses,[23,24] so large doses are tolerated. The low toxicity of olsalazine makes these frameworks amenable to various applications in medicine, as the large pores can accommodate drug cargo and the linker itself is also therapeutic. Furthermore, these frameworks are also biodegradable under physiological conditions, making them viable materials for drug delivery applications. A particularly interesting possibility is to graft a drug with a donating group to the open metal site of the MOF to alter the rate of drug release. We demonstrate this application by using Mg_2(olz) to encapsulate phenethylamine (PEA), a model drug that represents a wide class of bioactive compounds. We observe gradual release of PEA in conjunction with release of olsalazine, suggesting that the PEA release is occurring through diffusion through the pores prior to degradation of the framework.

With large internal pore volumes and highly accessible open-metal sites, this new series of M_2(olz) frameworks form a family of low-toxicity MOFs with capabilities for gas storage and drug delivery applications.

4.2 Experimental

4.2.1 Chemicals

All reagents and solvents were obtained from commercial sources at reagent-grade purity or higher. Solvents include *N,N*-dimethylformamide (DMF), *N,N*-diethylformamide (DEF), *N,N*-dimethylacetamide (DMA), methanol (MeOH), and ethanol (EtOH). Olsalazine acid was synthesized as described is Chapter 3.

4.2.2 Physical Characterization Methods

Laboratory powder X-ray diffraction patterns were collected on a Bruker AXS D8 Advance diffractometer equipped with Cu Kα radiation (λ = 1.5418 Å), a Göbel mirror, a Lynxeye linear position-sensitive detector, and mounting the following optics: fixed divergence slit (0.6 mm), receiving slit (3 mm) and secondary-beam Soller slits (2.5°). The generator was set at 40 kV and 40 mA. Thermogravimetric analysis was carried out at a ramp rate of 2 °C/min under nitrogen flow with a TA Instruments Q5000. ^{1}H NMR spectroscopy was performed on a Bruker Avance III NMR spectrometer equipped with a BBO broadband probe operating at 600.13 MHz. Elemental analyses for C, H and N were performed at the Microanalytical Laboratory of the University of California, Berkeley.

4.2.3 Synthesis of Mg_2(olz)

The metal salt $Mg(NO_3)_2 \cdot 6H_2O$ (242 mg, 0.945 mmol) was dissolved in 12 mL of EtOH and olsalazine acid (136 mg, 0.450 mmol) was dissolved in 18 of DMF. These solutions were combined in a 50-mL Pyrex glass jar and left to heat in an isothermal oven at 120 °C for 1 d. The reaction mixture was decanted, and the yellow powder was washed 3× in DMF at 80 °C and 3× in methanol at 60 °C. The slurry was then transferred to a preweighed analysis tube where excess solvent was removed via cannula. The MOF was activated under argon flow at 180 °C for 12 h and then activated under vacuum on an ASAP 2420 instrument at the same temperature. Activated yield: 125 mg (80% based on ligand). EA: calcd. C 48.5%, H 1.70%, N 8.10%; found C 48.4%, H 1.55%, N 7.94%.

4.2.4 Synthesis of Fe_2(olz)

In a nitrogen filled glove box, a 20-mL vial was charged with olsalazine acid (30 mg, 0.10 mmol) and $FeCl_2$ (30 mg, 0.25 mmol). Methanol (5 mL) and DMF (5 mL) were added and the vial was sealed and stirred until a homogeneous solution formed. The vial was placed on a dry bath preheated to 100 °C and kept at this temperature, without stirring, for 16 hours. The dark red/brown precipitate was collected by filtration, washed with a small amount of MeOH, then placed in a vial with fresh DMF (15 mL) and heated to 100 °C for 8 h. The DMF washes were repeated two more times and were followed by five 8-hour methanol (15 mL) washes at 60 °C. After the final wash, the dark red/brown solid was collected by filtration and dried under vacuum to give $Fe_2(olz)(MeOH)_2$ (46 mg, 97% yield). Activation conditions: In a glove box, $Fe_2(olz)(MeOH)_2$ was placed in a pre-weighed glass ASAP tube equipped with a Transeal. The tube was removed from the box and heated under vacuum to 120 °C at a rate of 0.2 °C/min for 1 week to give Fe_2(olz). EA: calcd. C 41.00%, H 1.50%, N 6.80%; found C 40.70%, H 1.18%, N 6.53%.

4.2.5 Synthesis of Co_2(olz)

The metal salt $Co(NO_3)_2 \cdot 6H_2O$ (72.8 mg, 0.250 mmol) was dissolved in 3.3 mL of ethanol and 3.3 mL of water, and olsalazine acid (30.2 mg, 0.100 mmol) was dissolved in 3.3 mL of DEF. These solutions were combined in a 10-mL Pyrex glass jar and left to heat in an isothermal oven at 100 °C for 1 day. The reaction mixture was decanted, and the orange powder was washed 3× in DMF at 80 °C and 3× in methanol at 60 °C. The slurry was then transferred to a preweighed analysis tube where excess solvent was removed via cannula. The MOF was activated under argon flow at 180 °C for 12 h and then activated under vacuum at the same temperature on an ASAP 2420 instrument. Activated yield: 125 mg (62% based on ligand). EA: calcd. C 40.40%, H 1.50%, N 6.70%; found C 40.13%, H 1.32%, N 6.84%.

4.2.6 Synthesis of Ni_2(olz)

The metal salt $Ni(NO_3)_2 \cdot 6H_2O$ (218 mg, 0.750 mmol) was dissolved in 10 mL of EtOH and 10 mL of H_2O, and olsalazine acid (90.7 mg, 0.300 mmol) was dissolved in 10 mL of DEF. These solutions were combined and then split into three 20-mL glass scintillation vials and left to heat in a dry bath at 100 °C for 1 d. The reaction mixture was decanted, and the orange powder was washed 3× in DMF at 80 ºC and 3× in methanol at 60 °C. The slurry was then transferred to a preweighed analysis tube where the excess solvent was removed via cannula. The MOF was activated under argon flow at 180 °C for 12 h and then activated under vacuum at the same temperature on an ASAP 2420 instrument.

Activated yield: 59.6 mg (62% based on ligand). EA: calcd. C 40.50%, H 1.50%, N 6.70%; found C 40.58%, H 1.69%, N 6.53%.

4.2.7 Synthesis of Zn_2(olz)

The metal salt $Zn(NO_3)_2 \cdot 6H_2O$ (298 mg, 1.00 mmol) was dissolved in 20 mL EtOH and olsalazine acid (121 mg, 0.400 mmol) was dissolved in 20 mL DMA. These solutions were combined and then split into four 20-mL glass scintillation vials and left to heat in dry bath at 100 °C for 1 d. The reaction mixture was decanted, and the yellow powder was washed 3× in DMF at 80 °C and 3× in methanol at 60 °C. The slurry was then transferred to a preweighed analysis tube where excess solvent was removed. The MOF was activated under argon flow at 100 °C for 12 h and then activated under vacuum at the same temperature on an ASAP 2420 instrument. Activated yield: 90.0 mg (52% based on ligand). EA: calcd. C 39.20%, H 1.40%, N 6.50%; found C 38.15%, H 1.34%, N 6.82%.

4.2.8 Gas Adsorption Measurements

Gas adsorption isotherms for pressures in the range 0–1.2 bar were measured using a volumetric method using either a Micromeritics ASAP2020 or ASAP2420 instrument. Samples were transferred under a dinitrogen or argon atmosphere to preweighed analysis tubes, then capped with a Transeal. The samples were evacuated at elevated temperature until the outgas rate was <1 μbar/min, at which point the tube was weighed to determine the mass of the activated sample. The tube was transferred to the analysis port of the instrument and the outgas rate was again checked to ensure that it was <1 μbar/min. UHP-grade (99.999% purity) N_2, H_2, CO_2, and He were used for all adsorption measurements. For all isotherms, warm and cold free spaces were measured using He; N_2, and H_2 isotherms at 77 and 87 K were measured in liquid nitrogen and liquid argon baths, respectively. CO_2 isotherms at 25, 35, and 45 °C were measured in a circulating water bath. Oil-free vacuum pumps and oil-free pressure regulators were used for all measurements. BET surface areas were calculated from the linear region of the N_2 isotherms at 77 K prior to the step at 0.1 bar, and Langmuir surface areas were determined using Micromeritics software.

4.2.9 Powder X-ray Diffraction

High-resolution X-ray powder diffraction patterns of the samples were collected at the beamline 17-BM at the Advanced Photon Source (Argonne National Laboratory) with an average wavelength of 0.72768 Å. Scattered intensity was recorded by Perkin Elmer a-Si Flat Panel detector at room temperature. Prior to measurement, the samples were sealed in borosilicate glass capillaries of 1 mm diameter under N_2 or Ar (Hilgenberg glass No. 50). The powder data analysis (pattern indexing, profile fitting, crystal structure solution and refinement) was performed with the program TOPAS 4.1.[25] A model of the M_2(olz) structure was derived using Materials Studio.

4.2.10 Infrared Spectroscopy

Activated MOF powder (~10 mg) was loaded into a cup attached to a copper slab providing thermal contact to a coldfinger cryostat (Janis ST-300T), which was monitored by a Si-diode thermometer. The cup was then mounted in a custom-built sample chamber, which allowed DRIFTS experiments to be performed under a controlled atmosphere. A calibrated gas manifold was used to dose the sample chamber with known

quantities of H_2 gas. Infrared spectra were acquired under different pressures of H_2 using a Bomem DA3Michelson interferometer equipped with a glowbar source, CaF_2 beamsplitter, and a liquid nitrogen cooled mercury-cadmium-telluride detector. A cutoff filter above 9000 cm^{-1} was used to prevent unwanted sample heating from the IR source.

4.2.11 Loading of Phenethylamine in $Mg_2(olz)$

A 20% solution of phenethylamine in DCM (500 µL) was sparged under N_2 and added to 6.5 mg of activated $Mg_2(olz)$ in a vial under a nitrogen atmosphere, and the sample was left undisturbed for 24 h. The product was washed copiously with fresh DCM and collected on a funnel to obtain $Mg_2(olz)(PEA)_2$ as an orange-yellow solid (Yield: 10.7 mg, 97%). To confirm stoichiometry, ~1 mg of material was digested in a 10% DCl solution in d_6-DMSO and placed in an NMR tube. A ratio of 1:2 olsalazine to phenethylamine was observed by ^1H NMR, confirming one PEA per open metal site.

4.2.12 Preparation of $Mg(olz)(PEA)_2$ Pellets

Pellets were prepared from all materials using a circular die with a 4 mm diameter and pressed in a vise for 15 min under a consistent pressure. All pellets had a mass of 5.0 mg (± 0.2 mg) and an approximate thickness of 0.35 mm.

4.2.13 Drug Release from $Mg_2(olz)(PEA)_2$

The drug release studies were performed under simulated physiological conditions (PBS, pH 7). Dissolution was observed for three 5.0 mg (± 0.2 mg) pellets each in 50 mL conical tubes containing 25 mL of PBS; the tubes were placed horizontally in a shaking incubator with bidimensional stirring at 60 rpm at 37 °C. 100 µL aliquots were collected at every designated time point and filtered through a 0.45 µm filter. Samples were stored at room temperature prior to analysis.

4.2.14 Quantification of Drug Release by HPLC

Release of phenethylamine and olsalazine from the material was monitored by reversed-phase HPLC. The Agilent 1260 Infinity Series HPLC was equipped with a quaternary pump, diode array detector, and a Zorbax C18 column using a gradient of 50 to 75% MeCN/H_2O (both with 0.05% TFA) at 1 mL/min and a 30 µL sample injection volume. Solvents were filtered using a Millipore 0.2 µm nylon membrane. The peak area measured at full dissolution was normalized to 100% released and used to correlate observed peak intensity to percent release at each time point. Phenethylamine and olsalazine were monitored at 210 and 360 nm, respectively.

4.3 Results and Discussion

4.3.1 Synthesis and Structure of $M_2(olz)$ Frameworks

The $M_2(olz)$ frameworks can be synthesized by heating a solution of metal(II) halide or metal(II) nitrate salts and olsalazine acid in a mixture of DMF, DEF, or DMA with EtOH or MeOH. The synthesis is fairly robust and can tolerate some variability in the synthetic conditions, which can be optimized for each metal to improve crystallinity (Figure 4.2). The frameworks are all isostructural under the same solvation conditions as observed by powder X-ray diffraction (Figure 4.3).

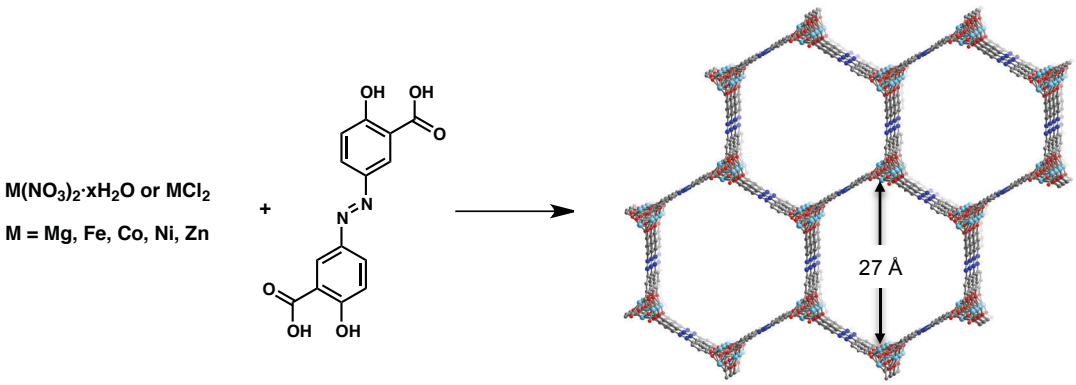

Figure 4.2. Synthetic scheme for M_2(olz) with structural model viewed down *c*-axis (solvent not shown). Cyan, gray, red, and blue spheres correspond to metal, carbon, oxygen, and nitrogen atoms, respectively.

Many attempts were made to vary synthetic conditions to grow large crystals for structure determination. However, the thin needle-shaped crystals did not diffract sufficiently for single crystal X-ray diffraction (crystallite size and morphology are shown in Figure 4S.1). Despite these issues, we have been able to model the structure of the frameworks by using high resolution powder patterns of solvated and activated M_2(olz). Severe preferred orientation of the crystallites limited the information obtained along the *c*-axis, but with the similarities to other analogs of MOF-74 such as M_2(dobpdc),[14] we have been able to show that the connectivity and space group are consistent with what one would predict for M_2(olz). Methanol-solvated frameworks appear to crystallize in the trigonal $P3_321$ space group with the cell parameters: a = 24.88(7) Å, c = 6.49(5) Å (Le Bail refinement plot shown in Figure 4.S2).

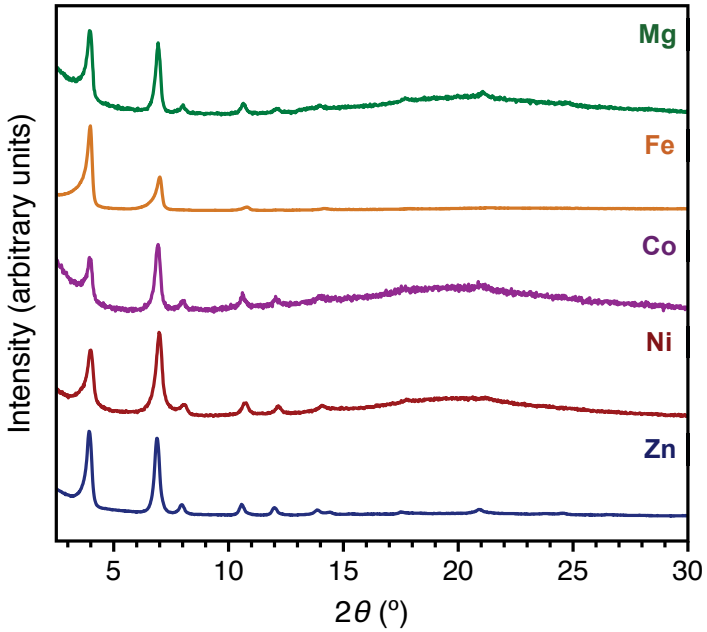

Figure 4.3. Powder X-ray diffraction patterns of DMF-solvated M_2(olz) frameworks (M = Mg, Fe, Co, Ni, Zn).

4.3.2 Nitrogen Adsorption in M_2(olz) Frameworks

Like the isoreticular frameworks in the expanded MOF-74 series, the M_2(olz)$(DMF)_2$ frameworks can undergo solvent exchange in methanol to replace coordinated solvent molecules at the axial position of the octahedral metal. The frameworks can then be activated with heating to remove bound solvent in the pores and produce bare M_2(olz). (Activated powder patterns shown in Figure 4.S3; activation conditions were extrapolated from TGA curves in Figure 4.S4.) N_2 adsorption measurements were performed on all of the M_2(olz) frameworks, and the isotherms are reported in Figure 4.4. With the exception of Zn_2(olz), which collapses upon removal of guest solvent (Figure 4.S5), the M_2(olz) frameworks exhibit high surface areas upon activation consistent with the expanded linker. The isotherms show a step at approximately 0.1 bar N_2, which likely results from the filling of secondary adsorption sites in the large pores. Langmuir and BET surface areas reported in Table 4.1 were calculated from N_2 isotherms at 77 K.

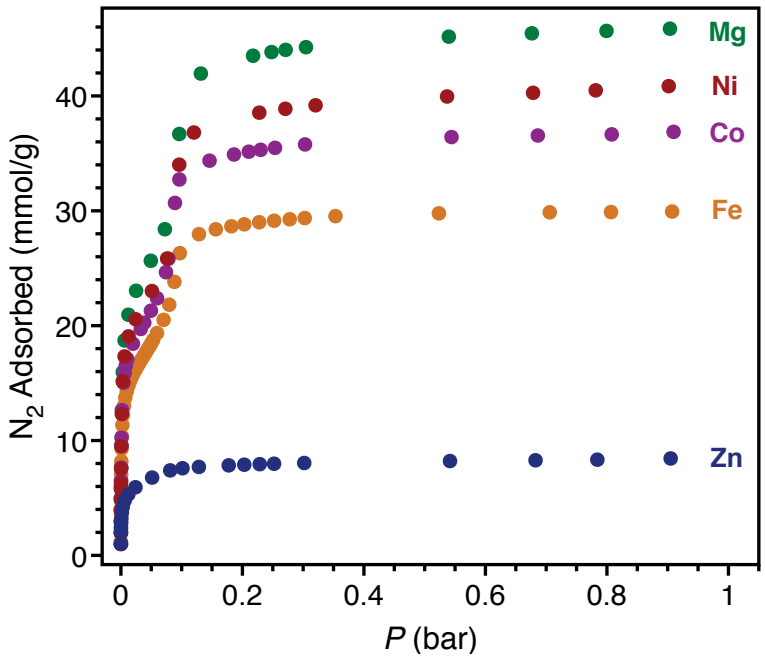

Figure 4.4. Isotherms for the adsorption of N_2 at 77 K in activated M_2(olz) (From top: M = Mg, Ni, Co, Fe, Zn).

Table 4.1. BET and Langmuir surface areas of activated M_2(olz) frameworks.

Metal	BET Surface Area (m^2/g)	Langmuir Surface Area (m^2/g)
Mg	2620	4530
Fe	1680	3000
Co	1980	3630
Ni	2030	4020
Zn	580	770

4.3.3 Hydrogen Adsorption in M_2(olz) Frameworks

In order to demonstrate that the M_2(olz) frameworks have the same connectivity as the expanded MOF-74 structures, we examined the strength of hydrogen binding to the frameworks to confirm the presence of open metal sites upon activation of the framework. In particular, we wanted to prove that activation of the frameworks would generate coordinatively unsaturated open metal sites, which are obtained when an axial solvent molecule like methanol is removed from the octahedral metal to produce a square-pyramidal geometry that is poised to interact with incoming gas molecules.

Isosteric heats of adsorption (Q_{st}) were calculated using the Clausius-Clapeyron relation after fitting H_2 isotherms at 77 and 87 K. Indeed, hydrogen adsorption studies of the activated M_2(olz) frameworks showed strong binding of H_2 for the Mg, Fe, Co, and Ni frameworks with Q_{st} at low coverage of about –11 to –12 kJ/mol (Figure 4.5), which is comparable to the values obtained for Ni_2(*m*-dobdc).[16] The steep rise of adsorbed hydrogen at low pressures is consistent with behavior of open metal sites and shows strong binding of hydrogen at these sites (Figure 4.6). In the case of Zn, however, we do not observe steep uptake of hydrogen due to a collapse of the framework as evidenced by the low surface area and a decrease in crystallinity upon activation. This behavior may result from a change in the coordination geometry of the Zn^{2+} ion where the removal of the axial solvent molecule, coupled with the flexibility of the olsalazine ligand, makes it favorable for five-coordinate Zn^{2+} to rearrange and adopt a lower energy geometry that is coordinatively saturated.

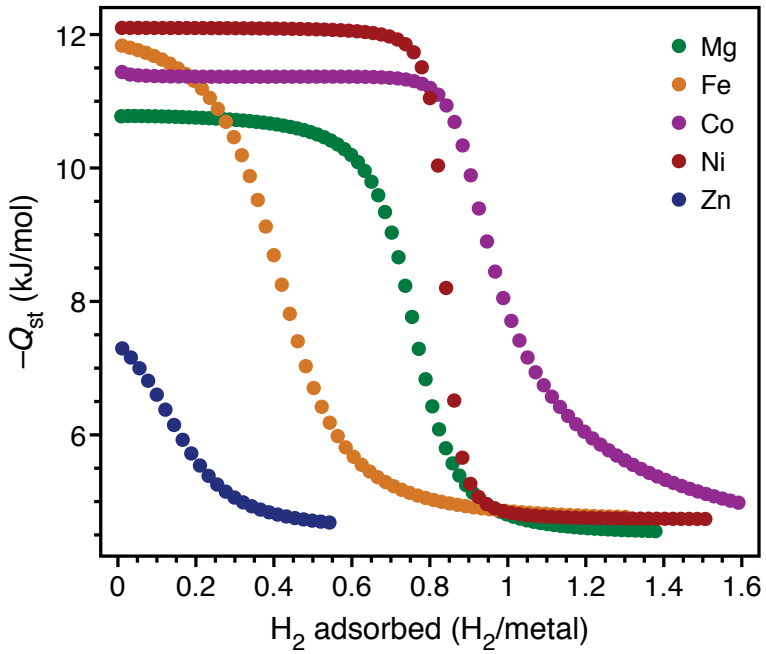

Figure 4.5. H_2 isosteric heat of adsorption curves for the M_2(olz) series of frameworks as a function of the amount adsorbed.

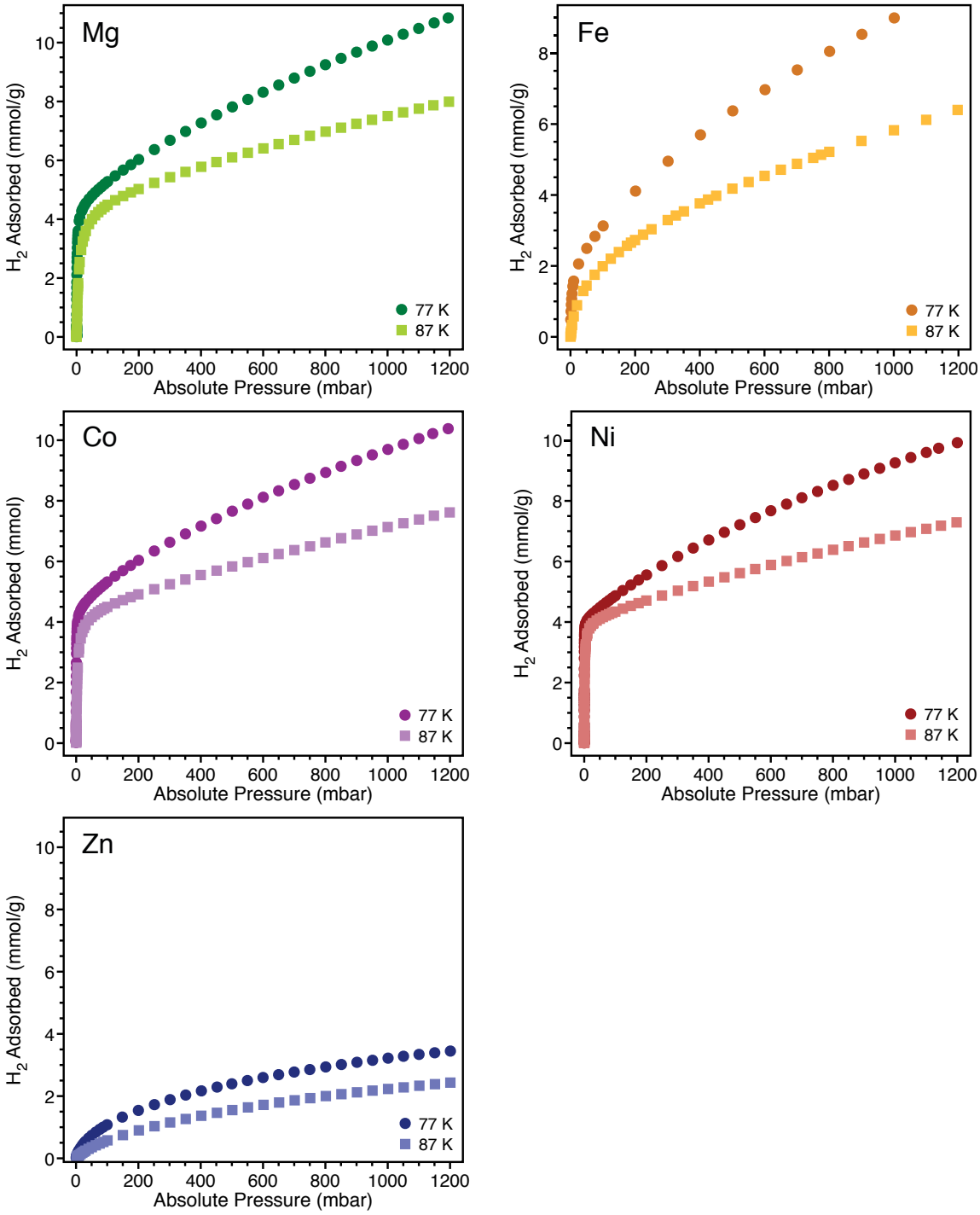

Figure 4.6. H_2 adsorption isotherms at 77 K and 87 K for M_2(olz) frameworks (M = Mg, Fe, Co, Ni, Zn). With the exception of Zn, all M_2(olz) materials show strong adsorption of hydrogen.

4.3.4 Infrared Spectroscopy of H_2 Interaction with M_2(olz) Frameworks

Infrared (IR) spectroscopy was used to probe the nature of the M_2(olz) interaction with hydrogen for the best performing materials, Ni_2(olz) and Mg_2(olz). Due to its molecular symmetry, hydrogen is an IR-inactive molecule in the gas phase. However, when adsorbed at electronically rich surfaces, the symmetry breaks and the molecule becomes IR-active (schematic energy diagram is given in Figure 4S.6). Accordingly, the binding of H_2 at open metal coordination sites in metal-organic frameworks can be probed by IR spectroscopy. The interactions of the adsorbed H_2 with the metal site almost always result in a lowering of its H–H stretching frequency. Recent studies showed a clear correlation between the magnitude of the frequency shift and the binding energy at a particular site in the framework.[26] Figure 4.7 shows a comparison of vibrational frequencies of seven different H_2 loadings for Mg_2(olz) (extended spectral ranges are given in Figure 4S.7). At a loading of one hydrogen molecule per metal, a doublet is observed in the spectrum (from 4100 to 4080 cm^{-1}) that corresponds to the pure vibrational part of *ortho*-H_2 and *para*-H_2 bound to the open metal site. The spectrum of H_2 bound to Ni_2(olz) shows greater frequency shift than that of H_2 bound to Mg_2(olz), which is consistent with the stronger H_2 binding to Ni^{2+} relative to Mg^{2+} (Figure 4S.9). The comparison of the spectra of M_2(olz) and M_2(dobdc) indicates slightly stronger H_2 binding in metal-organic frameworks based upon the $dobdc^{4-}$ linker (Figure 4S.9).

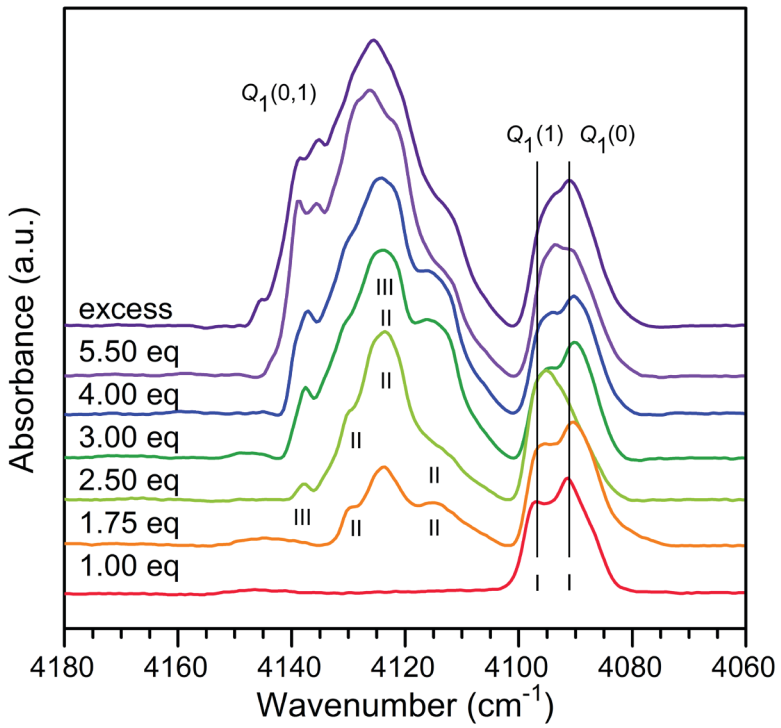

Figure 4.7. H_2 adsorbed at multiple sites as a function of loading. Infrared absorption of H_2 in Mg_2(olz) at 15 K, the equivalent number refers to H_2 molecules per Mg. Q(0) refers to para-H_2 and Q(1) to ortho-H_2.

Increasing H_2 loading beyond one equivalent per metal results in binding at secondary sites, as evidenced by multiple peaks (from 4150 to 4100 cm^{-1}). Similar frequency shifts were observed for the secondary adsorption sites of M_2(dobdc) and M_2(*m*-dobdc) frameworks.[16] Additional increase of loading results in further filling of the channels, thus more complicated spectral features are observed. These results indicate the presence of multiple binding sites within the M_2(olz) metal-organic frameworks.

The enthalpy of adsorption at a particular site can be established by variable-temperature infrared spectroscopy.[27,28] Figure 4.8 presents the spectra of M_2(olz) collected as a function of temperature. In both cases, the initial H_2 loading was set such that only the open metal site was occupied during the measurements and the fractional occupancy was determined by the ratio of the area under the infrared band to that observed at complete saturation. The enthalpy and entropy changes were extracted by the van't Hoff relationship plots, which are presented as insets in Figure 4.8. Note that the slopes extracted from these plots are very sensitive to variation in the maximum saturation area, thus an error of 0.5 kJ/mol can be estimated. For Ni_2(olz) the enthalpy of hydrogen adsorption is $\Delta H° = -12.8(6)$ kJ/mol, which is higher than the $\Delta H° = -9.84(2)$ kJ/mol of Mg_2(olz). These data are consistent with the calculated isosteric heats of adsorption from the H_2 adsorption isotherms. For both frameworks, rather large values of entropy changes are measured ($\Delta S° = -132(2)$ J/K and $\Delta S° = -154(6)$ J/K for Mg_2(olz) and Ni_2(olz) respectively). This is consistent with previous studies, where a strong correlation between the entropy and enthalpy change of bound H_2 was observed.[28]

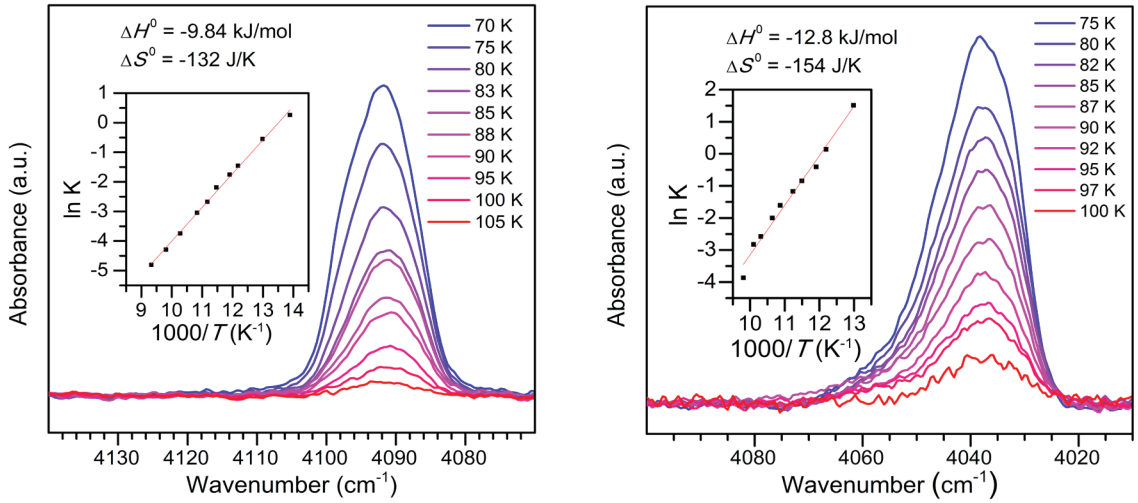

Figure 4.8. Enthalpy and entropy changes upon adsorption of H_2 on the open metal site. Variable-temperature infrared spectra of (a) Mg_2(olz) and (b) Ni_2(olz). The inset shows the van't Hoff plot that is used to extract the enthalpy and entropy change in H_2 upon adsorption to the open metal site.

4.3.5 CO_2 Adsorption in Mg_2(olz)

In order to reduce greenhouse gas emissions from coal-fired power plants, metal-organic frameworks have been shown to be promising materials for capture of carbon dioxide (CO_2) from flue gas. Since Mg is the lightest metal that forms the M_2(olz) materials, the highest gravimetric capacity for CO_2 can be achieved in Mg_2(olz). As such, adsorption of CO_2 was measured in Mg_2(olz) at different temperatures (Figure 4.9). While Mg_2(olz) appears to have lower uptake of CO_2 than Mg_2(dobpdc), the calculated isosteric heats of adsorption suggest that they may perform similarly (Figure 4S.10). Alkylamines such as *N,N′*-dimethylethylenediamine (mmen) have been appended to Mg_2(dobpdc) to enhance CO_2 binding.[14] This is achieved via a concerted mechanism that results in a stepped isotherm where essentially no CO_2 is adsorbed below a given pressure and full coverage is obtained above this step.[15] With the expanded pore geometry of Mg_2(olz), this material may offer opportunities to modulate the pressure at which this step occurs while also accommodating larger and bulkier amines.

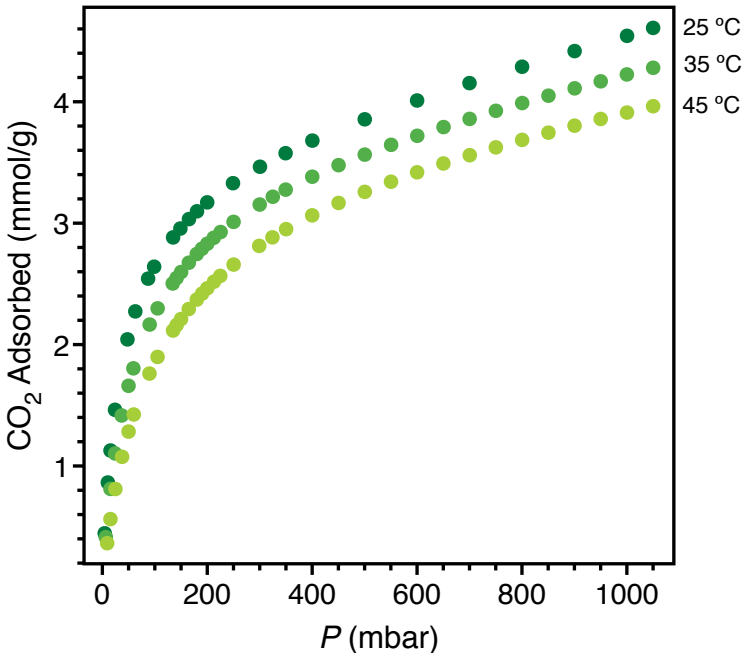

Figure 4.9. Adsorption of CO_2 at varying temperatures in Mg_2(olz).

4.3.6 Drug Loading and Release of Phenethylamine from Mg_2(olz)

The high biocompatibility of the M_2(olz) frameworks makes them promising candidates for drug delivery applications. Several approaches have been employed to load drugs into MOFs including non-covalent drug encapsulation,[29-33] post-synthetic functionalization of the MOF linker,[34] framework amorphization after loading,[35] "ship in a bottle",[36] and "bottle around ship"[37] strategies. An alternative approach is to use the drug as a ligand to bind to open metal sites within a MOF. However, there are few examples that use this approach.[30,38,39] By taking advantage of the coordinatively unsaturated open metal site

and large pore apertures of the M_2(olz) frameworks, we proposed to graft drugs containing a Lewis-basic functional group directly to the metal of the framework. Previous studies have demonstrated grafting of various functional groups, including amines,[14,15,40] alkoxides,[41] phenoxides,[42] and other anions[43] onto the open metal sites of M_2(dobdc), M_2(dobpdc), and MIL-101 frameworks. We therefore wondered if biologically active molecules possessing these functional groups could be similarly coordinated to the open metal sites of a M_2(olz) framework.

Phenethylamine (PEA) was selected as a model drug because this structural motif forms the basis for a large class of bioactive compounds with diverse pharmacological properties. Phenethylamines are employed as stimulants, vasoconstrictors, bronchodilators, appetite suppressants, antidepressants, blood pressure regulators, neuroprotective agents, and anti-Parkinsonian agents (Figure 4.S11). Due to the extensive metabolism and addictive nature of some of these compounds, there is a need for controlled release formulations that reduce dramatic fluctuations in drug concentrations while maintaining adequate therapeutic levels over time. In this way, having a controlled release dosage form may improve performance of the drug while reducing the likelihood of abuse.

Due to the lower atomic weight of Mg and its role as an essential nutritional supplement, Mg_2(olz) was used for the initial drug release studies. The degradation profile of Mg_2(olz) alone is given in Figure 4S.12. PEA was grafted onto activated Mg_2(olz) using a 20% solution of PEA in DCM. After 24 h, the material was washed and the stoichiometry of the material was confirmed as 2 PEA per olsalazine, or one PEA per Mg^{2+}, by ^{1}H NMR spectroscopy (Figure 4S.13). A proposed model for Mg_2(olz)$(PEA)_2$ is depicted in Figure 4.10, where the amine of PEA is coordinated to the Mg^{2+} open metal sites in the observed 1:1 stoichiometry. The secondary amine *N*-methylphenethylamine was also shown to bind to Mg_2(olz) in the expected stoichiometry of one amine per metal, suggesting that Mg_2(olz) is a versatile platform that could accommodate a variety of phenethylamine derivatives (Figure 4S.14).

In order to simulate physiological conditions for drug release, the Mg_2(olz)$(PEA)_2$ material was pressed into pellets, which were immersed in a neutral pH phosphate buffered saline (PBS) solution with shaking at 37 °C. Aliquots were taken at regular time points until the material was fully dissolved, and release of both PEA and olsalazine was quantified by reversed-phase HPLC (Figure 4.10). Based on the observed cumulative release, the internal PEA is released more rapidly than the olsalazine linker. For comparison, about 95% of PEA has been released at the 3 h mark, while only 50% of olsalazine has been released at this point. This difference in release rates suggests that the coordinated PEA is likely being displaced as water diffuses into the one-dimensional channels prior to the dissolution of the framework itself. In future embodiments, we may consider varying the particle size of the MOF to change the grain boundaries between particles and alter the rates of water diffusion into the material.

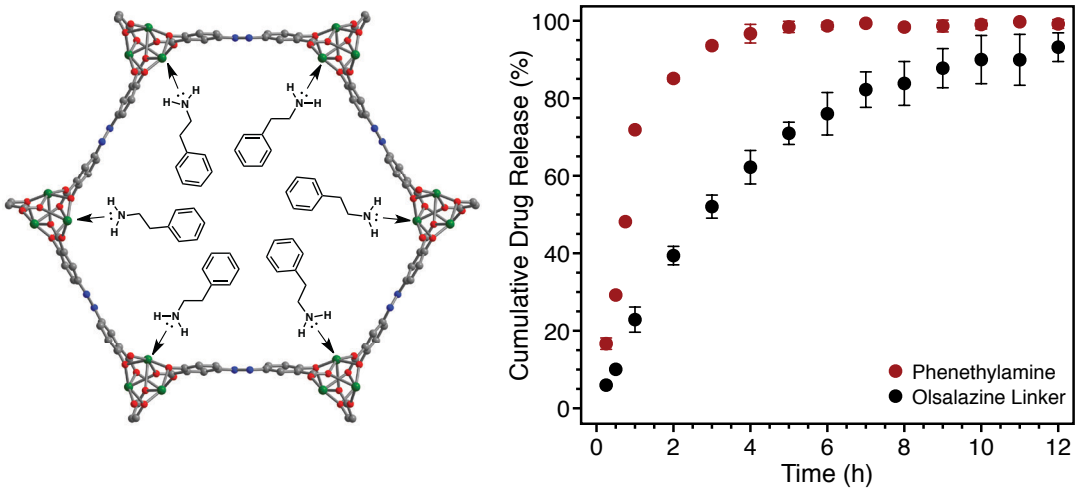

Figure 4.10. Left: Proposed binding of model drug phenethylamine to open metal sites of $Mg_2(olz)$ framework. Right: Release of phenethylamine and olsalazine from $Mg_2(olz)(PEA)_2$ under simulated biological conditions (PBS, pH 7.4, 37 °C). Error bars represent standard deviation for release from triplicate pellet samples.

4.4 Conclusions

We have synthesized and characterized a new family of $M_2(olz)$ metal-organic frameworks, where M = Mg, Fe, Co, Ni, and Zn. These materials exhibit very high surface areas and possess coordinatively unsaturated open metal sites that can be accessed by heating the materials under vacuum. The sites have a strong affinity for hydrogen, as demonstrated by hydrogen adsorption studies and infrared spectroscopy. The lightest $Mg_2(olz)$ framework, which is an expanded analog of $Mg_2(dobpdc)$, was also evaluated for CO_2 adsorption at various temperatures. It has similar adsorption properties and stability as bare $Mg_2(dobpdc)$, making $Mg_2(olz)$ a promising alternative whose larger pores may be used to accommodate larger amines for optimization of CO_2 adsorption.

$Mg_2(olz)$ was also used to demonstrate that these highly biocompatible materials can serve as attractive platforms for drug delivery applications. Phenethylamine was used as a model drug to illustrate the capabilities of the material for both drug loading and release. Through judicious choice of metal, one can envision tailoring the interaction between framework and drug to alter the strength of binding and optimize the rate of release. For instance, the $Mg_2(olz)$ and $Co_2(olz)$ frameworks would be well suited for strong interactions with hard nitrogen and oxygen donors while the $Zn_2(olz)$ framework would be well matched for softer sulfur-based drugs. Additionally, the $Fe_2(olz)$ framework could be oxidized to $[Fe_2(olz)]^{2-}$ as has been done for $Fe_2(dobdc)$[38] and $Fe_2(dobpdc)$,[43] thereby producing a cationic framework capable of strong binding to anionic drugs.

In summary, this family of low-toxicity $M_2(olz)$ frameworks serves as a useful platform for diverse applications including gas storage and drug delivery.

4.5 Acknowledgements

I would like to thank T. Runcevski, J. Oktawiec, and J. A. Mason for powder diffraction data collection and analysis, T. Runcevski and H. Z. H. Jiang for infrared spectroscopy measurements with S. A. FitzGerald, M. T. Kapelewski and D. A. Reed for fitting hydrogen isotherm data, B. K. Keitz for CO_2 isotherm measurements and synthesis of Fe_2(olz), K. E. Colwell for SEM studies, and J. R. Long for support. I would also like to thank J. Truong for assistance with HPLC measurements. We thank the 11-BM staff at the Advanced Photon Source at Argonne National Laboratory for assisting with powder X-ray diffraction experiments. Use of the Advanced Photon Source at Argonne National Laboratory was supported by the U.S. Department of Energy, Office of Science, Office of Basic Energy Sciences, under contract no. DE-AC02-06CH11357.

4.6 References

(1) Sumida, K., Rogow, D. L., Mason, J. A., McDonald, T. M., Bloch, E. D., Herm, Z. R., Bae, T.-H., and Long, J. R. (2012) Carbon dioxide capture in metal-organic frameworks. *Chem. Rev. 112*, 724–781.
(2) Herm, Z. R., Bloch, E. D., and Long, J. R. (2013) Hydrocarbon separations in metal–organic frameworks. *Chem. Mater. 26*, 323–338.
(3) Mason, J. A., Veenstra, M., and Long, J. R. (2014) Evaluating metal–organic frameworks for natural gas storage. *Chem. Sci. 5*, 32–51.
(4) Corma, A., Garcia, H., and Llabrés i Xamena, F. X. (2010) Engineering metal organic frameworks for heterogeneous catalysis. *Chem. Rev. 110*, 4606–4655.
(5) Chughtai, A. H., Ahmad, N., Younus, H. A., Laypkov, A., and Verpoort, F. (2015) Metal–organic frameworks: versatile heterogeneous catalysts for efficient catalytic organic transformations. *Chem. Soc. Rev. 44*, 6804–6849.
(6) Rocca, Della, J., Liu, D., and Lin, W. (2011) Nanoscale metal–organic frameworks for biomedical imaging and drug delivery. *Acc. Chem. Res. 44*, 957–968.
(7) Horcajada, P., Gref, R., Baati, T., Maurin, G., Couvreur, P., Férey, G., Morris, R. E., and Serre, C. (2012) Metal–organic frameworks in biomedicine. *Chem. Rev. 112*, 1232–1268.
(8) Sun, C.-Y., Qin, C., Wang, X.-L., and Su, Z.-M. (2013) Metal-organic frameworks as potential drug delivery systems. *Expert Opin. Drug Deliv. 10*, 89–101.
(9) Dietzel, P. D. C., Morita, Y., Blom, R., and Fjellvåg, H. (2005) An in situ high-temperature single-crystal investigation of a dehydrated metal–organic framework compound and field-induced magnetization of one-dimensional metal–oxygen chains. *Angew. Chem. 117*, 6512–6516.
(10) Rosi, N. L., Kim, J., Eddaoudi, M., Chen, B., O'Keeffe, M., and Yaghi, O. M. (2005) Rod packings and metal-organic frameworks constructed from rod-shaped secondary building units. *J. Am. Chem. Soc. 127*, 1504–1518.
(11) Dietzel, P. D. C., Panella, B., Hirscher, M., Blom, R., and Fjellvåg, H. (2006) Hydrogen adsorption in a nickel based coordination polymer with open metal sites in the cylindrical cavities of the desolvated framework. *Chem. Commun. 0*, 959–961.

(12) Caskey, S. R., Wong-Foy, A. G., and Matzger, A. J. (2008) Dramatic tuning of carbon dioxide uptake via metal substitution in a coordination polymer with cylindrical pores. *J. Am. Chem. Soc. 130*, 10870–10871.
(13) Bloch, E. D., Murray, L. J., Queen, W. L., Chavan, S., Maximoff, S. N., Bigi, J. P., Krishna, R., Peterson, V. K., Grandjean, F., Long, G. J., Smit, B., Bordiga, S., Brown, C. M., and Long, J. R. (2011) Selective binding of O_2 over N_2 in a redox-active metal-organic framework with open iron(II) coordination sites. *J. Am. Chem. Soc. 133*, 14814–14822.
(14) McDonald, T. M., Lee, W. R., Mason, J. A., Wiers, B. M., Hong, C. S., and Long, J. R. (2012) Capture of carbon dioxide from air and flue gas in the alkylamine-appended metal-organic framework mmen-Mg_2(dobpdc). *J. Am. Chem. Soc. 134*, 7056–7065.
(15) McDonald, T. M., Mason, J. A., Kong, X., Bloch, E. D., Gygi, D., Dani, A., Crocellà, V., Giordanino, F., Odoh, S. O., Drisdell, W. S., Vlaisavljevich, B., Dzubak, A. L., Poloni, R., Schnell, S. K., Planas, N., Lee, K., Pascal, T., Wan, L. F., Prendergast, D., Neaton, J. B., Smit, B., Kortright, J. B., Gagliardi, L., Bordiga, S., Reimer, J. A., and Long, J. R. (2015) Cooperative insertion of CO_2 in diamine-appended metal-organic frameworks. *Nature 519*, 303–308.
(16) Kapelewski, M. T., Geier, S. J., Hudson, M. R., Stück, D., Mason, J. A., Nelson, J. N., Xiao, D. J., Hulvey, Z., Gilmour, E., FitzGerald, S. A., Head-Gordon, M., Brown, C. M., and Long, J. R. (2014) M_2(*m*-dobdc) (M = Mg, Mn, Fe, Co, Ni) metal-organic frameworks exhibiting increased charge density and enhanced H_2 binding at the open metal sites. *J. Am. Chem. Soc. 136*, 12119–12129.
(17) Deng, H., Grunder, S., Cordova, K. E., Valente, C., Furukawa, H., Hmadeh, M., Gándara, F., Whalley, A. C., Liu, Z., Asahina, S., Kazumori, H., O'Keeffe, M., Terasaki, O., Stoddart, J. F., and Yaghi, O. M. (2012) Large-pore apertures in a series of metal-organic frameworks. *Science 336*, 1018–1023.
(18) Campbell, D. E. S., and Berglindh, T. (1988) Pharmacology of olsalazine. *Scand. J. Gastroenterol. 23*, 7–12.
(19) Selby, W. S., Barr, G. D., Ireland, A., Mason, C. H., and Jewell, D. P. (1985) Olsalazine in active ulcerative colitis. *BMJ (Clinical research ed.) 291*, 1373–1375.
(20) Brown, W. A., Farmer, K. C., Skinner, S. A., Malcontenti-Wilson, C., Misajon, A., and O'Brien, P. E. (2000) 5-aminosalicyclic acid and olsalazine inhibit tumor growth in a rodent model of colorectal cancer. *Dig. Dis. Sci. 45*, 1578–1584.
(21) Eaden, J. (2003) Review article: the data supporting a role for aminosalicylates in the chemoprevention of colorectal cancer in patients with inflammatory bowel disease. *Aliment. Pharmacol. Ther. 18*, 15–21.
(22) Herfarth, H. (2012) The role of chemoprevention of colorectal cancer with 5-aminosalicylates in ulcerative colitis. *Dig. Dis. 30*, 55–59.
(23) Courtney, M. G., Nunes, D. P., Bergin, C. F., O'Driscoll, M., Trimble, V., Keeling, P. W., and Weir, D. G. (1992) Randomised comparison of olsalazine and mesalazine in prevention of relapses in ulcerative colitis. *Lancet 339*, 1279–1281.
(24) Kles, K. A., Vavricka, S. R., Turner, J. R., Musch, M. W., Hanauer, S. B., and Chang, E. B. (2005) Comparative analysis of the in vitro prosecretory effects of balsalazide, sulfasalazine, olsalazine, and mesalamine in rabbit distal ileum. *Inflamm. Bowel Dis. 11*, 253–257.
(25) Bruker AXS. (2007) TOPAS-Academic, Version 4.1.

(26) FitzGerald, S. A., Burkholder, B., Friedman, M., Hopkins, J. B., Pierce, C. J., Schloss, J. M., Thompson, B., and Rowsell, J. L. C. (2011) Metal-specific interactions of H_2 adsorbed within isostructural metal-organic frameworks. *J. Am. Chem. Soc. 133*, 20310–20318.
(27) Garrone, E., Bonelli, B., and Otero Areán, C. (2008) Enthalpy–entropy correlation for hydrogen adsorption on zeolites. *Chem. Phys. Lett. 456*, 68–70.
(28) Areán, C. O., Chavan, S., Cabello, C. P., Garrone, E., and Palomino, G. T. (2010) Thermodynamics of hydrogen adsorption on metal-organic frameworks. *ChemPhysChem 11*, 3237–3242.
(29) Horcajada, P., Serre, C., Vallet-Regí, M., Sebban, M., Taulelle, F., and Férey, G. (2006) Metal–organic frameworks as efficient materials for drug delivery. *Angew. Chem. 118*, 6120–6124.
(30) Horcajada, P., Chalati, T., Serre, C., Gillet, B., Sebrie, C., Baati, T., Eubank, J. F., Heurtaux, D., Clayette, P., Kreuz, C., Chang, J.-S., Hwang, Y. K., Marsaud, V., Bories, P.-N., Cynober, L., Gil, S., Férey, G., Couvreur, P., and Gref, R. (2009) Porous metal-organic-framework nanoscale carriers as a potential platform for drug delivery and imaging. *Nat. Mater. 9*, 172–178.
(31) Wang, H.-N., Meng, X., Yang, G.-S., Wang, X.-L., Shao, K.-Z., Su, Z.-M., and Wang, C.-G. (2011) Stepwise assembly of metal-organic framework based on a metal-organic polyhedron precursor for drug delivery. *Chem. Commun. 47*, 7128–7130.
(32) Sun, C.-Y., Qin, C., Wang, C.-G., Su, Z.-M., Wang, S., Wang, X.-L., Yang, G.-S., Shao, K.-Z., Lan, Y.-Q., and Wang, E.-B. (2011) Chiral nanoporous metal-organic frameworks with high porosity as materials for drug delivery. *Adv. Mater. Weinheim 23*, 5629–5632.
(33) Zhuang, J., Kuo, C.-H., Chou, L.-Y., Liu, D.-Y., Weerapana, E., and Tsung, C.-K. (2014) Optimized metal-organic-framework nanospheres for drug delivery: evaluation of small-molecule encapsulation. *ACS Nano. 8*, 2812–2819.
(34) Taylor-Pashow, K. M. L., Rocca, Della, J., Xie, Z., Tran, S., and Lin, W. (2009) Postsynthetic modifications of iron-carboxylate nanoscale metal-organic frameworks for imaging and drug delivery. *J. Am. Chem. Soc. 131*, 14261–14263.
(35) Orellana-Tavra, C., Baxter, E. F., Tian, T., Bennett, T. D., Slater, N. K. H., Cheetham, A. K., and Fairen-Jimenez, D. (2015) Amorphous metal-organic frameworks for drug delivery. *Chem. Commun. 51*, 13878–13881.
(36) di Nunzio, M. R., Agostoni, V., Cohen, B., Gref, R., and Douhal, A. (2014) A "ship in a bottle" strategy to load a hydrophilic anticancer drug in porous metal organic framework nanoparticles: Efficient encapsulation, matrix stabilization, and photodelivery. *J. Med. Chem. 57*, 411–420.
(37) Liédana, N., Galve, A., Rubio, C., Téllez, C., and Coronas, J. (2012) CAF@ZIF-8: One-Step Encapsulation of Caffeine in MOF. *ACS Appl. Mater. Interfaces 4*, 5016–5021.
(38) Hu, Q., Yu, J., Liu, M., Liu, A., Dou, Z., and Yang, Y. (2014) A low cytotoxic cationic metal-organic framework carrier for controllable drug release. *J. Med. Chem. 57*, 5679–5685.
(39) Bloch, E. D., Queen, W. L., Chavan, S., Wheatley, P. S., Zadrozny, J. M., Morris, R., Brown, C. M., Lamberti, C., Bordiga, S., and Long, J. R. (2015) Gradual release of strongly bound nitric oxide from $Fe_2(NO)_2$(dobdc). *J. Am. Chem. Soc. 137*, 3466–3469.

(40) Nguyen, H. G. T., Weston, M. H., Farha, O. K., Hupp, J. T., and Nguyen, S. T. (2012) A catalytically active vanadyl(catecholate)-decorated metal organic framework via post-synthesis modifications. *CrystEngComm 14*, 4115–5.
(41) Wiers, B. M., Foo, M.-L., Balsara, N. P., and Long, J. R. (2011) A solid lithium electrolyte via addition of lithium isopropoxide to a metal-organic framework with open metal sites. *J. Am. Chem. Soc. 133*, 14522–14525.
(42) Aubrey, M. L., Ameloot, R., Wiers, B. M., and Long, J. R. (2014) Metal–organic frameworks as solid magnesium electrolytes. *Energy Environ. Sci. 7*, 667–671.
(43) Aubrey, M. L., and Long, J. R. (2015) A dual-ion battery cathode via oxidative insertion of anions in a metal-organic framework. *J. Am. Chem. Soc. 137*, 13594–13602.

4.7 Supplementary Information

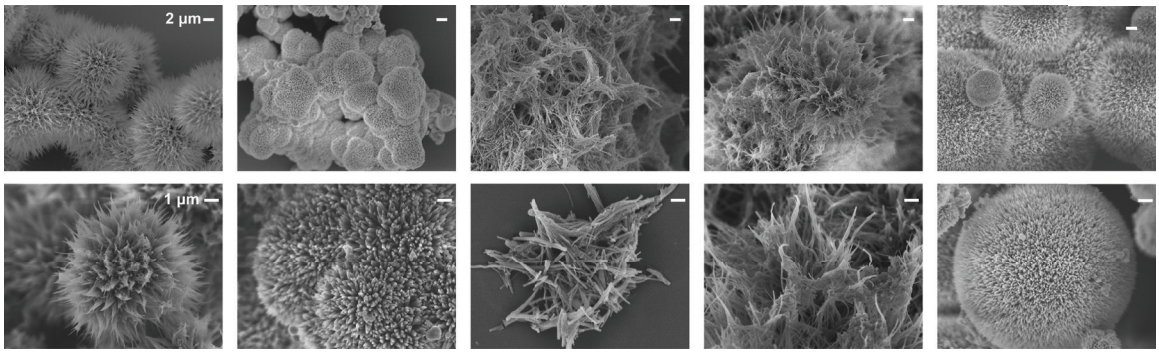

Figure 4.S1. Scanning electron microscopy images of M_2(olz) crystallites (from left to right: Mg, Fe, Co, Ni, Zn). SEM images were taken using a JEOL JSM-6340F SEM. Samples were suspended in methanol and drop cast onto a silicon chip. To dissipate charge, the samples were sputter coated with approximately 3 nm of Au (Denton Vacuum).

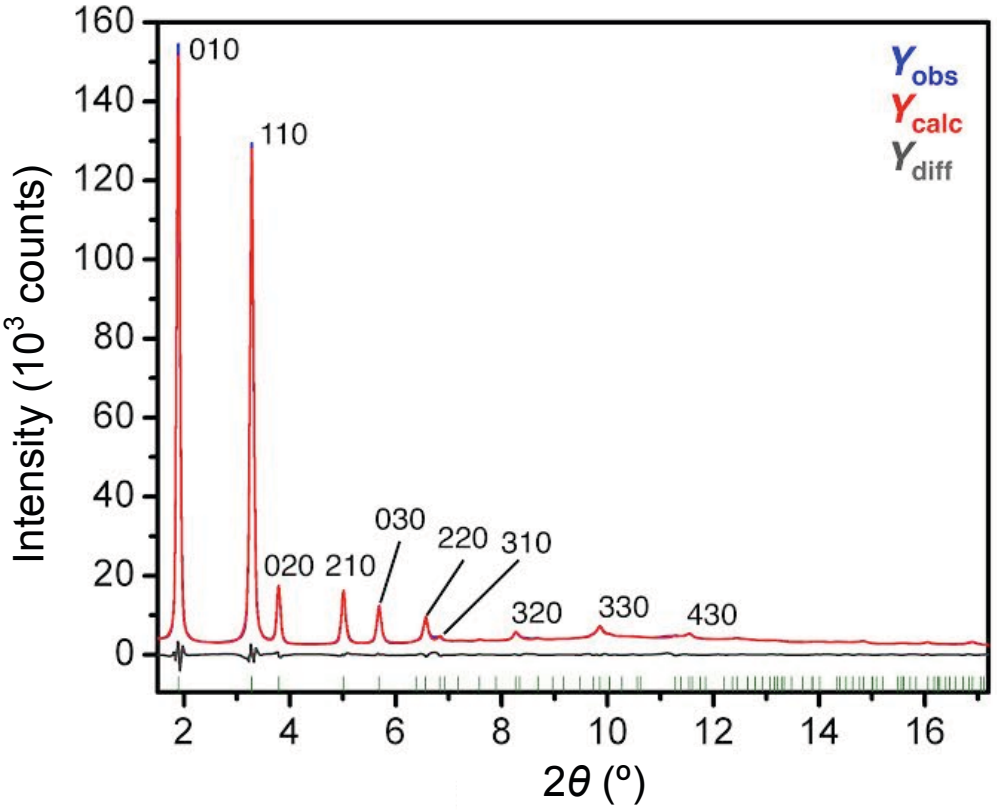

Figure 4.S2. Plot of the Le Bail refinement for MeOH-solvated Zn_2(olz) (λ = 0.41397 Å) showing the observed (blue) and calculated (red) powder diffraction patterns and the difference (grey). The indicated reflections show the lack of structural information available for the *c*-axis.

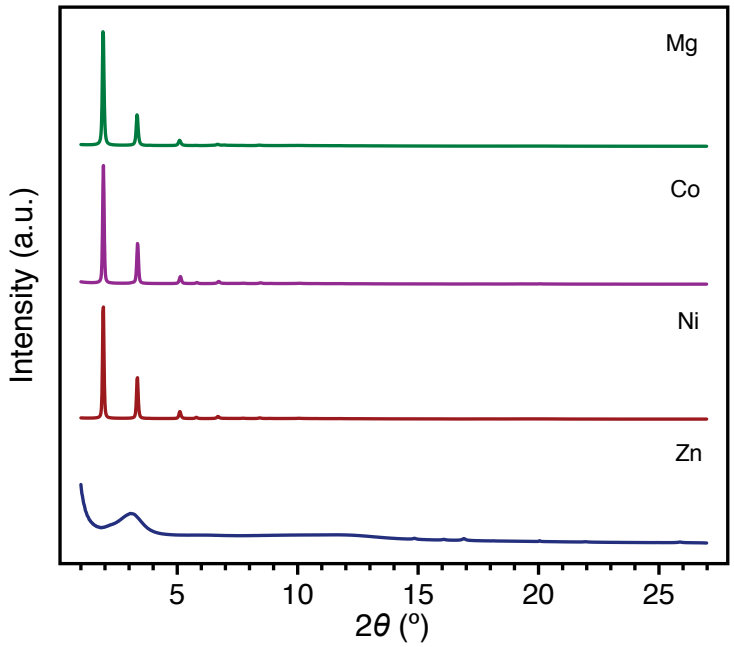

Figure 4.S3. Powder X-ray diffraction patterns of activated M_2(olz) frameworks (λ = 0.72768 Å). Loss of crystallinity for Zn upon heating is consistent with the lower surface area and low hydrogen uptake observed.

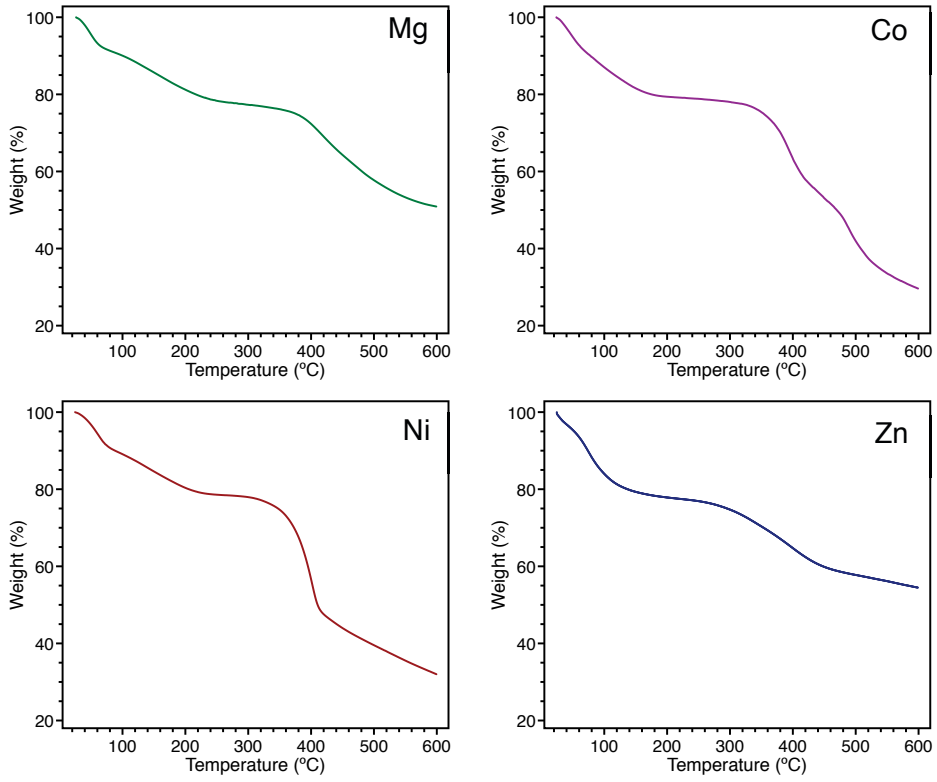

Figure 4.S4. Thermogravimetric analysis (TGA) of air-stable methanol-solvated M_2(olz) frameworks. Data collected with a ramp rate of 2 °C/min.

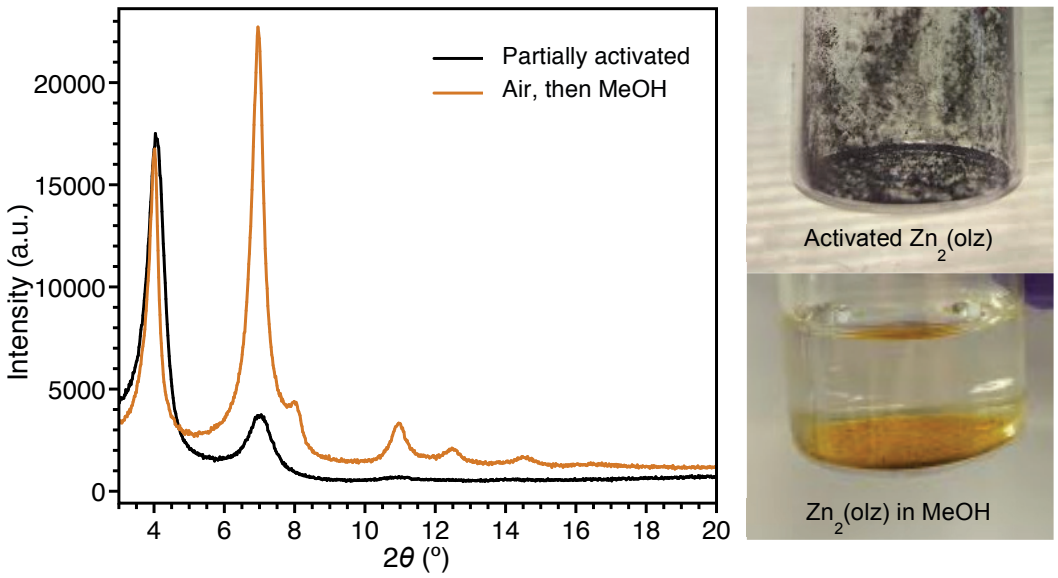

Figure 4.S5. Decreased crystallinity of Zn_2(olz) after partial activation at 65 °C is regained after exposure to methanol by powder X-ray diffraction (λ = 1.5418 Å). This behavior is suggestive of framework collapse upon desolvation, resulting in loss of long-range order. When re-immersed in a coordinating solvent such as methanol, crystallinity is restored.

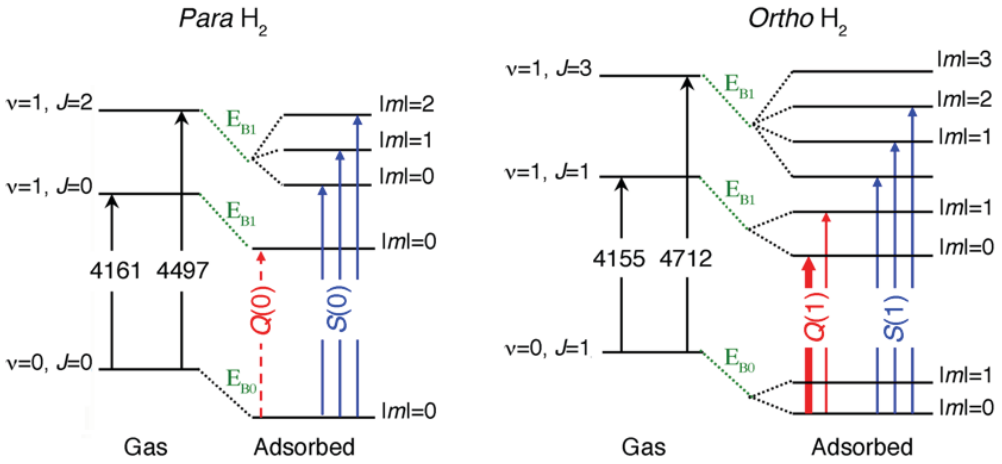

Figure 4.S6. Energy diagram of molecular hydrogen explaining the vibrational transitions observed in metal-organic frameworks. While gas phase H_2 is not observed by IR spectroscopy, the polarization of the molecule upon interaction with a metal cation results in transitions from the vibrational ground state (v = 0) to the first excited state (v = 1) for *para* and *ortho*-H_2. J is the rotational quantum number. The values indicate gas phase transition frequency in cm^{-1}. Dashed vertical arrows indicate transitions that are activated by the overlap mechanism, solid arrows indicate the quadrupole mechanism, and the transition marked with the thick arrow is activated by both. E_{B0} and E_{B1} are the binding energies in the ground state and vibrationally excited states, respectively.

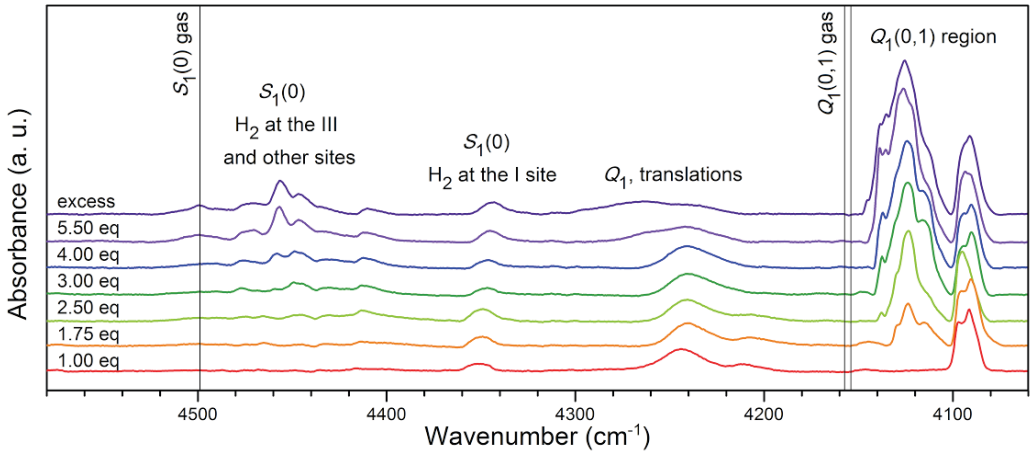

Figure 4.S7. H_2 adsorbed at multiple binding sites as a function of loading in Mg_2(olz). IR absorption of H_2 at 15 K, the equivalent number refers to H_2 molecules per Mg. The vertical lines show the H_2 gas phase wavenumber values for vibration (Q) and vibration-rotation (S) excitations. Q_{trans} refers to the center-of-mass motion of the adsorbed H_2. Q(0) and S(0) refer to *para*-H_2 and Q(1) to *ortho*-H_2. Subscript 1 indicates fundamental transition in which the vibrational quantum number increases by one.

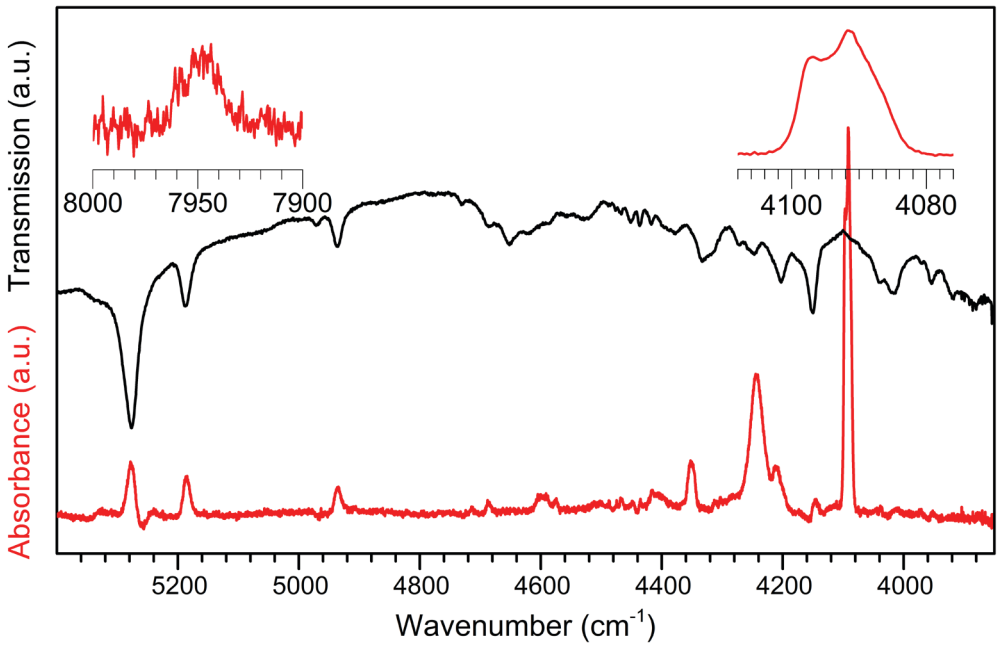

Figure 4.S8. H_2 adsorbed at an open metal site. Curve in red: absorbance at 15 K for one H_2 per Mg relative to activated sample of Mg_2(olz). Insets: overtone and fundamental stretching vibrations of H_2, showing peaks of both *ortho* and *para* hydrogen. Curve in black: Raw IR signal for activated Mg_2(olz) sample at 15 K.

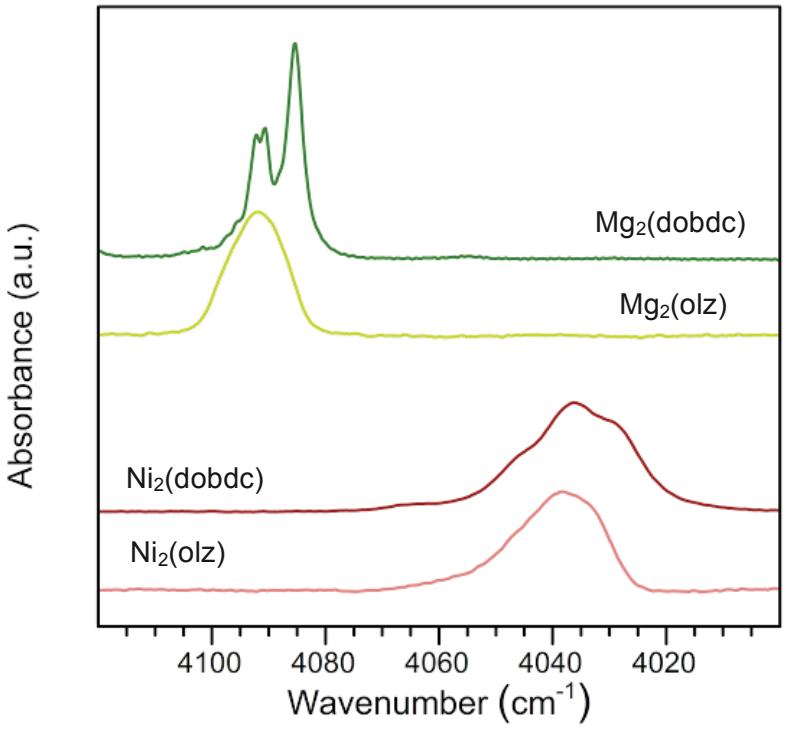

Figure 4.S9. Infrared spectroscopy of H_2 adsorbed at an open metal site. Absorbance at 77 K for one H_2 per metal cation relative to activated samples of Mg_2(dobdc), Mg_2(olz), Ni_2(dobdc), and Ni_2(olz) (dobdc^{4-} = 2,5-dioxido-1,4-benzenedicarboxylate). The similar wavenumber values for the stretching vibrations of H_2 adsorbed at frameworks composed of the same metal but different organic linker indicate similar local environment around the metal center. The observed redshifts of the peaks in the spectra of the nickel frameworks as compared to the peaks in spectra of the magnesium frameworks indicate that H_2 is more strongly bound to the nickel open metal sites (confirmed by the calculated entropy and enthalpy changes upon adsorption). According to the small redshifts in the spectra of the dobdc as compared to olz analogues, H_2 adsorbs only slightly stronger to the dobdc frameworks as compared to the olz frameworks.

Langmuir-Freundlich Fits for Calculation of Isosteric Heats of Adsorption

The dual-site Langmuir−Freundlich expression (Equation 4.S1) was used to fit the combined isotherm data at 77 K and 87 K for Mg_2(olz), Fe_2(olz), Ni_2(olz), and Zn_2(olz). The tri-site Langmuir expression (Equation 4.S2) was used to fit the data for Co_2(olz), where n is the amount of gas adsorbed (mmol/g), q_{sat} is the saturation loading for site 1, 2, or 3 (mmol/g), b is the Langmuir parameter associated with either site 1, 2, or 3 (bar^{-v}), p is the pressure, and v is a constant. The value for b is calculated per Equation 4.S3.

$$n = \frac{q_{sat,1} b_1 p^{v_1}}{1 + b_1 p^{v_1}} + \frac{q_{sat,2} b_2 p^{v_2}}{1 + b_2 p^{v_2}} \qquad \text{Equation 4.S1}$$

$$n = \frac{q_{sat,1} b_1 p^{v_1}}{1 + b_1 p^{v_1}} + \frac{q_{sat,2} b_2 p^{v_2}}{1 + b_2 p^{v_2}} + \frac{q_{sat,3} b_3 p^{v_3}}{1 + b_3 p^{v_3}} \qquad \text{Equation 4.S2}$$

$$b_i = e^{-S_i} e^{E_i \cdot 1000/RT} \qquad \text{Equation 4.S3}$$

The equation was fit using the statistical software package of OriginPro 8. The quality of fits was determined by comparing the adjusted R^2 and residual sum of squares values, as well as by visual inspection. Wolfram Mathematica 7 was then used to create a series of data points corresponding to points on the fit curve. The isosteric heat of adsorption Q_{st} was then calculated using the data points from Mathematica for both the 77 K and 87 K isotherms using the Clausius-Clapeyron relation (Equation 4.S4) at equivalent loadings (n, mmol/g). Q_{st} is the isosteric heat of adsorption (kJ/mol), R is the gas constant (L*bar/[mol*K]), and P is the pressure at a given n at either T_2 (87 K) or T_1 (77 K).

$$Q_{st} = -\frac{R\left[\ln(P_{T_2}) - \ln(P_{T_2})\right]}{T_2^{-1} - T_1^{-1}} \qquad \text{Equation 4.S4}$$

Table 4.S1. Langmuir fit parameters for the H_2 isotherms of M_2(olz) shown in Figure 4.6.

	Mg_2(olz)	Fe_2(olz)	Co_2(olz)	Ni_2(olz)	Zn_2(olz)
$q_{sat,1}$ (mmol/g)	4.36	2.09	4.19	4.04	0.74
S_1 (R)	9.57	13.44	10.28	9.96	8.86
E_1 (kJ/mol)	10.29	12.17	11.63	12.10	8.04
v_1	0.95	1	1.03	1	1
$q_{sat,2}$ (mmol/g)	29.14	16.63	20.49	14.06	4.72
S_2 (R)	7.46	7.69	6.94	7.92	7.01
E_2 (kJ/mol)	3.88	4.69	3.62	4.73	4.56
v_2	0.86	1	0.97	1	1
$q_{sat,3}$ (mmol/g)	–	–	1.53	–	–
S_3 (R)	–	–	16.38	–	–
E_3 (kJ/mol)	–	–	11.05	–	–
v_3	–	–	0.62	–	–

Table 4.S2. Dual-site Langmuir-Freundlich parameters for the CO_2 adsorption isotherms of Mg_2(olz) at 25, 35, and 45 °C.

	25 °C	35 °C	45 °C
$q_{sat,1}$ (mmol/g)	3.48	3.23	2.95
b_1 (bar^{-1})	21.37	16.45	13.31
v_1	0.921	0.946	0.987
$q_{sat,2}$ (mmol/g)	28.95	4.57	3.53
b_2 (bar^{-1})	0.0441	0.345	0.492
v_2	0.915	0.980	1.02

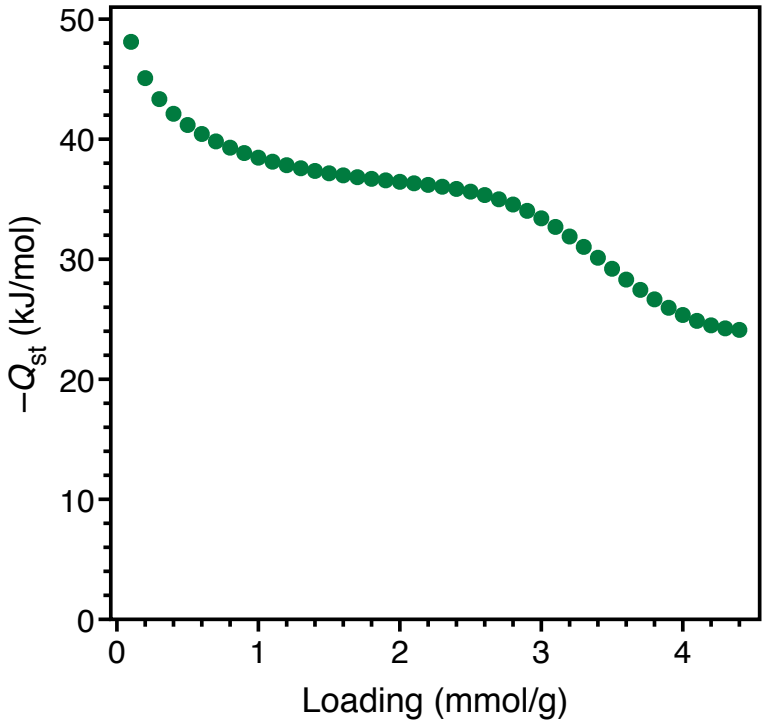

Figure 4.S10. Isosteric heats of adsorption ($-Q_{st}$) as a function of loading for CO_2 in Mg_2(olz).

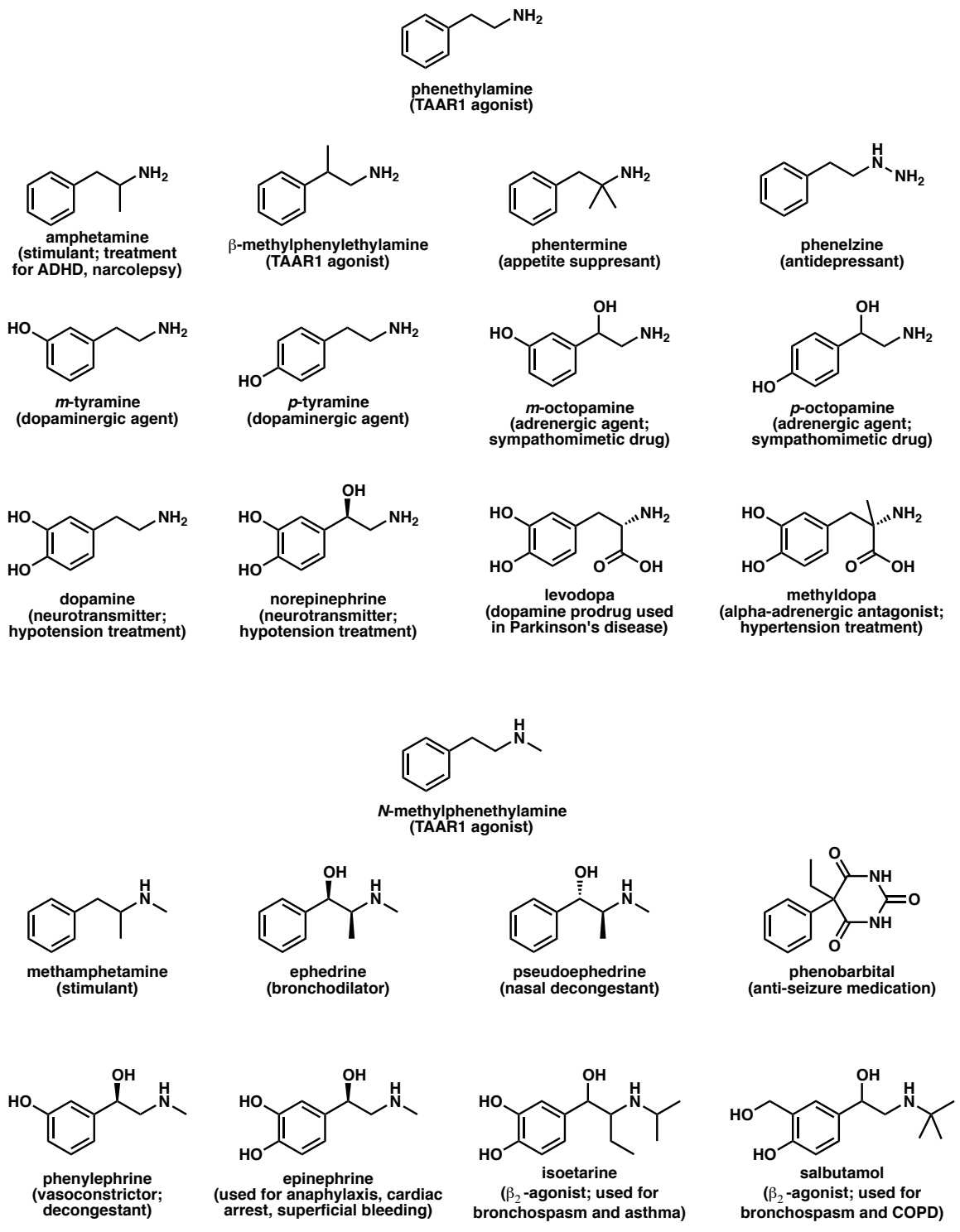

Figure 4.S11. A selection of primary and secondary phenethylamine derivatives of pharmaceutical importance.

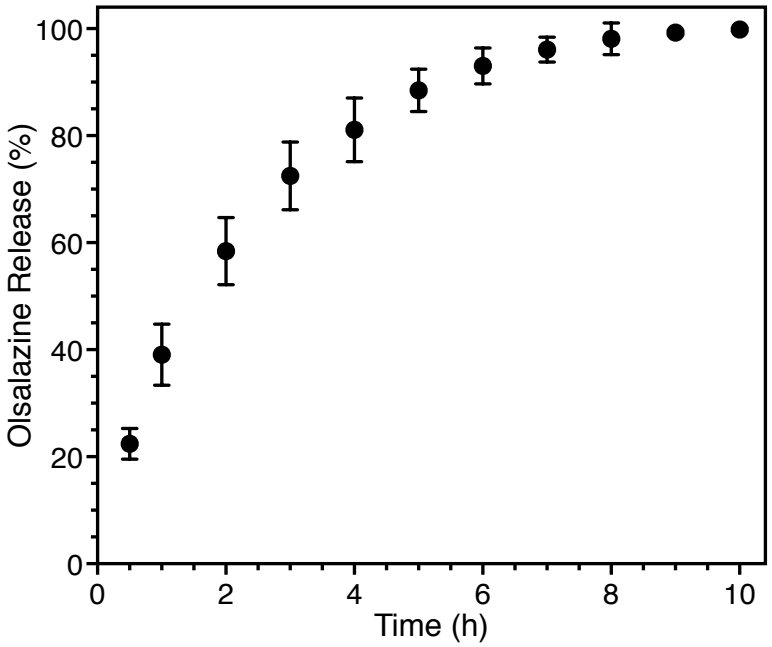

Figure 4.S.12. Release of olsalazine from the bare Mg_2(olz) framework. After synthesis, the Mg_2(olz) framework was washed 3x with DMF, 3x with MeOH, and 3x with EtOH, and then dried. 4.0 (± 0.3) mg pellets were pressed, and the release experiment was carried out under simulated biological conditions (pellet placed in 30 mL of PBS at 37 °C with bidimensional stirring at 60 rpm). 200 μL aliquots were removed at every time point, and 75 μL of each sample were placed on a black clear-bottom plate in duplicate and calibrated against Na_2(olz) standards in PBS at known concentrations. Absorbance was measured at 360 nm.

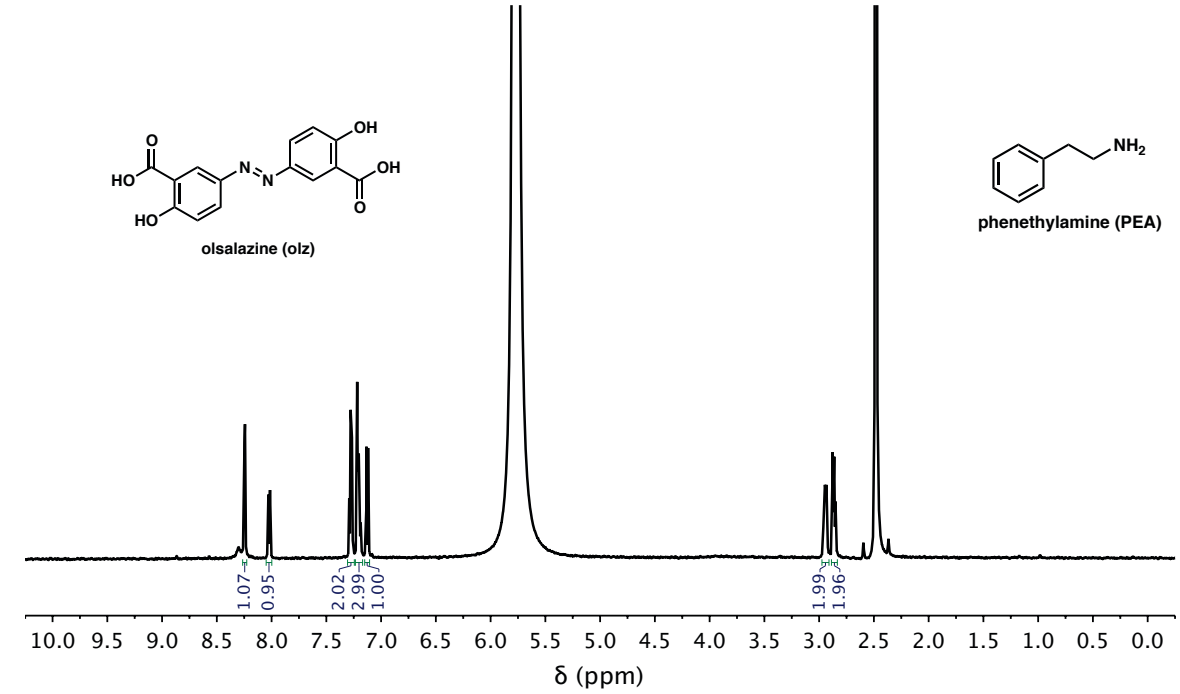

Figure 4.S13. ^{1}H NMR of $Mg_2(olz)(PEA)_2$ in d_6-DMSO (530 μL) and DCl (20 μL) (PEA = phenethylamine).

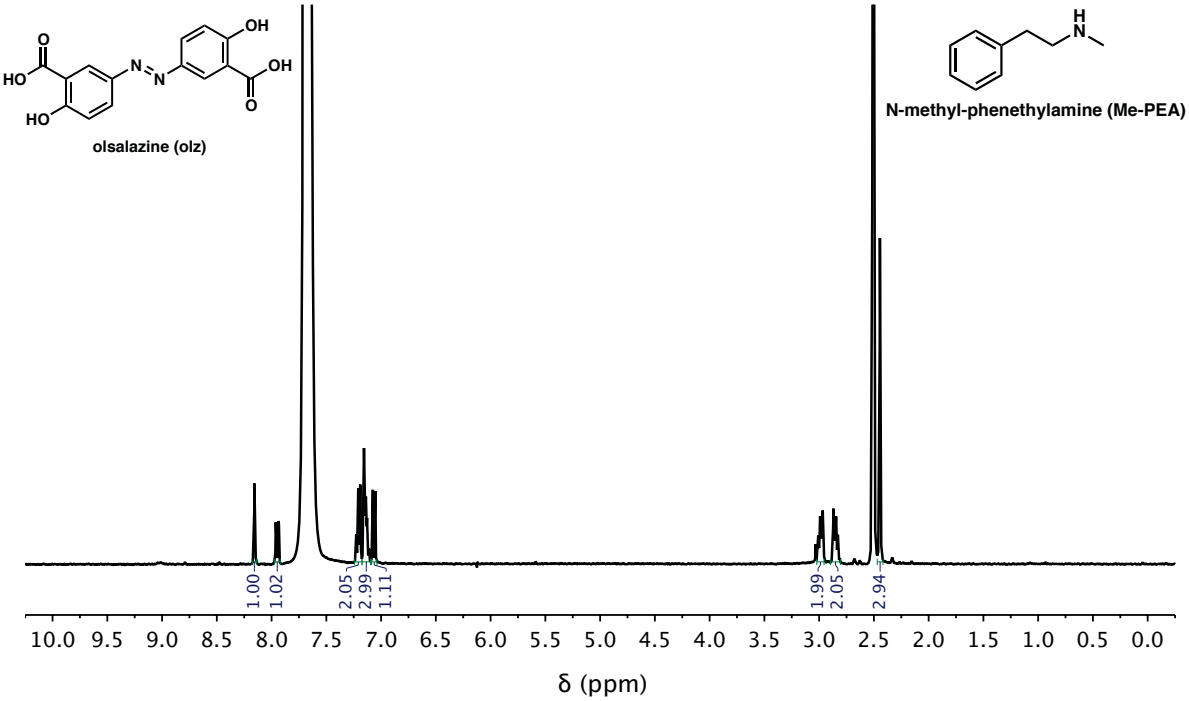

Figure 4.S14. ^{1}H NMR of $Mg_2(olz)(Me\text{-}PEA)_2$ in d_6-DMSO (530 μL) and DCl (70 μL) (Me-PEA = N-methyl-phenethylamine).